Electroelastic Modeling and Testing of Direct Contact Ultrasonic Clothes Drying Systems

Eric D. Dupuis

Dissertation submitted to the Faculty of
Virginia Polytechnic Institute and State University
in partial fulfillment of the requirements for the degree of

Doctor of Philosophy
In
Engineering Mechanics

Shima Shahab, Chair
Nicole Abaid
Anne Staples
Ayyoub Momen
Eli Vlaisavljevich
Viral Patel

April 30, 2020
Blacksburg, Virginia

Keywords: Ultrasonic drying, vibrations, piezoelectric, electromechanical, microchannel

Copyright 2020, Eric D. Dupuis

Electroelastic Modeling and Testing of Direct Contact Ultrasonic Clothes Drying Systems

Eric D. Dupuis

ABSTRACT

Energy efficient appliances and devices are becoming increasingly necessary as emissions from electricity production continue to increase the severity of global warming. Many of such appliances have not been substantially redesigned since their creation in the early 1900s. One device in particular which has arguably changed the least and consumes the most energy during use is the electric clothes dryer. The common form of this technology in the United States relies on the generation of thermal energy by passing electrical current through a metal. The resulting heat causes liquid within the clothing to evaporate where humid air is ejected from the control volume. While the conversion of energy from electrical to thermal through a heating element is efficient, the drying characteristics of fabrics in a warm humid environment are not, and much of the heat inside of the dryer does not perform work efficiently.

In 2016, researchers at Oak Ridge National Laboratory in Knoxville, Tennessee, proposed an alternative mechanic for the drying of clothes which circumvents the need for thermal energy. This method is called direct-contact ultrasonic clothes drying, utilizing atomization through direct mechanical coupling between mesh piezoelectric transducers and wet fabric. During the atomization process, vertical oscillations of a contained liquid, called Faraday excitations, result in the formation of standing waves on the liquid surface. At increasing amplitudes and frequencies of oscillation, wave peaks become extended and form “necks” connecting small secondary droplets to the bulk liquid. When the oscillation reaches an acceleration threshold, the droplet momentum is sufficient to break the surface tension of the neck and enable the droplets to travel away from

the liquid. For smaller drops where surface tension is high, a larger magnitude of acceleration is needed to reach the critical neck lengths necessary for droplet ejection. The various pore sizes within the many fabrics comprising our clothing results in many sizes of droplets retained by the fabric, affecting the rate of atomization due to the differences in surface tension.

In this study, we will investigate the physical processes related to the direct contact ultrasonic drying process. Beginning with the electrical actuation of the transducer used in the world's first prototype dryer, we will develop an electromechanical model for predicting the resulting deformation. Various considerations for the material properties and geometry of the transducer will be made for optimizing the output acceleration of the device. Next, the drying rates of fabrics in contact with the transducer will be modeled for identification of parameters which will facilitate timely and energy efficient drying. This task will identify the first ever mechanically coupled drying equation for fabrics in contact with ultrasonic vibrations. The ejection rate of the water atomized by the transducer and passed through microchannels to facilitate drying will then be physically investigated to determine characteristics which may improve mass transport. Finally, future considerations and recommendations for the development of ultrasonic drying will be made as a result of the insight gained by this investigation.

Electroelastic Modeling and Testing of Direct Contact Ultrasonic Clothes Drying Systems

Eric D. Dupuis

GENERAL AUDIENCE ABSTRACT

Energy efficient appliances and devices are becoming increasingly necessary as emissions from electricity production continue to increase the severity of global warming. Many of such appliances have not been substantially redesigned since their creation in the early 1900s. One device in particular which has arguably changed the least and consumes the most energy during use is the electric clothes dryer. The common form of this technology in the United States relies on the generation of thermal energy by passing electrical current through a metal. The resulting heat causes liquid within the clothing to evaporate where the humid air is ejected from the control volume. While the conversion of energy from electrical to thermal through a heating element is efficient, the drying characteristics of fabrics in a warm humid environment are not, and much of the heat inside of the volume does not perform drying as efficiently as possible.

In 2016, researchers at Oak Ridge National Laboratory in Knoxville, Tennessee, proposed an alternative mechanism for the drying of clothes which circumvents the need for thermal energy. This method is called direct-contact ultrasonic clothes drying, and utilizes a vibrating disk made of piezoelectric and metal materials to physically turn the water retained in clothing into a mist, which can be vented away leaving behind dry fabric. This method results in the water leaving the fabric at room temperature, rather than being heated, which bypasses the need for a substantial amount of energy to convert from the liquid to gas phase. The first ever prototype dryer shows the potential of being twice as efficient as conventional dryers.

This investigation is based around improving the device atomizing the water within the clothing, as well as understanding physical processes behind the ultrasonic drying process. These tasks will be conducted through experimental measurements and mathematical models to predict the behavior of the atomizing device, as well as computer software for both the parameters experimentally measured, and items which cannot be measured such as the flow in very small channels. The conclusions of this study will be recommendations for the future development of direct contact ultrasonic drying technology.

To my parents, brother, and sister, who have always been supportive and have always been there for me.

Acknowledgments

There are countless people, teachers, mentors, and friends who have helped me achieve and grow as a scholar that I am thankful for. Several of which have played an immense role in bringing me to this stage in my life where I am able to write and defend a dissertation to earn a doctoral degree. This acknowledgment is meant to thank those who have been there for me the most during the past four years of my education.

Firstly, my sincerest praise goes to my advisor, Dr. Shima Shahab, who has always been a source of inspiration and guidance as I undertook the most challenging portion of my education. Dr. Shahab has taught me much more than just being an ethical and efficient researcher; she has taught me many aspects of professionalism and has motivated me and been compassionate during several difficult moments during my graduate schooling. Her constant availability and openness to answer all of my many questions over the years has been undoubtedly the biggest contributor to my success has a researcher. I would not be able to communicate my findings as well as I have without her mentorship and support, while creating an environment of mutual respect and growth in her lab.

I would like to thank my committee members for their time and input into my research. Without their help and contributions, I would not be able to present this dissertation. For this, I thank Dr. Nicole Abaid, Dr. Anne Staples, and Dr. Eli Vlaisavljevich. A special thanks goes to my committee members and supervisors Dr. Ayyoub Momen, and Dr. Viral Patel. Their friendship and support of my research, as well as their constant positive feedback and help has given me the confidence to proceed during this difficult stage in my education, and without them I would not be where I am today.

I would like to thank my labmates, Omid, Marjan, Aarushi, and Vamsi, for their friendship and support both in my courses and in my research. Much of my success is due to their constant availability to answer my questions, lend a helping hand, and help troubleshooting issues in my experiments and coding. I owe much of my progress to their guidance as they have always helped to ground me during frustrating times and have been a source of inspiration, as I tried to always rise to their level as a researcher.

A special thanks goes to Kateri, for her help in motivating me and her companionship over the last and most difficult years of my education. Her understanding and support has allowed me to focus my attention on school, and without her, my life would have been severely more chaotic.

Above all, I would like to thank my parents, brother, and sister, who have always supported and praised my accomplishments, giving me the motivation and courage to pursue higher education. Without their support, I would not be where I am today.

I would also like to thank the institution that made this work possible. This work was sponsored by the U. S. Department of Energy's Building Technologies Office under Contract No. DE-AC05-00OR22725 with UT-Battelle, LLC. The authors would also like to acknowledge Mr. Antonio Bouza, Technology Manager – HVAC&R, Water Heating, and Appliance, U.S. Department of Energy Building Technologies Office.

Attribution

Chapter 2: This chapter represents a collaborative work with Dr. Shima Shahab, Dr. Ayyoub Momen, and Dr. Viral Patel which has been published in the Applied Energy journal.

Chapter 3: This chapter represents a collaborative work with Dr. Shima Shahab, Dr. Ayyoub Momen, and Dr. Viral Patel which has been published in the Smart Materials and Structures journal.

Chapter 4: This chapter represents a collaborative work with Dr. Shima Shahab, Dr. Ayyoub Momen, Dr. Viral Patel, and Dr. Zhaokuan Lu, which will be published at a future date.

Contents

List of Figures

List of Tables

Chapter 1

Introduction

1.1 Background

Residential and commercial clothes drying is an energy intensive process that has not made significant technological advancements since the invention of the modern electric dryer in 1938 by J. Ross Moore [1]. Since its invention, the same fundamentals of generating thermal energy for evaporating moisture in clothing has been used in subsequent generations of residential clothes dryers. While the method of producing thermal energy has changed from combustion of materials to the passage of electricity through a heating element, the concept has remained unaltered. Sensor technology, control cycles, and heat exchangers have been used to increase the efficiency of dryers; however, they have subsequently increased the time it takes to dry clothing. In the United States, the majority of consumers favor quick dry times which consumes significantly more energy than European counterparts utilizing heat exchanges and regenerative technology. This is evident since over 80% of the market share of dryers sold in the U.S. are electric resistance. [2]. These dryers consume approximately 4% of the energy produced in the United States [2].

Energy star appliances have sought to increase the efficiency of this technology, but with limited results. These appliances are categorized by their combined energy efficiency factor (CEF), measuring the pounds of clothing dried per kWh of electricity consumed. A subset of available dryers can be pictured in figure 1.1, where it can be quickly seen the CEF of electric resistance dryers are substantially lower than rival heat pump dryers, as well as hybrid dryers utilizing a combination of both technologies; moreover, the legal minimum CEF necessary to be sold in the United States is close behind that of electric resistance dryers, and as our restrictions on energy

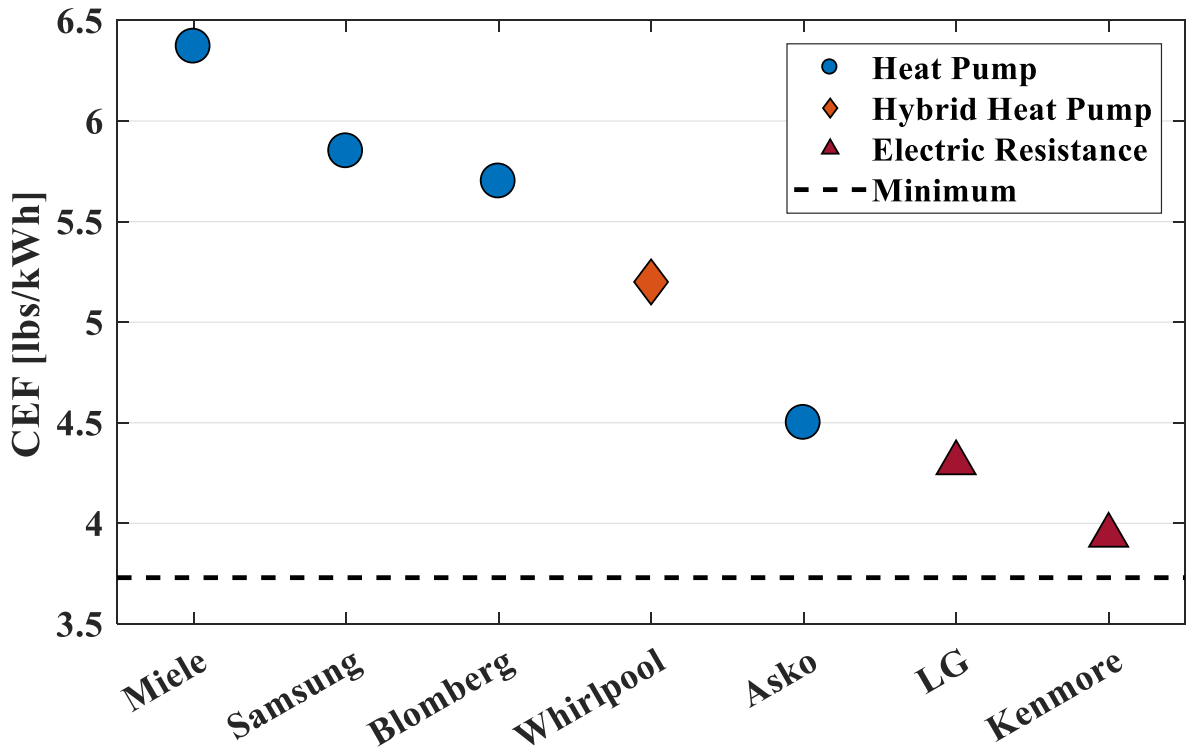

Figure 1.1. Energy efficiency comparison of different dryer types.

inefficient appliances increase, it is not a farfetched idea that electric resistance dryers may soon be obsolete.

It is necessary to change the fundamental mechanic for which these dryers operate in order to move away from electric resistance heating elements and towards ultra-efficient clothes dryers. In 2016, researchers at Oak Ridge National Lab in Oak Ridge, Tennessee, turned to piezoelectric elements to solve this problem. The high efficiency of electromechanical coupling piezoelectric materials is defined by means that much of the input electrical energy will be converted to useful mechanical work. By mechanically exciting the wet fabric, researchers were able to atomize the water retained in the clothing, turning the retained moisture to a fine mist which can be vented out of the clothing either through forced air as well as through microchannels embedded within the piezoelectric transducers.

This investigation will consider the multiphysics process of atomization, from the actuation of the piezoelectric device, to the atomization and ejection of water from the fabric. The mathematical models and insight gained will aid in the development of the next generation clothes dryer. We will begin with the electromechanical modeling of the piezoelectric transducer before connecting the output acceleration to the drying rates of fabrics it is in contact with. From this point, the atomized water and its passage through the microchannels within the transducers plate will be investigated for increasing the mass flow rate.

The proposed dissertation includes the electroelastic analytical models, which couple multiphysics topics, as well as finite element and experimental verification of the developed models. The models introduced identify the influence of key parameters on ultrasonic drying and will aid in improving atomizer design for efficient, timely fabric drying. This study is the first proposed model for the ultrasonic atomization of fabrics saturated with water, applicable to any type of transducer. The results present a non-dimensional equation for the ultrasonic dewatering of fabrics, dependent only on transducer acceleration and the surface area of the cloth. The development of this technology using the proposed physical models will allow for global reductions in electrical demand related to clothes drying.

1.2 Governing physics

The direct contact atomization process for water retained in fabrics is a multi-step process coupling electromechanical and fluid mechanic behavior. The center point of which is a particular piezoelectric transducer selected for its drying capabilities due to several key features [3]. The transducer shown in figure 1.2 is comprised of an outer bimorph portion, responsible for converting the input electrical signal to a mechanical deformation. The inner portion of this

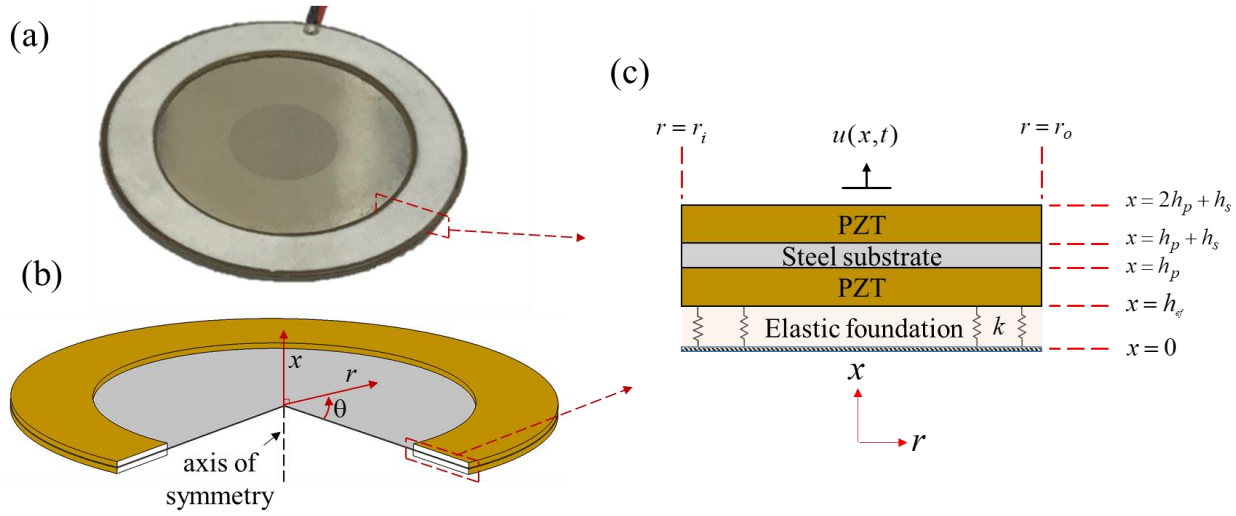

Figure 1.2. (a) Transducer image, **(b)** transducer schematic and coordinate system, and **(c)** transducer cross section.

transducer is a thin stainless-steel plate which is also the substrate of the bimorph. Due to the bimorphs deformation acting as a base excitation, the plate vibrates according to classical plate theory; this is due to its thickness to diameter ratio fitting the criteria for Kirchoff plate theory. This thin plate is able to vibrate with sufficient acceleration from the motion of the bimorph so that water in contact with its surface is nearly instantly atomized. Finally, small microchannels laser cut into the plate (figure 1.3) help to facilitate the transport of water from the top of the transducer to the bottom, where it is vented away due to the high velocities the liquid reaches inside of the channel. We will break this process into four parts:

1. Actuation of the bimorph via an electrical stimuli.
2. Vibration of the thin inner plate due to the deformation of the bimorph.
3. Drying characteristics of fabrics in contact with the vibrating transducer.
4. Liquid transport characteristics inside of the microchannel.

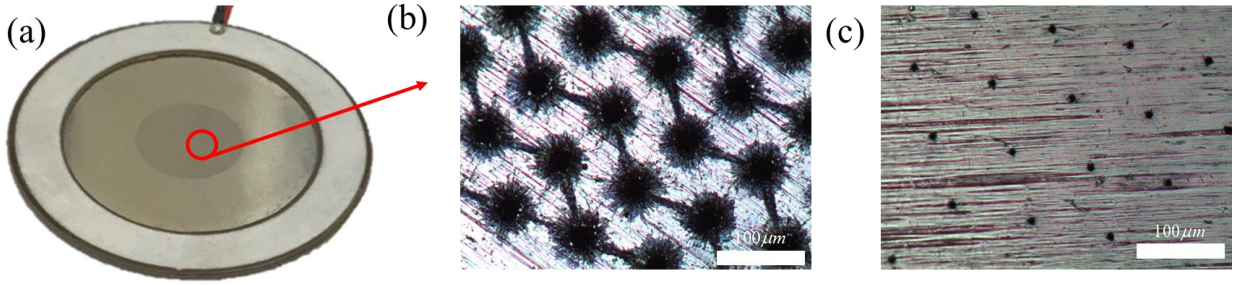

Figure 1.3. (a) Transducer image, **(b)** top view showing microchannel inlet, and **(c)** bottom view showing microchannel outlet.

The first portion will consider linear piezoelectric theory, where Hamilton's principle and Galerkin's Method are used together to solve for the motion of the bimorph due to an applied voltage. The analytical model developed considers the material properties and geometry of the bimorph, where the boundary conditions can be altered to consider a wide range of mounting conditions for the transducer. The goal of this model is to evaluate resonance between the bimorph and the plate, while also creating an equation capable of being optimized.

The second portion is the vibration of a thin plate by a base excitation. The bimorph displaces by a known amount due to the previous modeling efforts, and therefore the outer portion of the plate is forced according to this motion. The unconstrained portion of the plate is then free to vibrate as a function of its material properties, geometry, and the excitation frequency and magnitude. This model is based upon Kirchoff plate theory, valid for displacements smaller than the plate's thickness and the aspect ratio at hand. The plate is able to reach much higher magnitudes of acceleration than the bimorph due to the lack of constraints and lower mass. The acceleration output is then capable of oscillating liquids with sufficiently small capillary wave lengths that droplet ejection is achieved.

During the third stage, the physics of atomization and droplet ejection occur within the fabric. Due to the oscillation of the fabric generated by the vibrating transducer, liquid droplets

retained between pores in the fabric are excited and capillary waves generated on their surface. The resulting small diameter droplets that are ejected pass through the fabric where it is capable of being vented away, either through the microchannels when the mist moves downward, or by ambient air if it is ejected upwards.

Lastly, the ejected mist in the form of droplets pass through microchannels in the center of the plate, visible as the darkened region on figure 1.3a. These microchannels have an inlet diameter of 70 μm, and an outlet of 10 μm. Due to the oscillatory motion of the plate the downwards motion results in air entrainment, leading to two phase flow dynamics. The complexity of the flow arises due to air entrainment, as well as the short length of the channel, resulting in significant entrance and exit effects; moreover, the open-air outlet and decreasing water supply at the inlet results in complex boundary conditions. An investigation into increasing the mass flow rate of the microchannels by controlling its physical parameters will be considered to increase the transport of water. The motion of the microchannel is the only known parameter, as the modeling efforts in the first two stages predicts its displacement due to an applied voltage to the bimorph.

1.2.1 Piezoelectric actuation

Piezoelectric materials are those which can convert mechanical strain into electrical charge, noted as the piezoelectric effect, and vice versa, where the inverse piezoelectric effect converts electrical charge into mechanical strain. This phenomenon occurs due to an imbalance of charge within the lattice structure of the material creating a dipole (figure 1.4 [4]). These materials have been well suited for a wide range of tasks, most typically with regards to the field of vibrations.

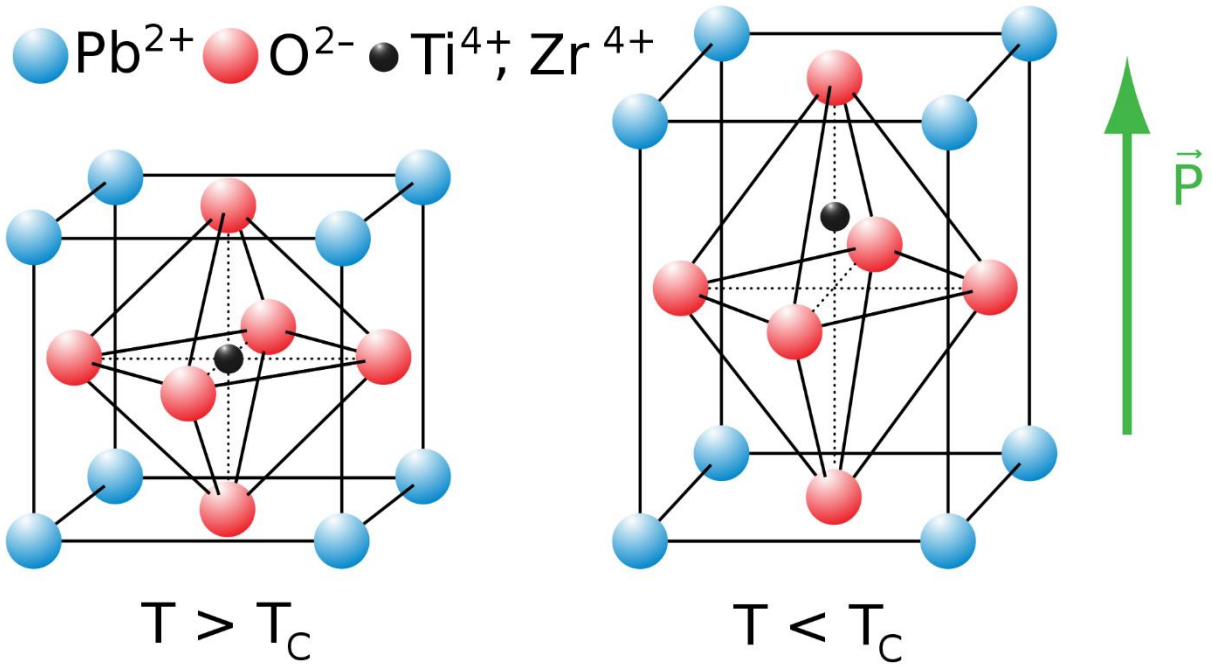

Figure 1.4. Crystalline structure of PZT highlighting the charge imbalance.

Vibration-based models of small-scale piezoelectric systems have been an increasingly popular research area for a wide range of applications including energy harvesting, controls, structural health monitoring, and contactless acoustic energy transfer systems, among others [5-10]. For these applications, access to the devices and energy availability are limited, making self-powered, wireless networks highly desirable. Electromechanical models relating the input deformations to the output charges produced are necessary for achieving system efficiencies that approach the high coupling factors piezoelectric materials are defined by.

For a bimorph structure under actuation, such as the transducer in figure 1.2, a voltage is applied across the top surface of the upper piezoelectric layer where it is connected in series to a terminal on the bottom surface of the lower piezoelectric layer. For modeling purposes, the steel substrate is considered a perfect conductor. The poling directions of the layers are away from the substrate, denoting a bending mode deformation of the bimorph; however, the highest piezoelectric

coupling is in the thickness direction, giving evidence that thickness mode deformations dominate the displacement of the structure. This notion is further tested and proven in chapter 3.

Actuation of the bimorph with an alternating current signal produces an oscillating deformation capable of reaching high magnitudes of acceleration due the high operating frequencies. The transducer in figure 1.2 excites the central unconstrained portion of the substrate, allowing for resonance of the actuator and plate to further increase the output acceleration this transducer is capable of, as compared to a bimorph only. A knowledge gap regarding modeling was found for systems with poling and forcing along the same axis, using the distributed parameter approach. These systems are often modeled using lumped parameters; however, this method does not allow for accurate analysis of design changes with regards to an annular bimorph structure. The majority of distributed parameter models assume bending is the dominant deformation [5, 11]. There is a need for distributed parameter analytical models of piezoelectric transducers where electromechanical coupling is along the same axis and bending is not a dominant deformation. This thesis will fill this gap in knowledge by providing a straightforward approach for distributed parameter modeling of an annular bimorph operating in the 33-mode of piezoelectricity. The developed models will be connected to the drying rate of wet fabrics in contact with ultrasonic vibrations.

1.2.2 Liquid atomization

Atomization is the process of a bulk liquid being excited with sufficient intensity that smaller diameter droplets are ejected from its surface. The physics of droplet ejection has been shown to be predominantly governed by free-surface breakup due the extended lengths of capillary

waves forming on the liquids surface [12]. Figure 1.5 is an example of this process, where we see the liquid initially take on the radial mode shapes the plate exhibits, before a mist is ejected from the bulk liquid, evident by the decrease in liquid volume over the transducers surface.

The formation of capillary waves on the bulk liquid has been robustly related to the driving frequency and amplitude of the faraday excitations. Several studies concluded the critical acceleration, a_c, needed for atomization of low-viscosity fluids such as water can be defined as

$$a_c \approx c \cdot \omega^{4/3} (\sigma / \rho_f)^{1/3} \tag{1.1}$$

where σ is the surface tension, ρ_f is the fluid density, ω is the radial excitation frequency given in rad·s^{-1}, and c is a constant coefficient. The constant c had been found experimentally to be 0.261 or 4, depending on the definition of the atomization event, either when it first occurs or ceases [12, 13]. The diameter of the ejected droplet when this critical acceleration is achieved has been shown to be approximately one third of the wavelength of the driving frequency, given as [14]

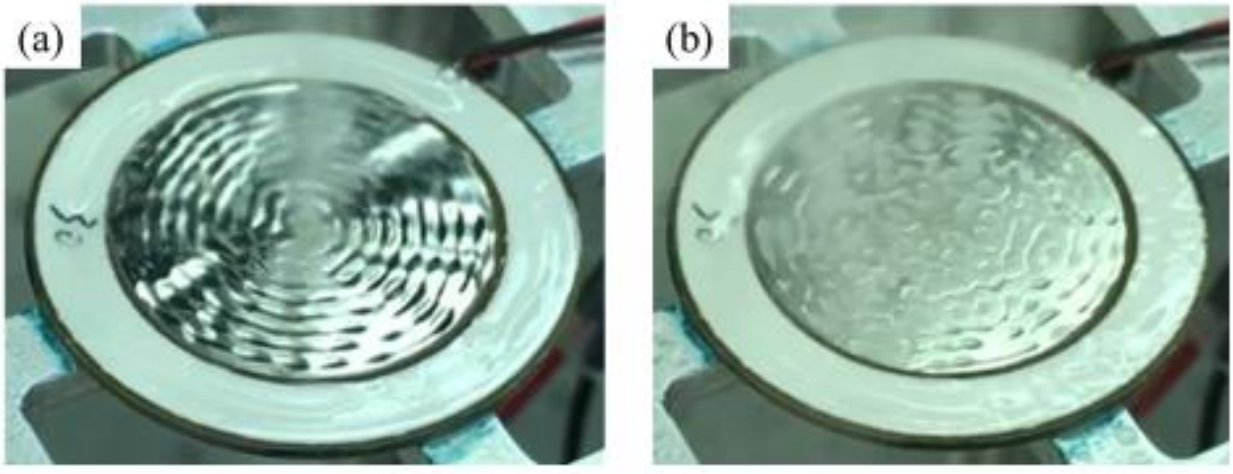

Figure 1.5. (a) Excitation of a liquid by the transducer, pre-atomization, and **(b)** during atomization.

$$D = 0.34\left(\frac{32\pi^3\sigma}{\rho\omega^2}\right)^{1/3} . \quad (1.2)$$

This result also gives insight into the forces at play during free-surface breakup. The capillary wave peak forming a bulbous tip will have sufficient momentum at the critical acceleration to overcome the surface tension holding the wave together. For such small droplets, inertia is not typically a large force, but for the critical acceleration to be achieved the time scale of oscillation is small enough for inertia to be a large factor in droplet ejection. The distribution of droplet sizes is very consistent, and follows a near normal distribution around an average droplet diameter, commonly in the micrometer range [15-17].

1.2.3 Direct contact ultrasonic drying

The acceleration imparted from the vibration applied to a bulk liquid is capable of atomizing liquids it is in contact with when the forcing is large enough, as given by equation (1.1). The oscillatory force applied to a bulk liquid is proportional to the mass of the hemisphere droplet formed, m, the vibration amplitude, A, and the frequency of operation, ω, given as

$$F_o \sim mA\omega^2 . \quad (1.3)$$

For a droplet not retained by a fabric, its mass can be written as $\frac{1}{12}\pi d^3\rho$ where the drops density is ρ, and the diameter d. The oscillatory force must overcome the droplets surface tension only. This surface tension is dependent on the contact angle the liquid makes with the plate; therefore, the force it applies is written as

$$F_s \sim \sigma\pi d\cos(\theta) \quad (1.4)$$

where σ is the liquids surface tension coefficient and θ is the contact angle. There exists a ratio of the applied oscillatory force to the surface tension force, which must be overcome for atomization to occur, given as [3]

$$R \sim \frac{F_o}{F_s} \sim \frac{d^2 \rho A \omega^2}{12\sigma \cos(\theta)} \ . \tag{1.5}$$

For values of R larger than unity, the applied force is larger than the surface tension, and the capillary waves appearing on the surface of the droplet extend to a critical length where the tips break off as a mist.

The same physics occur when water is retained within a fabric. The significant difference being that a fabric has a distribution of pore sizes between its threads; therefore, varying sizes of droplets are retained in the fabric. The acceleration imparted to a wet fabric will atomize the largest droplets retained first, as the forcing ratio R is largest, followed by smaller and smaller droplets until a limit is reached. At this limit, temperature increases due to the heating of the piezoelectric as well as friction due to the motion of the threads results in thermal evaporation of the smallest droplets.

These two regions of drying, the atomization and thermal regions, are nonlinear and linear, respectively [18]. The nonlinear region, being a decreasing exponential rate of water loss, is due to the limited supply of water for which the forcing ratio is greater than unity. The drops with the largest ratio are atomized first, and the slowly decreasing rate is indicative of the supply of such drops disappearing. The latter constant rate of water loss until the fabric is dry is indicative of evaporative drying. For the atomized water, microchannels within the plate help to transport moisture away from the fabric, greatly facilitating the efficiency of direct contact ultrasonic drying.

1.2.4 Microchannel flow

Microchannels are narrow tubes less than 1mm in diameter which exhibit many enhanced fluid properties, such as volume flow rate and heat transfer. These structures have received an increase in attention over the years due to increases in microfabrication capabilities as well as measuring techniques for such small-scale systems. The transducer in this investigation utilizes an array of microchannels for transporting of water from the fabric to the air beneath the transducer. These structures are tapered, having an inlet diameter of approximately 70 μm and an outlet of 10 μm, which helps to increase the velocity gradient leading to increase volume flow rates. In this section, we will analyze the microchannel flows for the oscillating plate in an attempt to bridge the velocity of the oscillation to the mass flow rate of the channel for optimization purposes. The physics associated with droplet ejection will be investigated to identify the needs of future work.

1.3 Research overview

In this investigation, we will apply experimental, computer aided, and theoretical concepts for the prediction, quantification, and analysis of the physics of direct contact ultrasonic clothes drying. By using three methods of verification, a robust model can be developed which can be depended on for further developments, helping to decrease the cost of prototyping and manufacturing. The multiple physics involved in ultrasonic drying requires a wide range of tools for analysis and prediction.

Chapter 2 of this dissertation covers the electromechanical modeling of the transducer used in ultrasonic drying. Both analytical and finite element models of the transducer are developed, where validation is done by comparisons to experimental measurements. This section will focus

on an in-depth development of an analytical equation predicting the transducers motion as a result of an applied voltage and dependent on mounting conditions, geometry, and material properties of the system. Hamilton's principle is used for the analytical modeling in this section. Finite element modeling is achieved through COMSOL Multiphysics, where all parts of the analytical model are confirmed prior to experimentation.

Chapter 3 will discuss the drying characteristics of fabrics actuated by ultrasonic vibrations from the previously mentioned transducer. The physics of atomization will be discussed further, and the forcing principles discussed previously applied to the imparted acceleration to a bulk liquid from a vibrating source. Then, the various drying regimes of fabrics in contact with ultrasonic vibrations is discussed and linked to the previous principles. Finally, a model describing the regimes of drying will be proposed by utilizing empirical evidence. A discussion on the electromechanical modeling of the system and its effect on drying will finish this section.

Chapter 4 will focus on the microchannels within the plate which facilitate liquid ejection. This section will utilize support from computational fluid dynamics via COMSOL Multiphysics. Relying on computer aided models is necessary as experimental techniques for a short open microchannel are difficult, and to the authors knowledge no such experiments have been conducted in the frequency range of the operating point for the transducer in this investigation (~100kHz). The results will be a discussion on alterations to the microchannel which may increase the mass flow rate of the system.

Chapter 5 is an experimental investigation into alternative drying configurations based on the lessons learned in the previous sections. Computer aided models will confirm observations and hypothesis as we attempt to scale the drying system to a larger contact area. It is this Section's goal to test the idea that fewer high-power transducers actuating a larger structure are more

efficient than many transducers with a smaller surface area. The design simplification that comes with the switch to fewer transducers is the driving force behind this investigation. Alternative dryer configurations will be proposed which can take advantage of the large area atomization this section aims to prove feasible.

Bibliography

1. Acton, J., T. Adams, and M. Packer, *The origin of everyday things*. 2006, New York: Sterling.
2. Administration, U.S.E.I. *Annual Energy Outlook*. 2019; Available from: https://www.eia.gov/outlooks/aeo/tables_ref.php.
3. Peng, C., et al., *Physics of direct-contact ultrasonic cloth drying process.* Energy, 2017. **125**: p. 498-508.
4. Pinin, *Tetragonal unit cell of lead titanate*. 2010: Wikimedia.
5. Anton, S.R. and H.A. Sodano, *A review of power harvesting using piezoelectric materials (2003–2006).* Smart Materials and Structures, 2007. **16**(3): p. R1-R21.
6. Cook-Chennault, K.A., N. Thambi, and A.M. Sastry, *Powering MEMS portable devices—a review of non-regenerative and regenerative power supply systems with special emphasis on piezoelectric energy harvesting systems.* Smart Materials and Structures, 2008. **17**(4).
7. Shahab, S. and A. Erturk, *Contactless ultrasonic energy transfer for wireless systems: acoustic-piezoelectric structure interaction modeling and performance enhancement.* Smart Materials and Structures, 2014. **23**(12): p. 1-13.

8. Shahab, S., M. Gray, and A. Erturk, *Ultrasonic power transfer from a spherical acoustic wave source to a free-free piezoelectric receiver: Modeling and experiment.* Journal of Applied Physics, 2015. **117**(104903): p. 1-8.

9. Shahab, S., D. Tan, and A. Erturk, *Hydrodynamic thrust generation and power consumption investigations for piezoelectric fins with different aspect ratios.* The European Physical Journal Special Topics, 2015. **224**(17-18): p. 3419-3434.

10. Shahab, S., S. Zhao, and A. Erturk, *Soft and Hard Piezoelectric Ceramics and Single Crystals for Random Vibration Energy Harvesting.* Energy Technology, 2018. **6**(5): p. 935-942.

11. Fan, K., et al., *Design and development of a multipurpose piezoelectric energy harvester*. Energy Conversion and Management, 2015. **96**: p. 430-439.

12. Vukasinovic, B., M.K. Smith, and A. Glezer, *Mechanisms of free-surface breakup in vibration-induced liquid atomization.* Physics of Fluids, 2007. **19**(1).

13. Goodridge, C.L., et al., *Viscous effects in droplet-ejecting capillary waves.* Physical Review E, 1997. **56**(1): p. 472-475.

14. Lang, R.J., *Ultrasonic Atomization of Liquids.* The Journal of the Acoustical Society of America, 1962. **34**(1): p. 6-8.

15. Ramisetty, K.A., A.B. Pandit, and P.R. Gogate, *Investigations into ultrasound induced atomization.* Ultrason Sonochem, 2013. **20**(1): p. 254-64.

16. Barreras, F., H. Amaveda, and A. Lozano, *Transient high-frequency ultrasonic water atomization.* Experiments in Fluids, 2002. **33**(3): p. 405-413.

17. Donnelly, T.D., et al., *An experimental study of micron-scale droplet aerosols produced via ultrasonic atomization.* Physics of Fluids, 2004. **16**(8): p. 2843-2851.

18. Peng, C., A.M. Momen, and S. Moghaddam, *An energy-efficient method for direct-contact ultrasonic cloth drying.* Energy, 2017. **138**: p. 133-138.

Chapter 2

Electroelastic investigation of drying rate in the direct contact ultrasonic fabric dewatering process

Abstract

Ultrasonic vibrations, used to atomize liquids into a fine mist, are a promising solution for the future of efficient clothes drying technology. The world's first ultrasonic dryer—demonstrated by researchers at Oak Ridge National Laboratory—successfully applies the scientific principles behind ultrasonic drying, and several working prototypes have been demonstrated. This technology is based on direct mechanical coupling between mesh piezoelectric transducers and wet fabric. During the atomization process, vertical oscillations of a contained liquid, called Faraday excitations, result in the formation of standing waves on the liquid surface. At increasing amplitudes and frequencies of oscillation, wave peaks become extended and form "necks" connecting small secondary droplets to the bulk liquid. When the oscillation reaches an acceleration threshold, the droplet momentum is sufficient to break the surface tension of the neck and enable the droplets to travel away from the liquid. In this work, we investigate the atomization process using an ultrasonic transducer as it pertains to moisture retained within a fabric. An experimentally validated electromechanical analytical-numerical model is proposed. This model bridges the vibrations of a piezoelectric mesh transducer to the critical acceleration needed for fabric drying to occur. Then, the drying rate model is developed, consisting of an initial nonlinear region due to atomization, followed by a linear thermal evaporation region. The models developed identify the influence of key parameters on ultrasonic drying and will aid in improving atomizer design for efficient, timely fabric drying. This study is the first proposed model for the ultrasonic

atomization of fabrics saturated with water, applicable to any type of transducer. The results present a non-dimensional equation for the ultrasonic dewatering of fabrics, dependent only on transducer acceleration and the surface area of the cloth. The development of this technology using the proposed physical models will allow for global reductions in electrical demand related to clothes drying.

2.1. Introduction

As climate change and sustainability concerns push the energy market toward renewable electrical production, the energy efficiency of common products is often overlooked. As important as it is to efficiently produce energy, it is just as necessary to efficiently consume it. One innovation tackling this very challenge is the ultrasonic clothes dryer. Modern drying technology is heavily reliant on electrical resistance heat generation to thermally evaporate moisture. In the United States, this process can account for 10–15% of annual residential electricity use; and in European countries it may be as much as 20–25% (the European percentage is higher only because the data source is more recent) [1]. Although improvements in electric resistance dryer design such as control systems and heat exchangers can increase efficiency by upwards of 10%, the high latent heat of the vaporization of water is the limiting factor of this technology [2, 3]. The next generation of drying technology must turn to new principles of moisture extraction for substantial improvements to be made. This thesis introduces a novel solution for characterizing the key parameters in the ultrasonic drying process that will contribute to advancements in the development of energy efficient direct contact ultrasonic dryers.

Researchers at Oak Ridge National Laboratory turned to mechanical vibrations for extracting moisture from clothes and, in 2016, produced the world's first benchtop ultrasonic dryer

[4, 5]. The dryer's novelty came from the use of a piezoelectric compound (PZT, lead zirconate titanate) to apply direct vibrations to an article of fabric for moisture removal, bypassing the latent heat of vaporization. Through mechanical removal, water leaves the fabric as a cold mist of water droplets. The lack of heating or evaporation involved makes this process extremely energy efficient. Performance evaluations of this technology have shown an order of magnitude decrease in energy consumption compared with a typical electric resistance dryer, and five times lower than the latent heat of vaporization at water contents greater than 20% [6]. This performance gain using ultrasonic technology is immense, especially when considering a 2013 study concluding that heat-pump dryer technology was, at the time, the most energy efficient as it consumed 40% less energy than standard dryers [7]. Comparisons of various drying technology affirms the need for development of direct contact ultrasonic drying. This chapter contributes an in-depth analysis of fabric drying trends when exposed to ultrasonic vibrations that will further improve upon the already drastic increase in clothes drying energy efficiency for this new technology. Although the invention of the direct-contact ultrasonic dryer is historic, the concept of using non-contact ultrasonic pressure waves for drying is not.

The first observations of ultrasonic atomization came in 1927 by W. R. Wood and A. L. Loomis [8]. The pair reported a dense fog forming when drops of oil were placed on a vibrating piezoelectric transducer. Söllner made several accurate predictions regarding this process, most notably hypothesizing the importance of cavitation [9, 10]. Further experiments by Söllner revealed the non-contact drying capabilities of ultrasonic transducers. While studying the effects of ultrasonics on dilatancy, he discovered that moisture is removed from wet sand when it is exposed to non-contact vibrations for a long period of time [11]. This was the first, albeit inadvertent, observation of non-contact ultrasonic drying.

Decades later, this technology was revitalized after experiments revealed the relationship between driving frequency and capillary waves for contained liquids exposed to Faraday excitations. Lang concluded that capillary waves oscillate at half the driving frequency and, through the use of the Kelvin equation for the wavelengths of capillary waves, the length scale can be accurately calculated [12]. Moreover, Lang found that droplets produced during atomization were approximately one-third of this wave length. This result proved to be valuable for many industries for which creating a spray with consistent particle dimensions is beneficial, such as ink-jet printing, spray coating, and nebulizers. The method of predicting atomization characteristics due to the presence of capillary waves became known as capillary wave theory [6, 13, 14].

Because of industry interest in atomization technology for sprays, capillary wave theory was favored in many studies following Lang's experiments [15-21]. Consequently, the mechanisms of free surface breakup of a liquid drop excited by ultrasonic vibrations were studied in depth. Capillary wave theory predicts atomization on the basis of several types of liquid instability, such as Rayleigh, Taylor, and Faraday [14-16, 18-24]. The theory is commonly defined as follows: Faraday excitation, or the vertical oscillation of a liquid, produces standing waves that form on the liquid surface. At sufficient intensities, the wave peaks extend, forming a jet of water. At critical lengths of the jet, a bulbous tip is formed as a result of necking of the liquid column [18, 19, 21, 23, 24]. Instability of the jet may eject this bulbous tip away from the bulk liquid, if its momentum is able to overcome capillary forces [18]. It is also possible for the drop to be ejected, but with a velocity toward the bulk liquid, or even for several drops to be emitted from the jet at once [18]. The conditions necessary for free surface atomization are dependent on excitation frequency and surface tension for low-viscosity fluids, and on frequency and viscosity for high-

viscosity fluids [15]. Several studies concluded the critical acceleration, a_c, needed for atomization of low-viscosity fluids can be defined as

$$a_c \approx c \cdot \omega^{4/3} (\sigma / \rho_f)^{1/3}, \tag{2.1}$$

where σ is the surface tension, ρ_f is the fluid density, ω is the radial excitation frequency given in rad·s^{-1}, and c is a constant coefficient. The constant c had been found experimentally to be 0.261 or 4, depending on the definition of the atomization event, either when it first occurs or ceases [15, 18]. While this result proved useful for industry, capillary wave theory could not fully explain the atomization process.

Advancements in technology allowed for Söllner's observations of cavitation to be tested [14, 25]. Commonly known as cavitation theory, the conjecture was that shocks propagating from the source of excitation form cavitation bubbles within the liquid. The implosion of these bubbles releases relatively massive amounts of energy capable of ejecting droplets. The observation of ejected droplets—either small in mass with high velocity, or large with low velocity—was well explained by the presence of cavitation, as capillary wave theory suggests a narrow distribution around a single drop diameter [9, 14]. Possibly the soundest evidence of cavitation was found when an aqueous solution of potassium iodide was atomized. The rapid temperature and pressure changes associated with cavitation are a catalyst for chemical reactions. It was found that the solution decomposed when placed on the active atomizer, suggesting that the energy produced from cavitation is present and actively liberating the iodine from the compound [14].

Because of strong evidence of cavitation occurring, coupled with the accuracy of droplet prediction via capillary wave theory, the explanation of atomization is commonly a combination of both theories. One study attempted to analytically model capillary waves as a result of cavitation

and found threshold relationships similar to those in Goodridge et al. (1996) [16, 26]. However, to the authors' knowledge, no model coupling the two has successfully predicted the atomization process.

The instabilities leading to droplet atomization have been used for the purpose of de-wetting fabrics. Pores of void space between threads are occupied by liquid droplets. The application of ultrasonic vibrations oscillates the entire fabric, resulting in the atomization of these retained droplets, according to the mechanics of capillary wave theory and cavitation theory. The resulting smaller ejected droplets are able to escape the large pores, and momentum carries them away from the fabric. This process continues until the remaining moisture occupies the smallest pores available, within which the increased surface tension due to the decrease in drop diameter is larger than the excitation force. From this point, fabric vibrations create friction, which imparts thermal energy to the moisture, eventually leading to evaporation.

Preliminary studies of ultrasonic drying have identified several important design considerations, the most important of which is the selection of a particular type of atomizer. When a solid piezoelectric transducer is used, the atomized mist is ejected upward, and some moisture falls back into the fabric. Similarly, a layer of mist may form between the fabric and transducer surface, temporarily eliminating the contact that is necessary for optimal drying [4, 6]. It was found that atomizers typically used in nebulizers perform the best. The key characteristic of these devices is micrometer-scale holes laser-cut into the mesh-like transducer. When vibrating, these holes produce a pressure difference that actively transports moisture through the vibrating mesh and ejects mist away from the transducer. The ability to transport moisture far away from the fabric decreases the time it takes to dry. Furthermore, the drying trends for fabrics exposed to ultrasonic drying have been shown to exhibit an initial nonlinear region followed by a linear drying region

[4]. This finding is the basis of the model proposed in this research. The initial nonlinear region is where the immense performance gain in ultrasonic fabric drying occurs.

The knowledge gap in current ultrasonic drying technologies centers on a lack of modeling techniques. While modern electric resistance dryers and even newly demonstrated thermoelectric dryers have well developed thermal-coupled models [27-30], the lack of attention towards the mechanics of atomization limits the ability to predict direct contact ultrasonic drying performance. Specifically, the dewatering phenomenon as a result of direct contact ultrasonic vibrations with wet textiles has received little attention prior to its first investigation in 2016 [4, 6]. These studies identified the rate of water loss and temperature changes in a wet fabric due to ultrasonic vibrations, but did not attempt to model the trends discovered. Consequently, there are no accurate methods for predicting the magnitude of energy savings using this technology. It is for this reason the development of an experimentally-validated drying rate model coupling the piezoelectric atomizer performance with moisture removal is necessary. The originality of the proposed techniques for ultrasonic drying rate analysis will provide a foundation for accurate energy consumption predictions.

In this study, for the first time, we investigate the atomization process of water suspended in a fabric for the development of the ultrasonic clothes dryer. Specifically, we investigate electroelastic dynamic actuation of a piezoelectric transducer and the drying rate of fabrics actuated by the mesh atomizer in the ultrasonic fabric dewatering process (i.e the elastic response due to an applied electrical stimuli, and its influence on drying). Section 2 begins with the derivation of an analytical model for vibration analysis of a fully clamped piezoelectric atomizer, used in combination with electroelastic numerical models. A multiphysics axisymmetric finite element model (FEM) created for predicting acceleration is compared against the analytical model

and experimental data. Finally in this section, observations of the ultrasonic fabric drying process are discussed and the first drying rate model for wet fabrics exposed to ultrasonic vibrations is proposed. Section 3 discusses the detailed experimental methods used for data collection and the obtained experimentally validated modeling results. A 3-dimensional (3D) FEM is used for simulating complex boundary conditions. Next, the results of experiments and simulations of the models, as well as the process for identifying values of the coefficients used in a proposed drying-rate model, are discussed. These coefficients are related to the average transducer acceleration, creating a truly global relationship for predicting the drying rate of fabrics exposed to ultrasonic vibrations. Conclusions are summarized in Section 4.

2.2. Theory

2.2.1. Vibration analysis of a fully clamped piezoelectric atomizer; combined electroelastic analytical and numerical modeling

Schematics of the F100 symmetric piezoelectric atomizer used in experiments are shown in figure 2.1. The coordinate directions r, θ, and z are coincident with the 1, 2, and 3 piezoelectric directions, respectively. The atomizer was composed of annular piezoelectric rings adhered to the top and bottom of a stainless-steel plate and oppositely poled in the thickness direction (operating in the 33-mode of piezoelectricity). An electrode was bonded to the exposed surface of each PZT

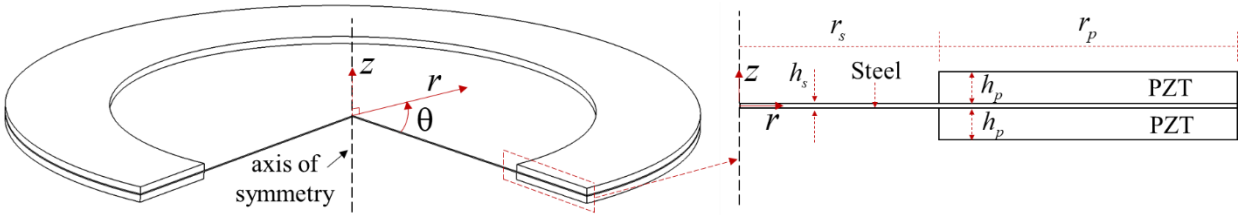

Figure 2.1. Schematic representation of an atomizer with annular piezoelectric rings adhered to the top and bottom of a stainless-steel plate.

layer and was connected in series. The PZT rings had thickness h_p and spans distance r_p, while the stainless-steel plate thickness was h_s and spanned across both r_s and r_p.

The PZT layers were actuated by a harmonic voltage input, resulting in thickness direction displacements. The stainless-steel substrate then experienced harmonic excitation from those displacements over the range r_p, where it was effectively constrained on the upper and lower surfaces. Because of these constraints, the forcing on the substrate was assumed to be uniform over r_p; this allowed a base excitation term to be applied at $r = r_s$. The constraints on the substrate at $r = r_s$ were approximated by clamped boundary conditions. The vibration of this clamped circular plate under axial base excitation was analyzed based on Kirchhoff's plate theory, as the radius/thickness ratio was large, deformations were assumed to be small, and the structure was assumed to show linear material behavior [31].

The governing distributed parameter partial differential equation for a damped circular plate is given as [31, 32]:

$$D\left(\frac{\partial^4 w_{rel}(r,t)}{\partial r^4}+\frac{2}{r}\frac{\partial^3 w_{rel}(r,t)}{\partial r^3}-\frac{1}{r^2}\frac{\partial^2 w_{rel}(r,t)}{\partial r^2}+\frac{1}{r^3}\frac{\partial w_{rel}(r,t)}{\partial r}\right)+c_a\frac{\partial w_{rel}(r,t)}{\partial t}+ c_s\frac{\partial \nabla^4 w_{rel}(r,t)}{\partial t}+\rho_s h_s\frac{\partial^2 w_{rel}(r,t)}{\partial t^2}=-\rho_s h_s\frac{\partial^2 w_b(t)}{\partial t^2} \tag{2.2}$$

where w_{rel} is the relative displacement of the plate due to the base excitation, defined as $w_b(t)=W_o e^{j\omega t}$, with W_o being the amplitude of excitation. The plate flexural rigidity is given as $D = Eh_s^{\,3}/12(1-\nu^2)$, where its Young's modulus and Poisson's ratio are E and ν, respectively. The mass density is denoted by ρ, thickness by *h*, and the subscripts *s* and *p* denote the steel and

piezoelectric layers, respectively. Viscous and structural damping coefficients are represented by c_a, and c_s in equation (2.2).

Therefore, equation (2.2) represents the distributed parameter elastic model of the circular plate in the transducer, and these equations can be solved using modal analysis.

To find characteristics of the transducer such as eigenvalues, mode shapes, and modal frequencies, we solved the partial differential equation governing the undamped free vibration EOM for a circular plate clamped about its circumference, given as [31]

$$D\nabla^4 w_{rel}(r,t) + \rho_s h_s \frac{\partial^2 w_{rel}(r,t)}{\partial t^2} = 0 \ . \tag{2.3}$$

Based on standard modal analysis, the relative transverse displacement can be represented as

$$w_{rel}(r,t) = \sum_{n=1}^{\infty} \phi_n(r)\eta_n(t) \ , \tag{2.4}$$

where $\phi_n(r)$ is the mass-normalized eigenfunction, and $\eta_n(t)$ is the time response in a modal coordinate for the *n*th vibration mode [31]. The spatial EOM became

$$\nabla^4 \phi_n(r) - \lambda_n{}^4 \phi_n(r) = 0 \ , \tag{2.5}$$

with λ_n representing the system's eigenvalue in the *n*th vibration mode.

The solution to equation (2.5) is a general shape function given as [31]

$$\phi_n(r) = C_{1n} J_0(\lambda_n r) + C_{2n} Y_0(\lambda_n r) + C_{3n} I_0(\lambda_n r) + C_{4n} K_0(\lambda_n r) \ , \tag{2.6}$$

where J_0 and Y_0 are the Bessel functions of the first and second kind, respectively, and I_0 K_0 are the modified Bessel functions of the first and second kind, respectively. Here the constants

$C_{1n},.....,C_{4n}$ and λ_n depend on boundary conditions. For a clamped-edge plate, the boundary conditions are given as

$$w_{rel}(r,t)\big|_{r=r_s} = 0 \quad \text{and} \quad \left.\frac{\partial w_{rel}(r,t)}{\partial r}\right|_{r=r_s} = 0 \ . \tag{2.7}$$

To avoid infinite values for Y_0, and K_0, the constants C_{2n} and C_{4n} must be zero because the Bessel functions of the second kind become infinite at $r = 0$. Then, applying the boundary conditions into equation (2.6) and using the known relations of Bessel functions [31], the mode shapes were found to be

$$\phi_n(r) = E_n\left[J_0(\lambda_n r)I_0(\lambda_n r_s) - J_0(\lambda_n r_s)I_0(\lambda_n r)\right] , \tag{2.8}$$

and we found the characteristic equation to be [31]

$$I_0(\lambda r_s)J_{-1}(\lambda r_s) - J_0(\lambda r_s)I_{-1}(\lambda r_s) = 0 \ . \tag{2.9}$$

The roots of equation (2.9) provided the eigenvalues, which in turn yielded the natural frequencies of the system as $\omega_n = \lambda_n^2 (D/\rho_s h_s)^{1/2}$.

The characteristics given by the previous undamped free vibration analysis were then used for the case of the damped forced vibration of the plate. The modal amplitude constant E_n in equation (2.8) must be evaluated for analysis of the damped EOM. This was done by normalizing the eigenfunction according to the orthogonality conditions, given as

$$\int_0^{r_s} 2\pi r \rho_s h_s \phi_n(r)^2 dr = 1, \quad \int_0^{r_s} 2\pi r D \nabla^4 \phi_n(r)^2 dr = \omega_n^2 \ . \tag{2.10}$$

The resulting modal amplitude constant was found to be [32-34]

$$E_n = \sqrt{\frac{\delta_{mn}}{2\pi\rho_s h_s \int_0^{r_s} r\left[J_0(\lambda_m r)I_0(\lambda_m r_s) - J_0(\lambda_m r_s)I_0(\lambda_m r)\right]\left[J_0(\lambda_n r)I_0(\lambda_n r_s) - J_0(\lambda_n r_s)I_0(\lambda_n r)\right]dr}} \quad .(2.11)$$

By following the modal analysis procedure [34], the damped partial differential EOM can be reduced to an infinite set of partial differential equations, given as [34]

$$\frac{\partial^2 \eta_n(t)}{\partial t^2} + 2\zeta_n \omega_n \frac{\partial \eta_n(t)}{\partial t} + \omega_n^2 \eta_n(t) = f_n(t) \ . \quad (2.12)$$

The damping ratio, ζ_n, was found for each modal frequency by analyzing empirical data with the half power method [34]. The modal forcing, $f_n(t)$ is given as

$$f_n(t) = -\rho_s h_s \left(\frac{d^2 w_b(t)}{dt^2} \int_0^{r_s} 2\pi r \phi_n(r) dr \right) . \quad (2.13)$$

The distributed parameter equation for a thin-plate transducer is given in physical coordinates in equation (2.2) and in modal coordinates in equation (2.12). If the base excitation of the plate is assumed to be harmonic in the form $w_b(t) = W_0 e^{j\omega t}$ (where the amplitude of the excitation is W_0 and $j = \sqrt{-1}$ is the unit imaginary number), and assuming linear oscillations, the steady-state expression for the modal response, $\eta_n(t)$, is expressed as

$$\eta_n(t) = A_n e^{j\omega t} \ , \quad (2.14)$$

Substituting equation (2.14) and (2.13) into equation (2.12) and cancelling terms, we find the expression for the complex amplitude, A_n. This information can then be used with equation (2.4) to derive the function for displacement at any point on the plate surface. Hence the closed-form steady-state expression for the transverse deflection of the plate is given as

$$w_{rel}(r,t) = \sum_{n=1}^{\infty} \phi_n(r) \frac{2\pi\rho_s h_s \omega^2 W_o \int_0^{r_s} r\phi_n(r)dr}{\omega_n^2 - \omega^2 + 2j\zeta_n\omega_n\omega} e^{j\omega t} \quad . \tag{2.15}$$

Taking the derivative of equation (2.15) twice with respect to time, the transverse acceleration of the plate at the geometric center, being the location of maximum acceleration for this axisymmetric system, was found to be

$$|a(0,t)| = \left| \sum_{n=1}^{\infty} -\phi_n(0) \frac{2\pi\rho_s h_s \omega^4 W_o \int_0^{r_s} r\phi_n(r)dr}{\omega_n^2 - \omega^2 + 2j\zeta_n\omega_n\omega} e^{j\omega t} \right| . \tag{2.16}$$

Equation (2.16) can be used for a circular plate, clamped and harmonically excited about its circumference for which classical plate theory is applicable.

The final step of the model was to choose an appropriate value for W_o, the magnitude of base excitation, and for ζ_n, the modal damping. Both the base excitation and damping terms were found through experimental data. The magnitude of base excitation velocity, for a harmonic voltage input to the transducer, was measured with a laser vibrometer; and the damping was found via the half-power method [35, 36]. Both were applied to equation (2.16) for each modal frequency range of $\left(\omega_n + \omega_{n-1}\right)/2 < \omega_n < \left(\omega_n + \omega_{n+1}\right)/2$.

To verify the analytical expression, we turned to the finite element software COMSOL Multiphysics, using the combined Structural Mechanic and electrostatic modules. This electromechanically coupled numerical model is an equivalent representation of figure 2.1 in which an AC voltage actuates the piezoelectric rings. Similar to the analytical model, it imposes

an axisymmetric response by solving a 2D model of the atomizer cross section with the bottom surface of the lower PZT fixed from displacement, denoting adhesion to a fixture.

For a thin, thickness-poled piezoceramic plate, the linear piezoelectric constitutive equations are [37-41]

$$S_3 = s_{33}^E T_3 + d_{33} E_3 \ , \tag{2.17}$$

$$D_3 = d_{33} T_3 + \varepsilon_{33}^T E_3 \ , \tag{2.18}$$

where S_3 is the strain, T_3 is the stress, D_3 is the electric displacement, and E_3 is the electric field. The elastic compliance at constant electric field is denoted by s_{33}^E (inverse of Young's Modulus), the strain constant by d_{33}, and the permittivity at constant stress by ε_{33}^T. These parameters are known for many piezoelectric materials, and the corresponding values are input into the material properties of the COMSOL simulation.

To ensure the FEM is accurate, an appropriate choice of element is vital. The default element shape is a tetrahedral, which will be used throughout the modeling process. Parameters of the elements that we are interested in testing are the order of the solution used to analyze the elements and the number of nodal points solved for each. Two orders of solution were tested, a quadratic and cubic solution; and two types of nodal configurations were examined, Lagrange and Serendipity. A Lagrange element has nodes along its exterior as well as its interior, whereas Serendipity elements have nodes only on their surfaces. Thus, Serendipity elements require less computation time than Lagrange elements. Four combinations of these parameter considerations were simulated and evaluated by the convergence of the predicted acceleration output. It was found that there were no deviations in response between Lagrange and Serendipity elements; therefore, Serendipity was chosen as the default nodal structure to decrease the computation time. Moreover,

an assumed cubic solution achieved convergence with a much coarser mesh than did the quadratic elements. Although the computation time for a cubic solution was longer per element, the drastic decrease in the total number of elements allowed for a more efficient simulation. Therefore, the element type chosen was a cubic Serendipity element ~1/8 mm in length. The resulting transverse acceleration of the transducer, as well as mode shapes and modal frequencies, were in strong agreement between both analytical and numerical models, as will be shown in Section 3.

2.2.2. Ultrasonic fabric drying model

Figure 2.2 shows several key moments in the ultrasonic fabric drying process. Figure 2.2a reveals the fixture that provides a boundary condition exhibiting the highest measured output acceleration (Appendix A). At this time step (t=0), 100 μL of water is being added to the fabric via a micro pipette. Immediately after actuation, the excess liquid that is not retained by the fabric coalesces with neighboring drops and is vigorously excited (figure 2.2b). Following quickly is the rapid atomization of these groups of water, evident by the decrease in size of the coalesced drops from figure 2.2b to 2.2c, as well as by mist being projected upward from the fabric. Moments later, the only liquid remaining on the atomizer is trapped within the fabric, and the drying process resembles figure 2.2d until all moisture is removed.

It can also be seen between figure 2.2b and 2.2c that the location of the cloth shifts slightly to the left. This shift is due to a layer of mist created by the sudden atomization, and it helps to temporarily separate the cloth from contact with the atomizer. The reduction in friction from loss of contact can shift the fabric by several millimeters. This movement is important, as the region containing the laser-cut liquid transport holes covers less than 20% of the total surface area; therefore, any displacement can move the fabric away from the locations of increased moisture

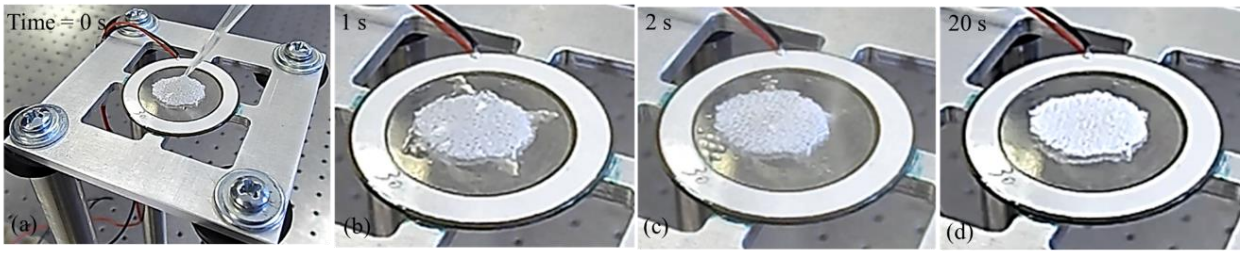

Figure 2.2. Snapshots of the ultrasonic fabric drying experiment process.

removal, causing the drying process to increase in duration. This is thought to be the main reason for differences in measured fabric weights between trials.

From this process, we can make two observations: (1) ultrasonic atomization begins with a rapid loss of the water not retained by the fabric, and (2) drying is more gradual following rapid atomization, as the availability of moisture decreases. These observations can also be well explained by relating the ratio between the surface tension forces and the excitation force. The threshold for atomization depends on the oscillating force that overcomes the surface tension. When this threshold is met, the liquid vapor boundary of the drop is broken and a mist is ejected. This can be quantified as a ratio, *R*, of the two forces, expressed as [6]

$$R \sim \frac{F_o}{F_s} \sim \frac{d^2 \rho_f a}{12\sigma \cos\beta} \tag{2.19}$$

where F_o and F_s are the magnitudes of the oscillation force and surface tension force, respectively; d is the drop diameter; a is the applied acceleration (given in equation (2.16) for fully clamped boundary conditions); and β is the contact angle formed between the drop and a solid support [6]. The minimum value of applied acceleration needed for atomization to occur is provided by equation (2.1). The surface tension decreases for larger drops; therefore, the coalesced liquid is first overcome by the oscillation, and atomization is realized almost instantly. Subsequently, moisture trapped in the larger pores is atomized until the remaining droplets are

small enough that their surface tensions are stronger than the excitation force. When this point is reached, thermal effects dominate, and the oscillation energy transferred through friction raises the temperature of the remaining moisture until evaporation occurs.

These two regions of drying—an initial rapid atomization of water followed by a gradual loss—have been denoted as nonlinear and linear regions, respectively. Moreover, studies have shown that there is a sharp transition between these two regions [4, 6]. The effects of changing acceleration while the atomization threshold is met are of the upmost interest in considering power efficiency; therefore, a model that relates changes in applied acceleration to changes in drying time is necessary to improve atomizer design.

The proposed fabric drying model consists of an exponential loss of water representing the nonlinear region, followed by a linear decrease in moisture content, expressed as

$$\begin{aligned} M(t) &= (M_{dry} + C) + (M_{sat} - C)e^{-\Omega t} \\ k &= \frac{M\big|_{t=t_{NL}} - M_{dry}}{t_L} \end{aligned} \qquad \begin{cases} 0 < t \le t_{NL} \\ t_{NL} < t_{dry} \end{cases}, \tag{2.20}$$

where $M(t)$ is the instantaneous mass of the fabric and any moisture it retains; M_{dry} is the bone-dry mass of the fabric; M_{sat} is the amount of water required to saturate the fabric; C is the limit of moisture content following the nonlinear region; Ω is the nonlinear drying rate; k is the linear drying rate; t, t_{NL}, t_L, and t_{dry} are the current time, duration of the nonlinear region, duration of the linear region, and total time to dry, respectively.

The model itself expresses important characteristics of the ultrasonic fabric drying process. The limit of moisture removal in the nonlinear region, denoted as *C*, is necessary, as atomization occurs only for drops for which the forcing ratio *R* is greater than unity. The fabric pores vary in size, but it can be assumed there is some Gaussian distribution of pore sizes. The limit *C* then

pertains to the water trapped in the smallest pore sizes where the surface tension is higher; thus, drop bursting does not occur.

Another characteristic is the sharp transition between the two regions. The model implies that the duration of the nonlinear region is constant at a given input acceleration, which has been observed to be true for the ultrasonic drying of various fabric types at constant acceleration [2, 10]. This hypothesis is tested by changing the actuation voltage and cloth size as described in Section 2.3. All further discussion of actuation voltage will be in reference to the peak-to-peak value.

For each magnitude of applied voltage tested, the empirical data are non-dimensionalized by dividing the measured mass by the bone-dry mass of the fabric, and dividing the time by the total time it takes to dry said fabric. Next, the non-dimensional version of equation (2.20) is fitted to the empirical data. The value of each parameter for the fitted curve will then be plotted against its corresponding applied acceleration for the trial, as each voltage input has a particular output acceleration. The regressions of these plots yield a relationship for each of the model parameters with the applied acceleration, from which the regressions are substituted into equation (2.21) and a global model for the drying rate of fabrics exposed to a given acceleration is found.

2.3. Results and discussion

2.3.1. Electromechanical analysis of a piezoelectric atomizer

Experiments were conducted for the investigation of two concepts: (1) identifying characteristics of the vibration of an ultrasonic atomizer for modal analysis and verification against electroelastic modeling, and (2) analyzing drying rate trends of wet fabrics exposed to ultrasonic vibrations. Bridging the results from these two concepts will provide a global electroelastic-drying model for predicting the applied acceleration and the corresponding drying rate, which will be

shown to be the only non-material parameters of the drying process. In this way, any boundary conditions of the atomizer or changes in dimensions can be simulated and an accurate estimate for drying time can be found.

To begin, the detailed geometry of the atomizer must be found before modeling. Microscopic images, using a Nikon Eclipse MA100 inverted microscope, were taken of the transducer cross section, as well as a top and bottom view of a central location (figure 2.3 c–d2). Figure 2.3c shows the annular PZT-5A rings adhered to the top and bottom of the stainless-steel plate. Figures 2.3 d1 and d2 show the array of laser-cut holes from a top and bottom view, respectively. These holes are conical in shape, in that the hole tapers in diameter from approximately 80 to 10 μm. The taper creates a pressure difference between regions above and below the plate, actively forcing moisture through the plate thickness and away from the fabric, where it can diffuse in the air. This design consideration greatly improves the moisture removal capabilities of the atomizer compared with a solid state transducer with no such permeability [6].

The atomizer is vacuum bonded to the fixture shown to ensure uniform adhesion; this bonding process is described in Anton et al. (2010) [42]. The fixture is a rectangular aluminum plate with a central hole of 21 mm, and 7 mm screw holes located at the corners of a 5×5 cm square. The central hole allows for the atomizer to be supported about the bottom PZT ring surface, whereas the stainless-steel plate is able to vibrate freely. A notch is created where the terminal leads would contact the fixture in order to isolate the flow of current.

To characterize fundamental properties of the transducer, an understanding of its response to electrical stimuli was needed. For this, the frequency-response function (FRF) of the atomizer to an AC voltage input was found to identify modal frequencies. A sine wave was generated with NI Signal Express and amplified with a Krohn-Hite model 7500 amplifier before the transducer

was actuated. The frequency of the sine wave was increased from 0 to 200 kHz, covering the manufacturer-reported resonance of 100 ± 8 kHz. Reflective tape was placed at the center of the transducer where a single-point laser doppler vibrometer (LDV; Polytec OFV 5000/505) measured the velocity of oscillation, from which the acceleration was calculated for the harmonic response of the plate (figure 2.3 a, b). Also measured was the FRF at various voltage amplitudes for the same frequency sweep.

Next, a scanning LDV (Polytec PSV 2000) was used to measure mode shapes, as well as the acceleration at multiple points. Reflective tape was placed over the entire stainless-steel plate surface area, a necessity to capture the increased density of sampling points over the area. An AC input at fixed frequency and amplitude actuated the atomizer, and the LDV measured the response at multiple points consecutively. This process was repeated for several voltage amplitudes; in this way, we were able to relate an input voltage to an output acceleration, effectively decoupling the electromechanical nature of the atomizer and providing a global parameter that can relate dissimilar atomizers. The mode shapes were used to verify the analytical model and FEMs, and the acceleration data will be vital for predicting the drying rates of fabrics.

An impedance curve was created using an HP4192a impedance analyzer. Those curves were used as a secondary verification for the modal frequencies found using LDVs. They also provided the resistance of the transducer for a particular operating condition and will be used for future comparisons of power efficiencies.

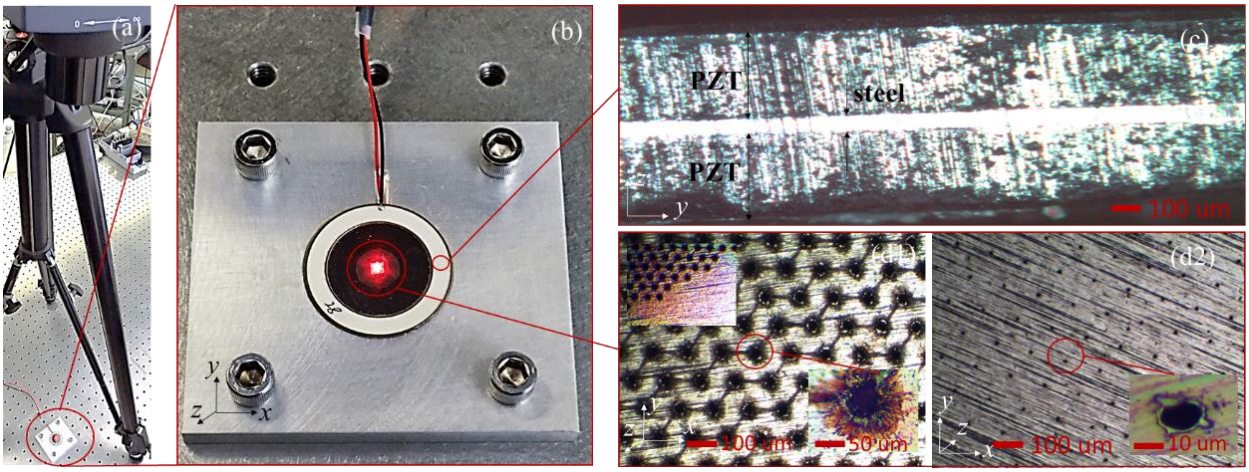

Figure 2.3. (a) Single-point laser vibrometer for measuring vibration response of the piezoelectric transducer (atomizer); **(b)** atomizer adhered to fixture; **(c)** cross section of the atomizer's outer radius; **(d1)** top view of laser-cut holes at center of atomizer; and **(d2)** bottom view of laser-cut holes.

For all the measurements discussed, seven different boundary conditions (in figure 2.A1) were tested; the results are shown in figure 2.A2. This allowed us to choose the arrangement and operating conditions that provide an acceleration that meets the atomization threshold and thus gives the fastest drying rate. The influence of various boundary conditions can be viewed in Appendix A.

Figure 2.4 shows the calculated acceleration at the center of the transducer for both the analytical model and FEMs, along with the experimental measurements. Information regarding the FEM can be found in Appendix C. Also shown in figure 2.4 is the curve described by equation (2.1), which is the threshold needed for atomization. It can be seen that the modal frequencies match nearly exactly, with only slight variations in amplitude and frequency between the solutions. These results also prove that axisymmetric boundary conditions and forcing yields an

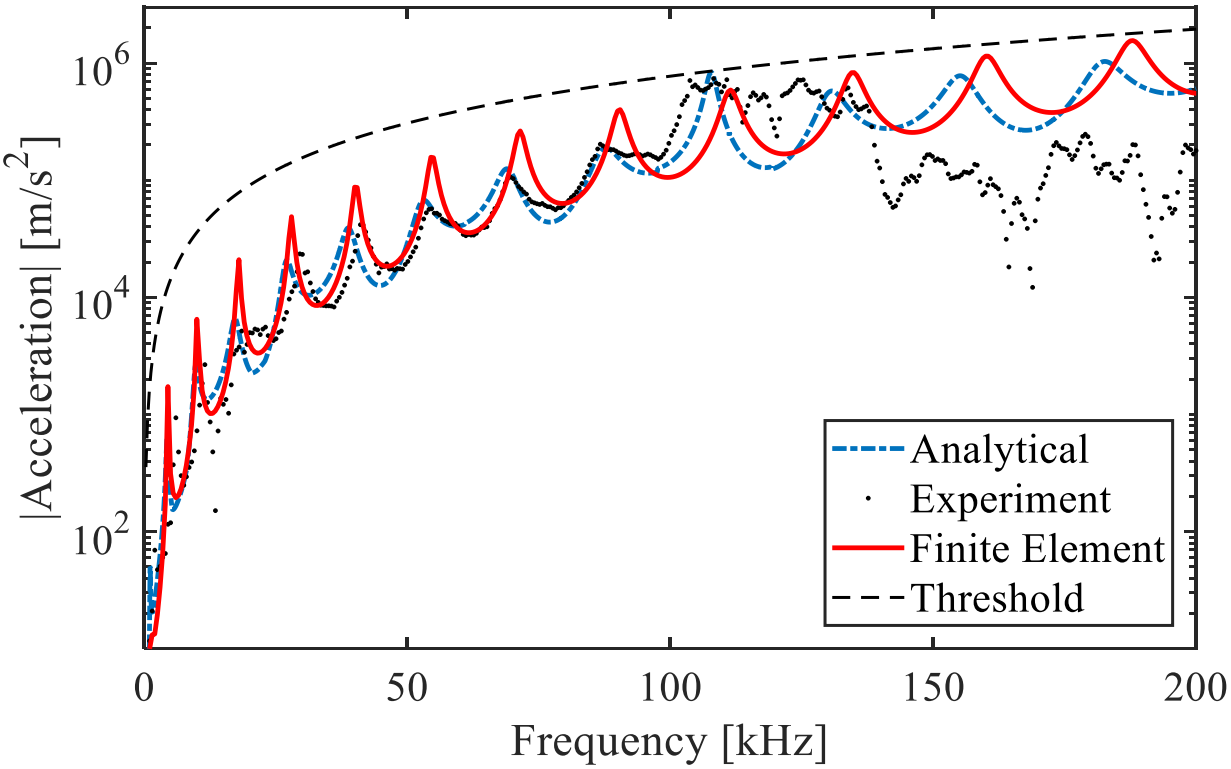

Figure 2.4. Experiment, analytical, and finite element simulation showing the acceleration at the geometric center of the transducer.

axisymmetric response. The results are accurate for frequencies up to 100 kHz, after which the response of the transducer is suspected to be nonlinear and thus cannot be captured by the analytical model or FEMs, which assume linearity. Comparing the experimental and analytical higher modes resonance frequencies shows less than 3% error. The major source of inaccuracy is unmolded effects (such as shear effects in the bonding layer) which can be manifested and pronounced in a mode shape-dependent way.

Note where the FRFs intersect the threshold for atomization, at approximately 105 kHz. This not only is within the manufacturer-reported range for operating frequencies that produce atomization, but also matches observations of when atomization occurs for drops of water excited at various frequencies. The agreement of the two models with experiment as well as observations proves the accuracy of the modeling techniques described.

Considering the breakdown in accuracy after 100 kHz, a new method of evaluating the output acceleration was needed. Since we had proved the models accurately captured the response of the atomizer, changes in the evaluation method pertained only to which parameters we were measuring and did not represent any intrinsic changes to the model. To resolve the issue, we compared the average acceleration over the stainless-steel plate found experimentally and with the FEM. Appendix B provides a more detailed analysis of this change in method.

A 3D FEM was used for the boundary conditions seen in the fabric drying experiment (figure 2.2a). Since the atomizer was no longer adhered to the fixture in an axisymmetric way, it was not appropriate to assume the same response would exist. We use the symmetry of the mounting condition to simplify the model. It can be seen that each quadrant of the fixture is identical; furthermore, we could divide the quadrant in half and still use symmetry to maintain the overall system properties. In this way, the model was reduced to 1/8 of its original size. A visual representation of the model and boundary conditions is provided by figure 2.5a. For each segment, symmetric boundary conditions are set at the edges. The boundary conditions in *z* direction (inward direction) are set as a combination of fixed, where the transducer is bonded to the base plate $w_{rel}(r,t)=0$, and free as shown in figure 2.5a.

The simulation results were obtained for the transverse acceleration of the stainless-steel plate area that makes contact with the fabric. The average acceleration was calculated from all the nodal points laying on this surface and integrated over the whole surface area.

As previously described, a scanning LDV measured the velocity at many sample points over the plate area. The average acceleration was calculated from these measurements, as the excitation was harmonic. Figure 2.5b compares the experimental results with the 3D FEM. It can be seen that the results match well; the two trends had a maximum difference of less than 6%. This

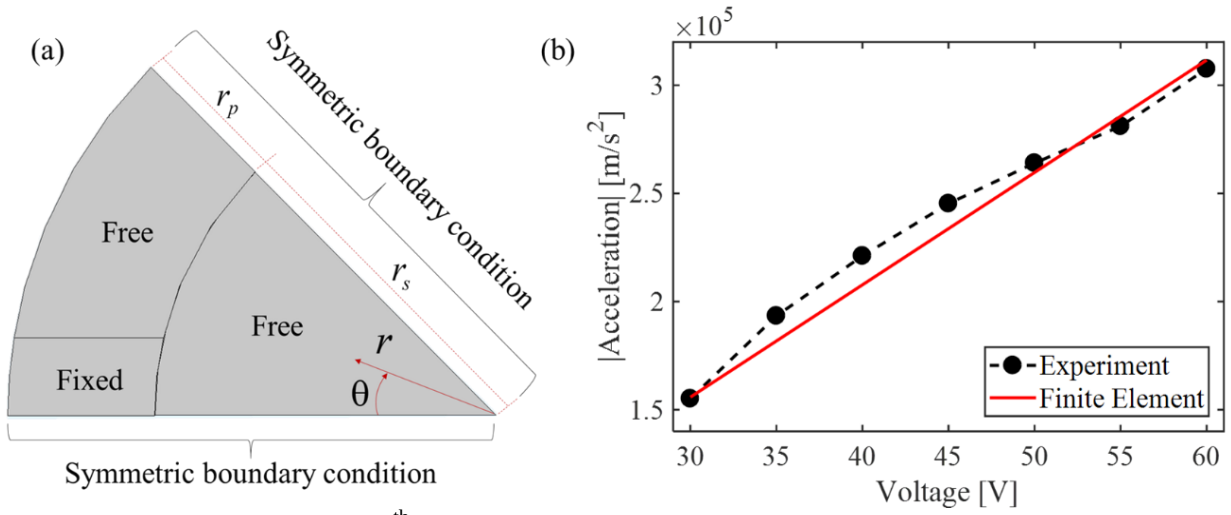

Figure 2.5. (a) COMSOL 1/8th transducer model, bottom view, displaying complex boundary conditions, and **(b)** experiment and finite element simulation showing average acceleration over the region bounded by r_s of the plate at a 107 kHz operating frequency.

information is used in the next section to globalize the input variable for the system. Input voltage to the transducer was originally the sole input to the models; however, this investigation presents a model that relates the applied voltage and output acceleration. Thus, we can relate the drying parameters of the system to the acceleration, following the description in the next section.

2.3.2. Ultrasonic drying rate analysis

Samples were cut from a Department of Energy standard test fabric, consisting of 50% cotton and 50% polyester [43]. The fabric was 0.40 mm thick and had an areal density of 190.9 g/m^2. Two different sizes of samples were tested, cut roughly into circles weighing 10 and 25 mg. Of these two sizes, four samples of each weight were cut and used during the experiment. The use of multiple fabrics reduced the number of cycles of wetting and drying each one experienced, helping to minimize fatigue and maintain fabric properties over the course of testing. This was found to be useful, as threads loosen with wear, affecting the absorbency of the fabric.

Fabrics were dried in the same manner as described in previous publications [4, 6]. Using a micropipette, 100 µL of water was added to the fabric resting on the atomizer. The atomizer was

activated for a given time interval. At the end of the run time, the sample was moved to a microbalance with tweezers and the total mass of the sample was weighed. Each time interval was tested three times, from which the average weight of the sample was calculated. Following the three tests, the time interval was increased and the process repeated. The intervals tested were 1, 2, 5, 20, 60, 120, 180, 240, and 300 seconds. After each test, the fabric was dried on a hot plate at 80°C to its dry mass.

Following the testing at all time intervals, a curve was assembled from the averages calculated. Then, the actuation voltage was changed and the entire process repeated. Peak-to-peak voltages tested ranged from 30 to 60 V in increments of 5 V. As previously mentioned, the acceleration output has been measured at various voltages. This allowed for the comparison of drying rate curves as a function of acceleration—a global variable, rather than of voltage—the influence of which is subjective, depending on the transducer. Note also that the 100 µL of added water was more than the fabric could retain; thus, some water remained on the atomizer outside the confines of the fabric pores. The initial oversaturation of the fabric was addressed in the proposed fabric model.

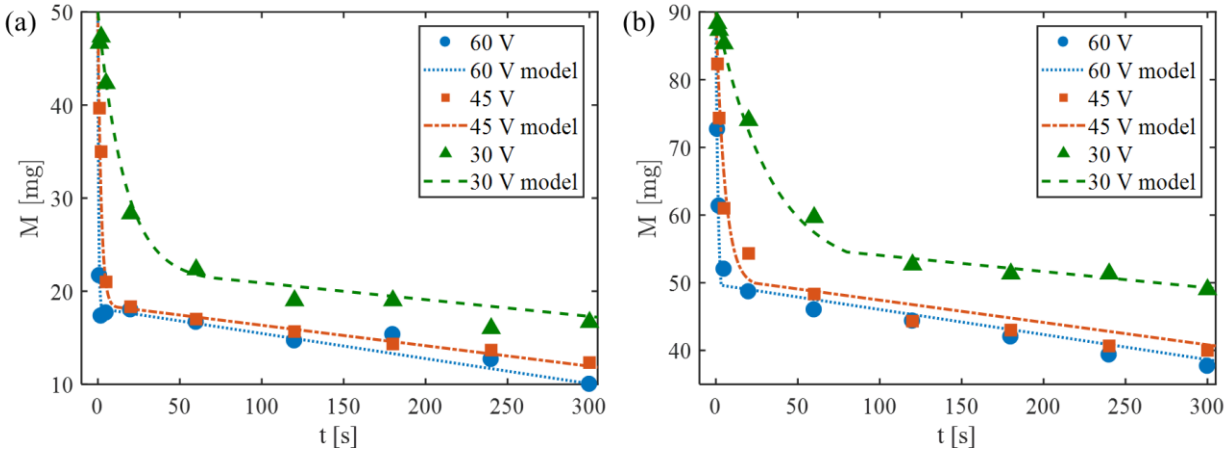

Figure 2.6. Experimental and model drying rates at 30, 45, and 60 V input voltage for **(a)** 10 mg, and **(b)** 25 mg cloth size.

The dimensional drying curves measured are shown in figure 2.6. The profound influence of applied acceleration (applied voltage is used as a proxy for acceleration) on fabric drying can immediately be seen. Furthermore, the accuracy of the proposed fabric drying model, equation (2.20), is easily seen. The saturation limit of each cloth is roughly four times its bone-dry weight. Most often, clothes being dried are not fully saturated; therefore, the starting mass would be lower than shown in figure 2.6 at t=0. However, since the time it takes to remove moisture from the saturation limit to approximately 20% of the limit is merely seconds, the model would still be accurate, as the total time scale for drying clothes is much larger. The parameters of the model were chosen with empirical evidence; it is necessary to do so, as no such model for the drying of fabrics with ultrasonic vibrations has been proposed previously.

It was earlier hypothesized that ultrasonic fabric drying would be dependent only on the applied acceleration and material properties. To test this, we non-dimensionalized the fabric drying model by dividing all terms expressing weight by the bone-dry weight of the fabric, and by dividing the current time by the total time it takes to dry the fabric. Thus, the model evolved so that the bar over the variables in equation (2.21) represents a parameter for the non-dimensional drying curve.

$$\begin{aligned} \bar{M}(t) &= (1+\bar{C}) + (\bar{M}_{sat} - \bar{C}) e^{-\bar{\Omega}\bar{t}} \\ \bar{k} &= \frac{\bar{M}\big|_{t=t_{NL}} - 1}{1-\bar{t}_{NL}} \end{aligned} \qquad \begin{cases} 0 < \bar{t} \le \bar{t}_{NL} \\ \bar{t}_{NL} < 1 \end{cases} \tag{2.21}$$

Figure 2.7 compares these non-dimensionalized curves; it plots together drying curves for two different-size fabrics exposed to the same average acceleration magnitudes. It can be seen that similar drying trends occur irrespective of the cloth size. The duration of the nonlinear region occurs for a constant percentage of the total drying time, given a constant acceleration. Also, for a

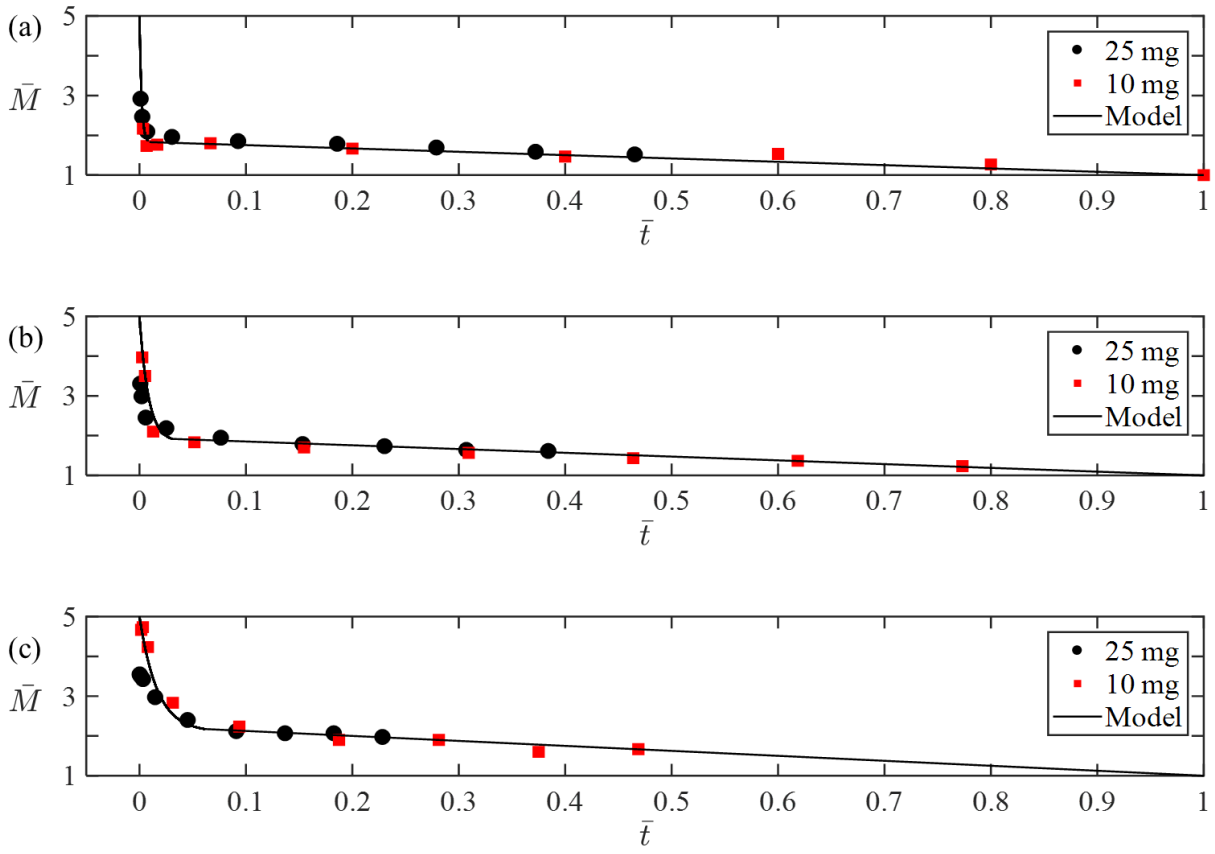

Figure 2.7. Normalized drying curves for **(a)** 60 V, **(b)** 45 V, and **(c)** 30 V actuation input voltage.

given excitation, the limit of nonlinear moisture removal is a constant multiple of the bone-dry fabric weight.

Moving forward, we expressed the non-dimensional fabric drying model coefficients as a function of the applied acceleration. Figure 2.8 compares these parameters against the average excitation acceleration. It can be seen that the nonlinear drying rate and total drying time are exponentially proportional to the applied acceleration, while the remaining parameters are linearly related. A previous study also came to the same conclusion that the atomization rate of water is exponentially proportional to the applied voltage [22].

Moreover, it was found that the total drying time was dependent on the fabric area. This result follows findings from studies investigating the thermal drying effects of fabrics of various

materials and sizes, which have found that the drying time is dependent only on the initial mass of water. Since a larger piece of cloth can retain more water, and the thickness of the fabric remained constant between testing periods, the changes in drying time can be related to the changes in area [44, 45].

The nonlinear drying parameters are also believed to be dependent on the area of the fabric. Evidence suggests each parameter is linearly related to area, however this study aimed to model the influence of acceleration only, where the testing of two fabric sizes was to ensure the accuracy of both data collected and the resulting models. The equations proposed in this study will be modified during future investigations to account for changes in area relative to the dimensions of the piezoelectric transducer.

From the relationships shown by figure 2.8, key parameters of the process, such as nonlinear drying limit and duration, can be expressed mathematically and related to observations made during drying experiments. The resulting relationships are applied to equation (2.22), yielding the first ever non-dimensional equation for the ultrasonic drying of wet fabrics, dependent only on applied acceleration and the surface area of the cloth, given as

$$\bar{M}(t) = (1 + \bar{C}_1 + C_2 a_{avg}) + (\bar{M}_{sat} - \bar{C}_1 - C_2 a_{avg}) \times \exp\left\{ -\bar{\Omega}_1 \, \mathrm{e}^{(1.58\times10^{-5} a_{avg})} \, t \Big/ \left[(\mathrm{Area}) t_1 e^{(-5\times10^{-6} a_{avg})} \right] \right\}. \tag{2.22}$$

This equation represents the nonlinear region of drying. Note that calculating the linear region is trivial, as the non-dimensional drying curve must reach unity for both non-dimensional time and normalized weight of the fabric. Because of differences in empirical data and the regressions, the model has a maximum error of 20% at low voltages; but as acceleration increases,

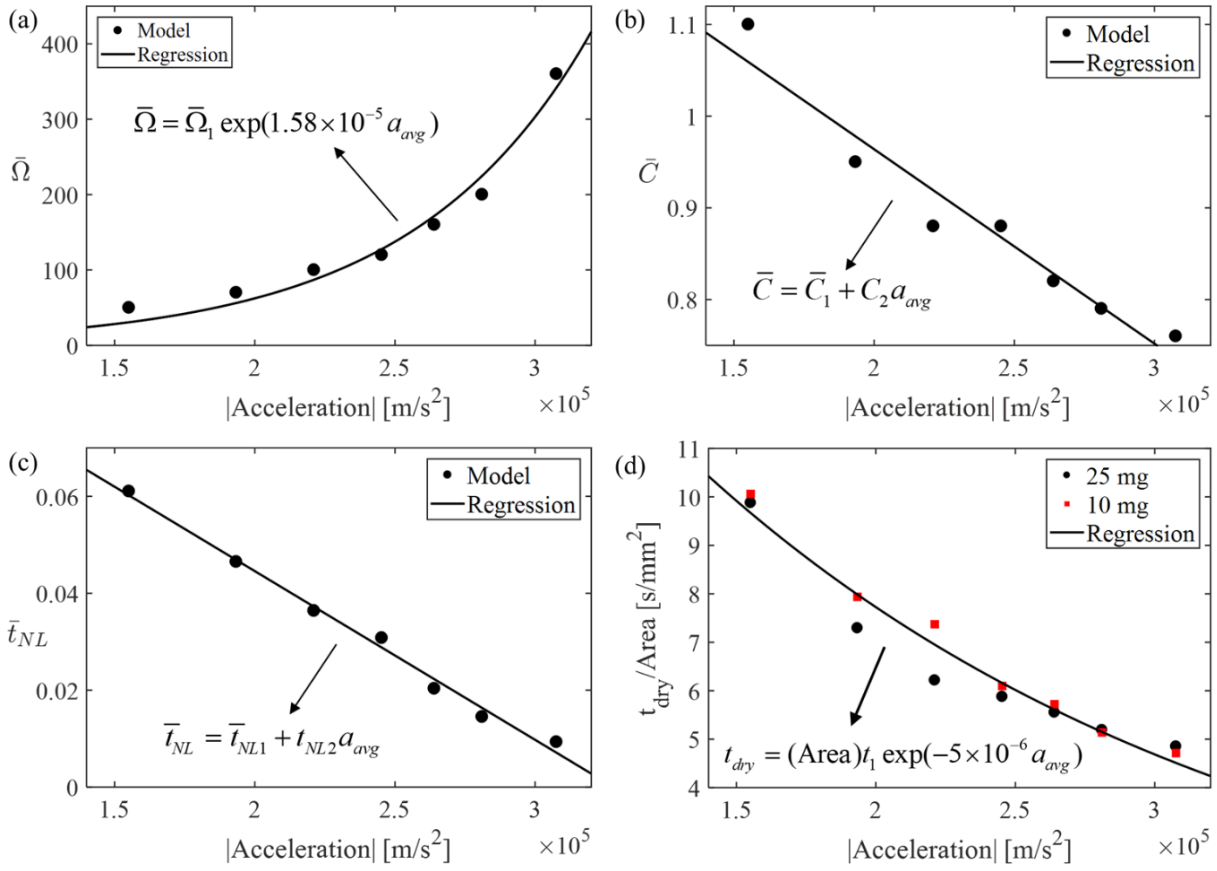

Figure 2.8. Non-dimensional drying rate model parameters as a function of average acceleration (a_{avg}) for **(a)** nonlinear drying rate, $\bar{\Omega}_1 = 2.65$, **(b)** nonlinear drying limit, $\bar{C}_1 = 1.4$, $C_2 = -2.1\times10^{-6}$ [s^2/m], **(c)** nonlinear duration percentage, $\bar{t}_{NL1} = 0.11$, $t_{NL2} = -3.5\times10^{-7}$ [s^2/m], **(d)** time to dry per unit of surface area, $t_1 = 21$ [s / mm^2].

the error decreases to less than 5%. The expression shows the dominance of acceleration over this process and is thought to hold true regardless of the device applying the acceleration.

The type of fabric being dried will also be a factor when developing equation (2.22). The acceleration needed to atomize water is related to the size of the droplet being excited. Since various fabrics have different distribution of pore sizes (the volume between threads) the amount of water lost in the nonlinear region will also be affected. It is believed that a correction factor accounting for the limit of atomization in the nonlinear region will be sufficient for applying this model to any type of fabric.

Equation (2.22) will serve to predict the mass of water loss from the fabric and the time it takes to shed this quantity. Used in conjuncture with the known electrical actuation signal, the drying efficiency is able to be calculated as a mass of water loss per watt of electrical input. Moreover this equation will allow for the instantaneous flow rate of water out of the fabric to be calculated by simply taking the time derivative. Analyzing equation (2.22) also allows for identifying parameters which control the shedding of water in the non-linear region of drying. By maximizing the water lost in this phase, the duration of drying will be greatly decreased due to the exponential relationship of water loss with output acceleration shown by figure 2.8a.

Conclusions

Although the feasibility of ultrasonic drying has been realized, the intricacies of the process are still of great interest. This chapter aims to analyze the physics of ultrasonic drying and proposes a global model that bridges the ultrasound transducer acceleration with the drying rates of wet fabrics. An electroelastic numerical model was created for predicting output acceleration and was verified against an experimentally validated analytical expression for an axisymmetric boundary condition. The numerical model was then modified to incorporate the complex boundary conditions used in benchtop drying tests and was shown to accurately predict average output acceleration. The average acceleration was then shown to govern all aspects of direct contact ultrasonic drying, allowing for the first-ever unified expression of drying rate dependent only on the transducer acceleration and contact area of the fabric. The development of ultrasonic drying technology can be built on these results through design changes in the device supplying the input acceleration.

The resulting relationships between parameters of the drying rate model and acceleration—i.e., the exponential relationship between applied acceleration and nonlinear drying rate (analogous to flow rate)—yield interesting characteristics of direct contact ultrasonic drying. This result, as well as the accuracy of predicting atomization using the critical acceleration threshold developed for free surface atomization, helps to explain the influence that a woven fabric has on dewatering phenomena.

From the known electrical input and its induced vibration response of the atomizer, and using the calculated drying time duration for which it is applied via the proposed drying rate model, will allow for the total energy consumption as well as the mass of water removed to be predicted. These two quantities allow for calculation of dryer performance as a metric of mass of water removed per unit energy consumed, being the industry standard for calculating efficiency. This aspect of the study is novel, as no such global model capable of predicting ultrasonic drying efficiency has been proposed in literature. This chapter provides a foundation for improving the direct-contact dewatering process of textiles. From this study, improvements in transducer design may greatly advance ultrasonic drying technology and allow for the application of this novel concept to a wide range of industries.

Appendix A: Influence of boundary conditions

The influence of mounting techniques on the atomizer's output acceleration is an important consideration, as they can improve performance without substantial design changes. These techniques are essentially a measure of the constraints imposed on the PZT rings' deformation. It was initially hypothesized that more constraints imposed on the PZT would lead to larger amplitudes of plate vibration. This is shown by fixture B in figure 2.A1, which has a mounting

plate on the upper and lower PZT rings. The inability of the upper PZT to be displaced in the thickness direction because of the extra fixture is thought to increase the forcing on the stainless-steel plate and, in turn, increase the displacement of the resonant modes. To test this hypothesis, two methods were used: (1) measuring the FRF of a central point on the atomizer and (2) performing an impedance analysis for each boundary condition.

The boundary conditions in figure 2.A1 are all adhered at locations on the PZT where contact is made with the fixture, with slight variations as follows: (A) adhesion on lower PZT, (B) adhesion on upper and lower PZT, (C) one notch removed, (D) four notches removed, (E) supported at four locations (inverse of D), (F) no fixture.

The results of an FRF for each boundary condition at constant voltage are shown in figure 2.A2. Previously, it was discovered that measuring the FRF at the center was an inaccurate way of predicting performance (see Appendix B for details). However, the differences in the amplitudes of the responses for frequencies less than 100 kHz accurately indicate performance differences when nonlinear influences are substantial. From figure 2.A2, it can be seen that fixtures with the least constraints are generally able to achieve higher output acceleration, with fixture "E" performing the best.

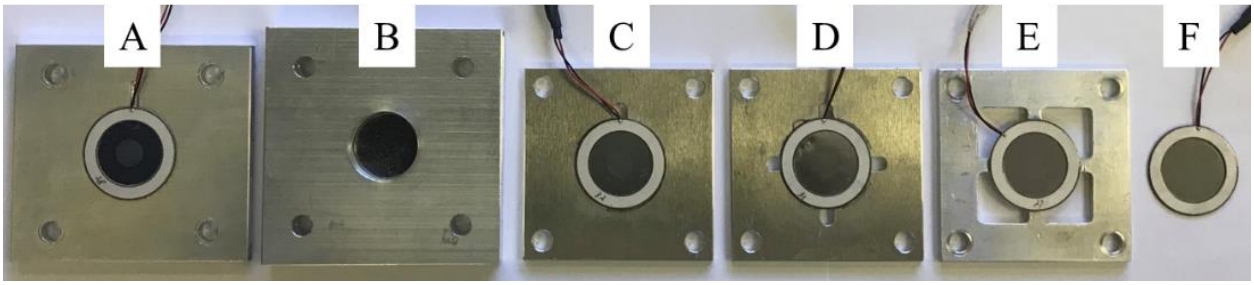

Figure 2.A1. Seven different boundary conditions investigated in the study.

Impedance analysis is another measure of the performance, similar to the FRFs shown in figure 2.A2. Figure 2.A3 shows these experimentally measured impedance curves. The difference in resonance and anti-resonance peaks of the curves is related to the magnitude of damping, where a large difference indicates relatively low damping. It can be seen that for fixtures with the least constraints, the damping is substantially lower than for those imposing more constraints. This follows the conclusions drawn from the FRFs. The curves are also useful for verifying the modal frequencies found with the analytical models and FEMs. Although the fixtureless atomizer, denoted "F" in figure 2.A1, performed very well, it is an impossible boundary condition to achieve in practice; therefore all ultrasonic drying was performed using boundary condition "E."

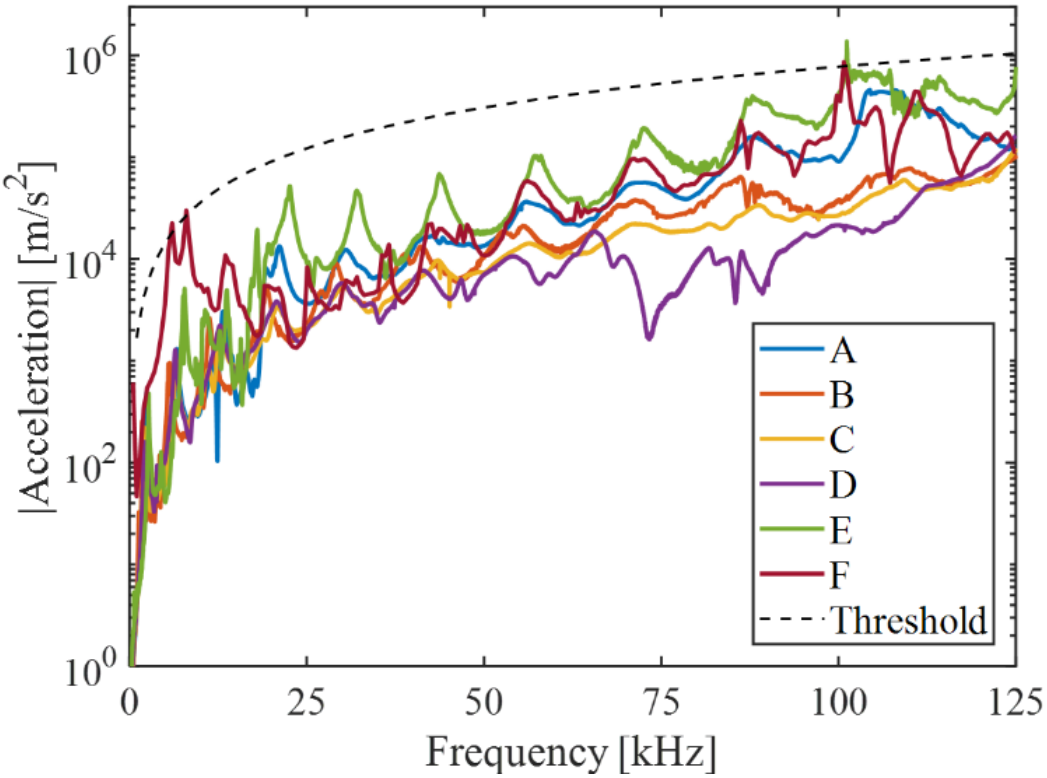

Figure 2.A2. Frequency-response curves of the investigated boundary conditions.

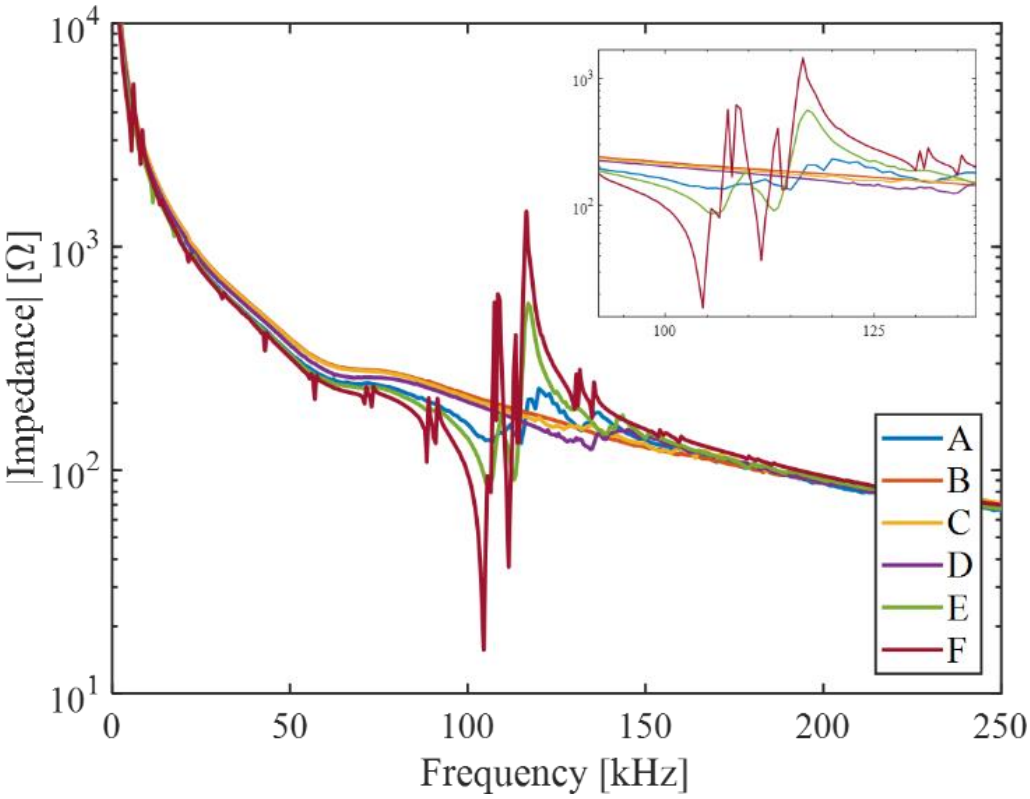

Figure 2.A3. Impedance curves of the investigated boundary conditions.

Appendix B: Average acceleration

Initially, the acceleration of the transducer was measured at the center of the stainless-steel plate, as axisymmetric mode shapes have a maximum displacement, velocity, and acceleration at the center. A plot of the FRF at this location to different voltage inputs is shown in figure 2.B1.

It can be seen that for frequencies less than approximately 60 kHz, there is very little deviation in response, other than in amplitude, when the voltage is changed. Also, for voltages of less than 25 V, there is very little change in response other than an amplitude changes for the entire range of frequencies tested; however, for frequencies above 60 kHz, as the voltage increases, there is a nonlinear softening that shifts the modal frequencies to a lower value. This softening is most easily seen at 85 kHz. When the excitation is increased past 100 kHz, the response of the system

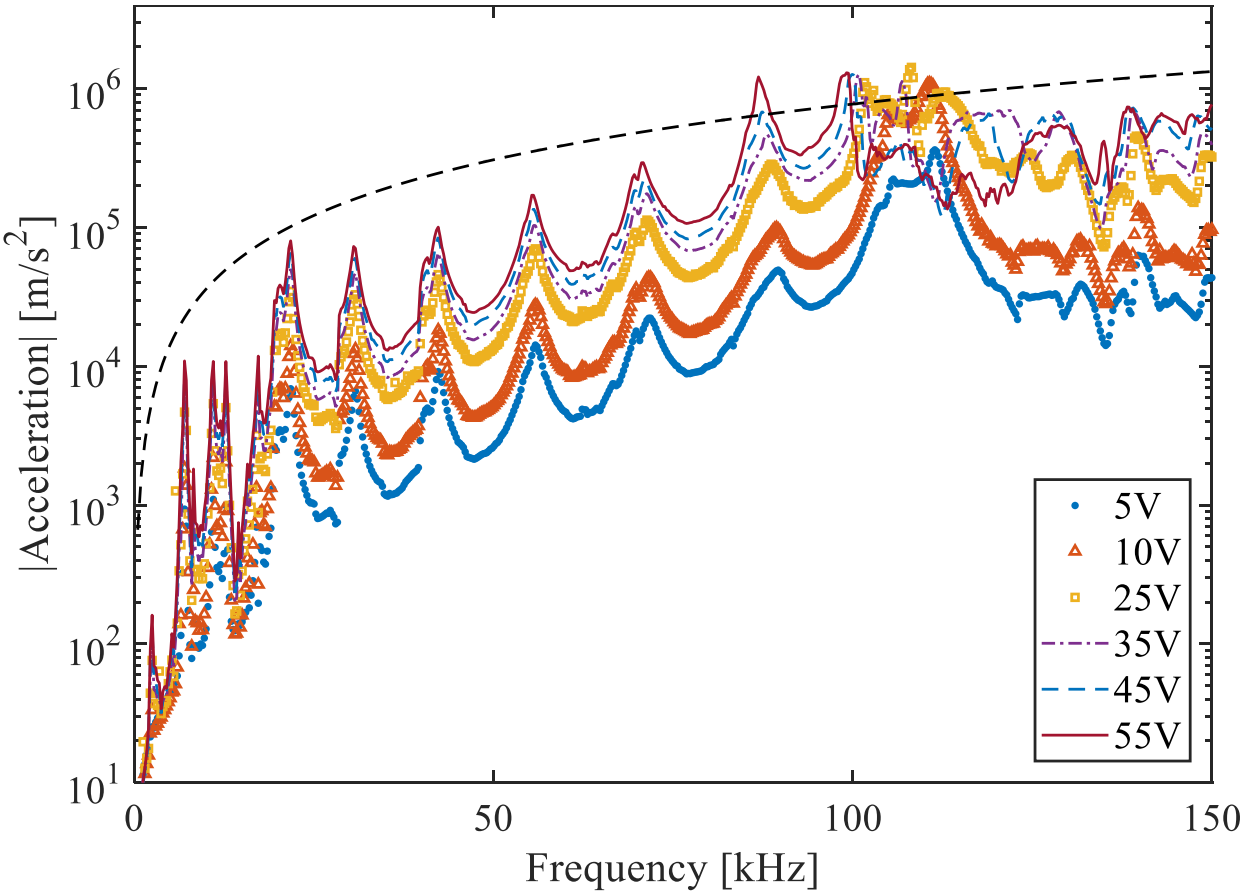

Figure 2.B1. FRF of the transducers center to various voltages.

at the center becomes chaotic. The data from figure 2.B1 suggest the maximum acceleration occurs at an input of 25 V and 107 kHz; however, this does not align with observations.

Experimental observations have shown that the atomization rate will always increase with larger magnitudes of input voltage so long as the atomization threshold is met, a finding supported by previous research [22]. To test the hypothesis that nonlinearities of the system influence the response at the transducer center, we measured the response of a point off-center. Measurements of a non-central point on the atomizer followed our observations of the atomization process: that increasing the voltage at 107 kHz yields a larger acceleration. From this data, we concluded that the mode shapes are no longer axisymmetric in this operating range.

Based on these results, we change the method of measuring performance to be more consistent in accounting for nonlinearities. To do so, we followed the method described in Section 3 of taking the average acceleration of many sample points measured with a scanning laser vibrometer. The resulting accuracy of this method between experiments and FEM simulations proved it to be valid solution (figure 2.5); furthermore, the clear relationships between the proposed drying model parameters and the average acceleration over the plate surface further justify this decision (figure 2.8).

Appendix C: Finite element modeling

Commercially available COMSOL Multiphysics is used for finite element modeling. This source of verification confirms the mechanical as well as the electromechanically coupled equations derived in this and the previous chapter. To begin, it is necessary to choose a mesh arrangement which accurately calculates the necessary results. Too coarse of a mesh will result in a lack of convergence to the true value, and too fine of a mesh wastes computational power. In this investigation, we will look at two types of elements, and two forms of assumed solutions for the nodes. The two elements tested are denoted as Lagrange and Serendipity. Lagrange elements contain interior nodes, or those that lay within the volume of the element, while Serendipity elements have nodes only on the exteriors; therefore, Serendipity elements do not take as much computation as the former type. We will assume a quadratic and cubic solution for the elements, where cubic solutions contain an extra node per edge than its quadratic counterpart. Figure 2.C1 shows a convergence plot for predicting output acceleration for four combinations of the Lagrange and Serendipity elements with quadratic and cubic assumed solutions.

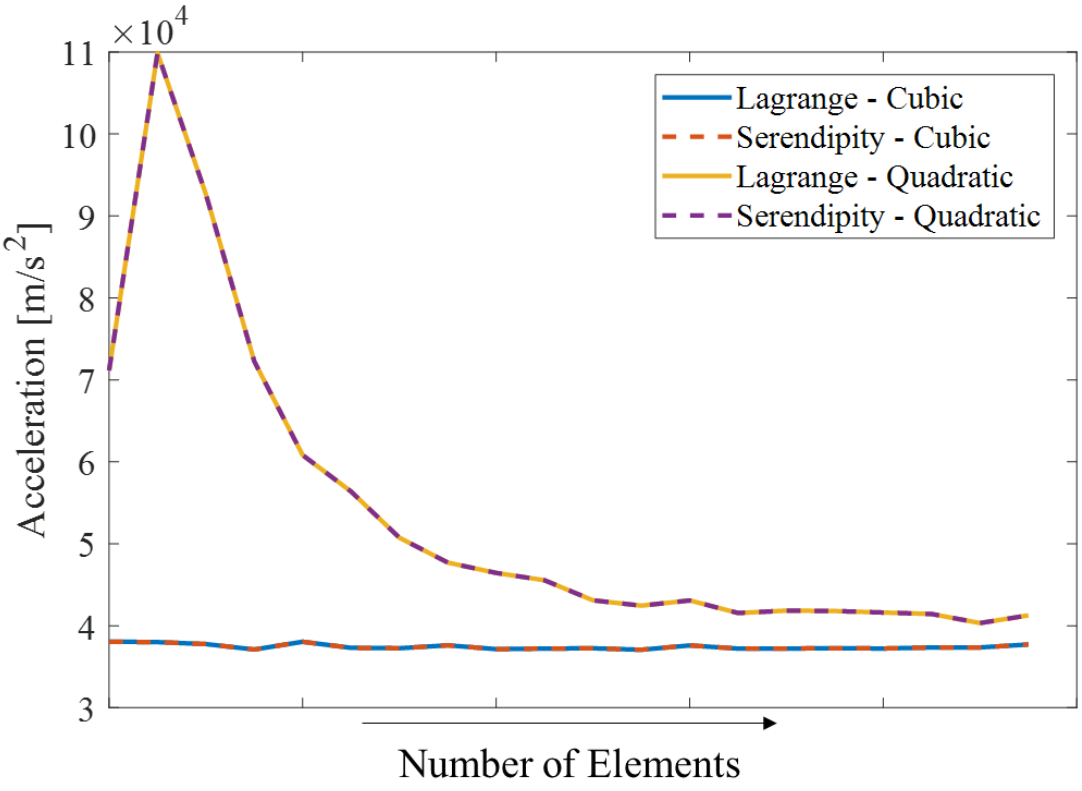

Figure 2.C1. Convergence study for four different configurations of FEM elements.

It can be seen that there is no differences in the converged values between Lagrange and Serendipity elements, therefore we will choose Serendipity elements due to the fewer number of nodes and faster computation time. It can then be seen that both quadratic and cubic elements converge to approximately the same value of output acceleration; however, an assumed cubic solution reaches the converged value with a significantly coarser mesh than the quadratic solutions. This is due to the higher order of accuracy contained in the polynomial each node is solving for. While this type of solution does take longer to compute, the far fewer elements needed makes for a more rapid simulation. Therefore, we choose cubic Serendipity elements in our model, of 1/8 mm in size.

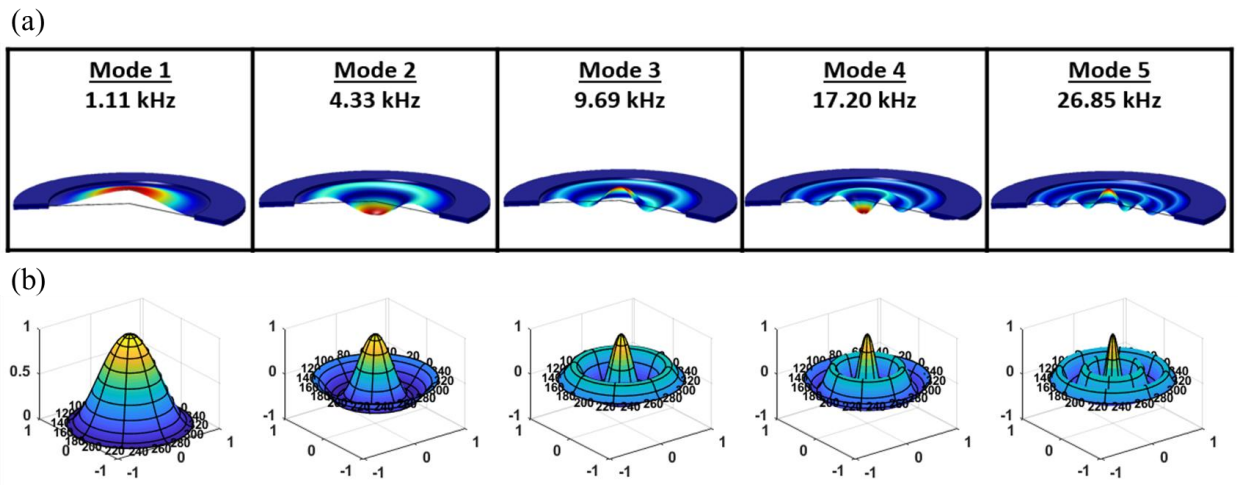

Figure 2.C2. Mode shape comparisons between a) FEM, and b) analytical predictions.

Validation of the analytical model using FEM was done through a comparison of modal frequencies and mode shapes. Figure 2.C2 shows the mode shapes for the first five axisymmetric modes. For each increasing mode, a radial node is gained in the response of the transducer. Between the FEM model and the analytical model, there are no differences in the predicted mode shapes.

Furthermore, an analysis of the first ten modal frequencies, covering the operating frequency of the transducer, shows an exact match between the analytical and FEM models, with the lowest accuracy being less than a 2% difference between the calculated values.

Mode	**1**	**2**	**3**	**4**	**5**	**6**	**7**	**8**	**9**	**10**
Analytical [kHz]	1.1121	4.3296	9.6998	17.2201	26.8892	38.7074	52.6742	68.7905	87.0553	107.4687
FEM [kHz]	1.1126	4.3307	9.8781	17.2156	26.8721	38.6651	52.5889	68.6367	86.9100	107.0734
% difference	0.038	0.025	1.821	0.026	0.064	0.109	0.162	0.224	0.167	0.369

Table 2.C1. Comparison of modal frequencies between the analytical and FEM models.

Bibliography

1. *Handbook of Industrial Drying*. Third ed, ed. A.S. Mujumdar. 2006: Taylor & Francis Group, LLC.
2. Bansal, P., K. Sharma, and S. Islam, *Thermal analysis of a new concept in a household clothes tumbler dryer.* Applied Energy, 2010. **87**(5): p. 1562-1571.
3. Stawreberg, L. and L. Nilsson, *Potential energy savings made by using a specific control strategy when tumble drying small loads.* Applied Energy, 2013. **102**: p. 484-491.
4. Peng, C., A.M. Momen, and S. Moghaddam, *An energy-efficient method for direct-contact ultrasonic cloth drying.* Energy, 2017. **138**: p. 133-138.
5. Momen, A.M., et al., *Dryer using high frequency vibration*. 2018, Ut-Battelle LLC.
6. Peng, C., et al., *Physics of direct-contact ultrasonic cloth drying process.* Energy, 2017. **125**: p. 498-508.
7. Letschert, V., et al., *Energy efficiency – How far can we raise the bar? Revealing the potential of best available technologies.* Energy, 2013. **59**: p. 72-82.
8. Wood, R.W. and A.L. Loomis, *XXXVIII. The physical and biological effects of high-frequency sound-waves of great intensity.* The London, Edinburgh, and Dublin Philosophical Magazine and Journal of Science, 1927. **4**(22): p. 417-436.
9. Bondy, C. and K. Sollner, *On the mechanism of emulsification by ultrasonic waves.* Transactions of the Faraday Society, 1935. **31**(0): p. 835-843.
10. Sollner, K., *The mechanism of the formation of fogs by ultrasonic waves.* Transactions of the Faraday Society, 1936. **32**(0): p. 1532-1536.
11. Burger, F.J. and K. Sollner, *The action of ultrasonic waves in suspensions.* Transactions of the Faraday Society, 1936. **32**(0): p. 1598-1603.

12. Lang, R.J., *Ultrasonic Atomization of Liquids.* The Journal of the Acoustical Society of America, 1962. **34**(1): p. 6-8.

13. Deepu, P., C. Peng, and S. Moghaddam, *Dynamics of ultrasonic atomization of droplets.* Experimental Thermal and Fluid Science, 2018. **92**: p. 243-247.

14. Avvaru, B., et al., *Ultrasonic atomization: effect of liquid phase properties.* Ultrasonics, 2006. **44**(2): p. 146-58.

15. Goodridge, C.L., et al., *Viscous effects in droplet-ejecting capillary waves.* Physical Review E, 1997. **56**(1): p. 472-475.

16. Goodridge, C.L., W.T. Shi, and D.P. Lathrop, *Threshold Dynamics of Singular Gravity-Capillary Waves.* Physical Review Letters, 1996. **77**(22): p. 4692-4692.

17. Vukasinovic, B., M.K. Smith, and A. Glezer, *Spray characterization during vibration-induced drop atomization.* Physics of Fluids, 2004. **16**(2): p. 306-316.

18. Vukasinovic, B., M.K. Smith, and A. Glezer, *Mechanisms of free-surface breakup in vibration-induced liquid atomization.* Physics of Fluids, 2007. **19**(1).

19. Yule, A.J. and Y. Al – Suleimani, *On droplet formation from capillary waves on a vibrating surface.* Proceedings of the Royal Society of London. Series A: Mathematical, Physical and Engineering Sciences, 2000. **456**(1997): p. 1069-1085.

20. Donnelly, T.D., et al., *An experimental study of micron-scale droplet aerosols produced via ultrasonic atomization.* Physics of Fluids, 2004. **16**(8): p. 2843-2851.

21. James, A.J., et al., *Vibration-induced drop atomization and bursting.* Journal of Fluid Mechanics, 2003. **476**.

22. Barreras, F., H. Amaveda, and A. Lozano, *Transient high-frequency ultrasonic water atomization.* Experiments in Fluids, 2002. **33**(3): p. 405-413.

23. Wilkes, E.D. and O.A. Basaran, *Drop Ejection from an Oscillating Rod.* Journal of Colloid and Interface Science, 2001. **242**(1): p. 180-201.

24. James, A.J., M.K. Smith, and A.R.I. Glezer, *Vibration-induced drop atomization and the numerical simulation of low-frequency single-droplet ejection.* Journal of Fluid Mechanics, 2003. **476**.

25. Ramisetty, K.A., A.B. Pandit, and P.R. Gogate, *Investigations into ultrasound induced atomization.* Ultrason Sonochem, 2013. **20**(1): p. 254-64.

26. Mir, J.M., *Cavitation-induced capillary waves in ultrasonic atomization.* The Journal of the Acoustical Society of America, 1980. **67**(1): p. 201-205.

27. Patel, V.K., et al., *Experimental evaluation and thermodynamic system modeling of thermoelectric heat pump clothes dryer.* Applied Energy, 2018. **217**: p. 221-232.

28. Yadav, V. and C.G. Moon, *Fabric-drying process in domestic dryers.* Applied Energy, 2008. **85**(2-3): p. 143-158.

29. Ng, A.B. and S. Deng, *A new termination control method for a clothes drying process in a clothes dryer.* Applied Energy, 2008. **85**(9): p. 818-829.

30. Tuğrul Oğulata, R., *Utilization of waste-heat recovery in textile drying.* Applied Energy, 2004. **79**(1): p. 41-49.

31. Rao, S.S., *Transverse Vibration of Plates*, in *Vibration of Continuous Systems*. 2007, John Wiley & Sons, Inc.: Hoboken, NJ.

32. Darabi, A., et al., *Bimorph disk piezoelectric energy harvester under base excitation: electroelastic modeling and experimental validation*, in *Active and Passive Smart Structures and Integrated Systems 2015*. 2015.

33. Aridogan, U., I. Basdogan, and A. Erturk, *Analytical modeling and experimental validation of a structurally integrated piezoelectric energy harvester on a thin plate.* Smart Materials and Structures, 2014. **23**(4).

34. Erturk, A. and D.J. Inman, *Base Excitation Problem for Cantilevered Structures and Correction of the Lumped-Parameter Electromechanical Model*, in *Piezoelectric Energy Harvesting*. 2011, John Wiley & Sons, Ltd: West Sussex, UK.

35. Shahab, S. and A. Erturk, *Coupling of experimentally validated electroelastic dynamics and mixing rules formulation for macro-fiber composite piezoelectric structures.* Journal of Intelligent Material Systems and Structures, 2016. **28**(12): p. 1575-1588.

36. Meirovitch, L., *Fundamentals of Vibrations*. 2001: McGraw-Hill.

37. Erturk, A. and D.J. Inman, *Appendix A: Piezoelectric Constitutive Equations*, in *Piezoelectric Energy Harvesting*. 2011.

38. Shahab, S. and A. Erturk, *Contactless ultrasonic energy transfer for wireless systems: acoustic-piezoelectric structure interaction modeling and performance enhancement.* Smart Materials and Structures, 2014. **23**(12).

39. Leo, D.J., *Piezoelectric Material Systems*, in *Engineering Analysis of Smart Material Systems*. 2008.

40. Sherman, C.H. and J.L. Butler, *Transducers and Arrays for Underwater Sound*. 2007: Springer Publishing Company, Incorporated. 612.

41. Shahab, S., D. Tan, and A. Erturk, *Hydrodynamic thrust generation and power consumption investigations for piezoelectric fins with different aspect ratios.* The European Physical Journal Special Topics, 2015. **224**(17-18): p. 3419-3434.

42. Anton, S.R., A. Erturk, and D.J. Inman, *Multifunctional self-charging structures using piezoceramics and thin-film batteries.* Smart Materials and Structures, 2010. **19**(11).

43. *10 CFR 430, 2013, "Energy Conservation Program for Consumer Products," Subpart B, "Test Procedures"; Appendix D/D1/D2, "Uniform Test Method for Measuring the Energy Consumption of Clothes Dryers."*. 2014.

44. Crow, R.M. and R.J. Osczevski, *The Effect of Fibre and Fabric Properties on Fabric Drying Times*, E.P. Section and P.S. Division, Editors. 1993.

45. Fourt, L., et al., *The Rate of Drying of Fabrics.* Textile Research Journal, 1951: p. 7.

Chapter 3

Coupling of electroelastic dynamics and direct contact ultrasonic drying formulation for annular piezoelectric bimorph transducers

Abstract

A newly developed technique for drying clothes without thermal energy has been developed through the utilization of ultrasonic vibrations from piezoelectric transducers. The novel technique incorporates the actuation of a thin stainless-steel disk in contact with wet fabric via annular piezoelectric rings, where water in the liquid form is atomized, transported through microchannels in the disk, and ejected as a mist. In such a system, resonance matching between the actuation portion of the transducer and the portion contacting fabric must be realized, with theoretical results from the developed electromechanical model showing a reduction in energy consumption by 50% when resonance matching is achieved. The electrically coupled distributed parameter model for an annular bimorph piezoelectric transducer is developed for optimization of ultrasonic drying technology. The thickness mode vibrations are shown to dominate the behavior of the system, where the analytically developed model can be optimized to increase the output acceleration of the transducer, thus increasing drying performance. The electromechanical equation developed will be connected to the drying rates of fabrics in contact with said vibrations, where the novelty of the coupled equations and its description of the physics of ultrasonic drying will be discussed.

Nomenclature

A	Area	a, b	Shape function coefficients
B	Temporal function coefficient	d	Piezoelectric charge constant

D	Electric displacement
$\bar{D}$	Plate flexural rigidity
E	Electric field
H	Piezoelectric enthalpy
$\bar{H}$	Heaviside function
h	Thickness
j	Unit imaginary number
K	Kinetic energy
k	Spring constant
L	Bimorph total thickness
m	Mass per unit length
r	Radial coordinate
S	Strain
T	Stress
t	Time
U	Potential energy
u	Displacement
V	Voltage
$\bar{V}$	Volume
x	Thickness direction coordinate
Y	Young's Modulus
α	Bimorph eigenvalue
ε^S	Permittivity at constant strain
ζ	Damping ratio
η	Bimorph temporal function
θ	Angular coordinate
λ	Plate eigenvalue
ν	Poisson's ratio
ρ	Mass density
ϕ	Bimorph shape function
Ψ	Plate shape function
Ω_n	Plate natural frequency
ω	Excitation frequency
ω_n	Bimorph natural frequency

Subscripts

ef	Elastic foundation
f	Fabric
i	Material layer index
n	Mode number index
p	Piezoelectric
s	Substrate
3, 33	Thickness direction

3.1. Introduction

The proposed experiments and experimentally-validated multiphysics modeling approach in this thesis aim at filling a knowledge gap in terms of considering distributed parameter models of piezoelectric bimorphs, associated with actuation and sensing, for the purpose of direct-contact ultrasonic clothes drying. The significant impacts of this research are analytical expressions for thickness-mode piezoelectric bimorph actuation coupled with the drying rate of fabrics in contact with the resulting ultrasonic vibrations, for the development of the next generation clothes dryer. The developed analytical expressions enable optimization to be performed efficiently, and the approach taken allows for the splitting of a transducer with a non-uniform geometry. This research will be the first attempt to establish a mathematical framework and experiments to predict the

effectiveness of a piezoelectric transducer applying ultrasonic vibrations to a wet fabric for de-watering. The proposed research will also tackle the problem of modeling bimorphs without the use of finite-element or lumped parameter methods as is commonly used [1-5].

Regular electric resistance clothes dryers, accounting for 80% of all dryer sales and found in over 200 million American homes, are an electrically wasteful appliance [6]. Upwards of 5% of the electricity consumed by residential buildings per year is done in the form of clothes drying. A much larger volume of air than the clothes occupy must be heated and sealed from leakage, and when the humidity inside the drum rises, much of that energy is expelled. The resistance of sealing rings against the rotation of the drum increases the power demand on the driving motor, further reducing energy efficiency.

Recently, other clothes drying methods have been introduced, which can significantly increase the efficiency associated with clothes drying. These methods include heat pump drying, recirculation, control systems, and even thermoelectric materials in an attempt to improve thermal drying technology from the likes of electric-resistance drying [7-12]. Heat pump dryer technology has significantly improved when compared to other methods, achieving upwards of 6 lbs of clothes dried per kWh of electricity, which is significantly higher than electric resistance dryers, which can only reach 3.7 lbs/kWh, being the legal minimum. However, heat pump dryers have not been popular in the U.S. due to higher initial costs and longer dry times [13]. Yet, there is a growing need for efficient appliances to help reduce emissions resulting from the production of electricity.

The limiting factor for efficient thermal clothes dryers stems from the properties of water. The high latent heat of vaporization of water requires a large amount of thermal energy to evaporate it from fabrics. Regardless of the advancements made in how heat is supplied to the dryer, the bare minimum energy requirement, being the latent heat of vaporization, dramatically

reduces the maximum efficiency possible when drying clothes with thermal energy. Therefore, a different mechanism of drying is proposed in order to vastly improve the efficiency of fabric drying technology.

The novel solution for energy-efficient clothes drying bypasses the need for thermal energy by utilizing a process called atomization: a mechanical process in which oscillated liquids can eject nanometer-sized droplets from its surface when exposed to sufficient magnitudes of acceleration, figure 3.1a. Droplet ejection during atomization is characterized by several instabilities due to free-surface breakup, mainly Rayleigh-Taylor, Rayleigh capillary, and Faraday-wave instabilities [14-16]. Piezoelectric based atomization technology is commonly used for aerosol drug delivery, medical-tool sterilization, humidifiers, food dehydration, and recently as a replacement for ink-jet printing due to the well-controlled sizes of the ejected droplets [17-20]. Due to the commonality of this technology and lack of recent advances, little attention is paid to atomization applications other than those where controlled droplet sizes are needed, mostly regarding industrial applications rather than consumer products. However, over the past several years atomization has been found to be ideal for the drying of fabrics, as no thermal energy is necessary due to the mechanical nature of this method.

The mechanics of atomization are well studied and were first observed in the late 1920's by Wood and Loomis [21]. Since then, many investigations have confirmed the relationships between the driving frequency of the liquid and the formation of capillary waves on its surface, as well as the prediction of droplet diameters [14-16, 18, 19, 22-25]. The accuracy of these relationships has resulted in a single expression for the acceleration necessary to achieve atomization as [16]

$$a_c \approx 0.261\omega^{4/3}(\sigma/\rho)^{1/3}\ , \tag{3.1}$$

where ω is the driving frequency, σ is the surface tension, and ρ the fluid density.

For a wet cloth, liquid droplets are contained within the fabric pores, which vary in size within a given fabric as well as between types of textiles. As the sizes of the drops vary within the fabric, so does their surface tension, effectively changing the acceleration necessary to achieve atomization. When atomization does occur, the ejected droplets are able to pass between fibers of the fabric and are expelled by their own momentum. By oscillating the fabric with sufficient intensity, the majority of water is able to be atomized and ejected, while the droplets retained in the smallest fabric pores remain as their surface tension is unable to be overcome. These smaller droplets are then evaporated due to the thermal energy resulting from the movement of the fabric, as friction between fibers increases the local temperature of the cloth [26]. This method was put into practice in 2016, where researchers at Oak Ridge National Laboratory created the first piezoelectric based clothes drying prototype and identified many characteristics of ultrasonic clothes drying [26-29]. The concept for the stages of atomization is show in figure 3.1a.

Previous investigations by this dissertations authors highlighted the predictability of ultrasonic drying performance given only the applied acceleration contacting the fabric to be dried [30-32]. A key finding was the ability of vibration-based models of the actuating structure to predict the drying rates of fabrics it is in contact with based upon its deformation acceleration. However, the previous publications relied on experimental data to supplement a missing portion of a piezoelectric transducer model. In this thesis, the same vibration model is completed by coupling the electroelastic actuation of an annular bimorph with the resulting plate vibrations which are further coupled to the fabric drying rate. Moreover, the novelty of the developed electroelastic models exceeds the application of ultrasonic drying and is useful in many other fields using piezoelectric systems as sensors or actuators.

Vibration-based models of small-scale piezoelectric systems have been an increasingly popular research area for a wide range of applications including energy harvesting, controls, structural health monitoring, and contactless acoustic energy transfer systems, among others [4, 33-37]. Of these applications, space and energy availability are often limited, making self-powered, wireless networks highly desirable. Electromechanical models relating the coupled inputs and outputs, being an electrical signal and mechanical deformation, are necessary for the optimization of systems to approach the high efficiencies that define the piezoelectric materials utilized.

The majority of vibration-based research of piezoelectric structures is related to energy harvesting, where large amplitudes of deflection are desired to maximize the electrical energy produced. As such, these models are often based on cantilevered structures with orthogonal electromechanical coupling between poling and forcing directions [1, 2, 4, 33, 38-43]. For cantilevered structures, distributed parameter models developed analytically have been heavily favored in literature [44, 45]. A hindrance to these forms of models arises from systems with complicated boundary conditions, often rendering analytical expressions near impossible to develop, forcing the use of finite element analysis. However, the optimization qualities of analytical expressions make these solutions more valuable [3]. For single degree of freedom systems, such as tuned-mass-dampers and instances where poling and forces are in the same direction, the method of using lumped parameters is often used for complex geometries [1-5].

A knowledge gap regarding modeling was found for systems with poling and forcing along the same axis, using the distributed parameter approach. As previously stated, these systems are often modeled using lumped parameters, however this method does not allow for accurate analysis of design changes with regards to an annular bimorph structure. Furthermore, the majority of distributed parameter models assume bending is the dominant deformation [33, 39]. Therefore,

there is a need for distributed parameter analytical models of piezoelectric transducers where electromechanical coupling is along the same axis and bending is not a dominant deformation. This investigation will fill this gap in knowledge by providing a straightforward approach for distributed parameter modeling of an annular bimorph operating in the 33-mode of piezoelectricity. Furthermore, the developed models will be connected to the drying rate of wet fabrics in contact with ultrasonic vibrations.

The significant goal of energy-efficient clothes drying will be approached through optimizing the mechanics of the device supplying the atomization energy. In this and previous [30] investigations, a particular meshed transducer was selected which consumed ~1W of power per transducer, including the losses due to the power electronics. Estimates place the number of transducers needed for a full-scale dryer in the hundreds, meaning approximately 0.4 kWh of power is consumed for a typical drying cycle. Through the optimization of the transducer and its boundary condition, this study will show the same amount of drying can be achieved with half of the estimated power. This drastic increase in energy savings demonstrates the need and novelty of the coupled electroelastic equations modeling the actuating transducer and connected to the drying rate of fabrics it is in contact with.

The objective of this research is to improve the fundamental understanding of the ultrasonic fabric drying process and apply the results to the ongoing development of a new and disruptive fabric drying technology, which will have a significant impact on the overall energy consumption attributed to clothes drying around the world. The work is novel because it involves an analytical, distributed parameter model for predicting the vibration characteristics of an annular piezoelectric bimorph transducer in resonance with a thin plate coupled with drying characteristics of fabrics in contact with the resulting vibrations, giving physical insight into direct contact ultrasonic drying

and atomization and progressing this application. Many of the previous approaches in the literature for this type of vibration research have resorted to finite element modeling (due to complicated boundary conditions) and lumped parameter methods, making them inaccurate and difficult to use for optimization (unlike our approach). In addition to these advantages, the modeling approach described in this thesis also involves electromechanical coupling between the electrical input and the resulting mechanical deformation of the bimorph. By combining these results with previous empirical results on ultrasonic fabric drying, this research represents the first complete model of ultrasonic based fabric drying, to the authors' knowledge. Using this model, an electrical input with particular frequency and amplitude can be used to accurately predict the vibration of the piezoelectric bimorph transducer, which can, in turn, be used to determine the expected energy consumption and drying time for a given fabric. The results are valuable for advancing the state-of-the-art ultrasonic drying technology, as they allow for the design and optimization of piezoelectric transducers for maximum energy efficiency and minimum drying time.

In this study, we investigate the electrical actuation of a disc-type, annular piezoelectric transducer, and the resulting deformations. Section 2 begins with analytical modeling, using Hamilton's principle and common techniques in vibrations analysis. A single expression for the displacement of the bimorph as a function of material properties and applied sinusoidal voltage will be developed. This expression will then be connected to previous modeling investigations of the transducer by the authors. Section 3 discusses the experimental techniques used to validate the electroelastic models, as well as a comparison of the transducer's measured response with that of the developed models. The two important deformation characteristics being the bimorph displacement and resulting plate acceleration. In Section 4, a proposed design solution based upon the developed models will be shown to aid in resonance matching and drastically increase the

output acceleration of the transducer. The effect on acceleration will be connected to theoretical drying rate of fabric it is in contact with, highlighting the immense capabilities of direct contact ultrasonic clothes drying.

3.2. Theory

The bimorph piezoelectric transducer, shown in figures 3.1a and b, is comprised of a single thin stainless-steel disk as the substrate; adhered to the top and bottom surfaces of the disk are annular Lead Zirconate Titanate (PZT-5A, PZT) actuators, thickness poled in a direction away from the substrate. Terminals located on the exposed surfaces of the upper and lower PZT rings connect the system in series, with the substrate modeled as a perfect conductor. All components have equal outer radii of 15 mm while the annular PZT layers also have an inner radius of 10.5 mm. The substrate thickness is 0.05 mm and the PZT layers are 0.32 mm thick. The following model is based on a commercially available transducer used in this and previous ultrasonic drying investigations [46]. An investigation into the effects of changing the PZT material can be found in Appendix A.

The bimorphs electromechanical coupling is largest in the thickness direction and seeing as the electric field is applied in the same direction over a small distance relative to the width of the bimorph, we can assume piston-like motion at resonance [47]. This assumption results in constant displacement over the range $r_i \le r \le r_o$, for any given value of x.

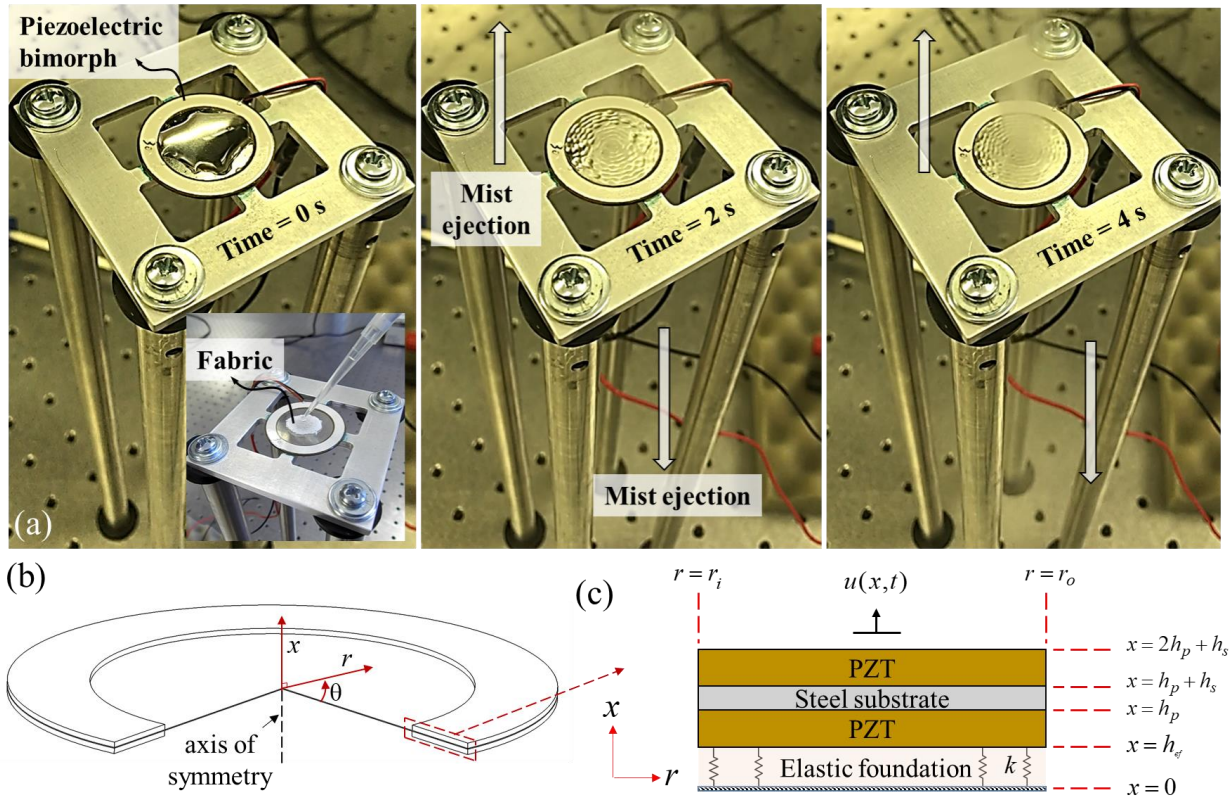

Figure 3.1. (a) Stages of atomization, **(b)** piezoelectric transducer schematic, and **(c)** a cross-section of the bimorph portion resting on an elastic foundation with spring constant k.

The transducer is mounted to an aluminum plate with a central hole of radius equal to that of the inner PZT radii; this ensures no contact is made between the vibrating plate and the fixture. The bottom surface of the transducer's bimorph portion is mounted to the fixture using a two-part epoxy (3M DP460) utilizing a vacuum bonding process to ensure proper contact and adhesion between the fixture and transducer [48].

A distributed parameter model of the dynamics of the transducers is developed in two parts: (1) electroelastic actuation of the bimorph portion of the transducer (figure 3.1c) due to an applied electric signal, and (2) the resulting plate vibration of the unconstrained stainless-steel substrate over the range $0 \le r < r_i$. The analytical approach requires separation of the model into two parts

due to the orthogonal distribution of the boundary conditions and geometric variables χ and r, used in each model, as defined in figure 3.1b.

Modeling of the bimorph is achieved using Hamilton's method, given by the expression [47, 49, 50]

$$\int_{t_1}^{t_2}\left[\delta\int_{\bar{V}}\left(K-U\right)d\bar{V}\right]dt=0\ . \tag{3.2}$$

This method considers a balance of potential and kinetic energies using variational methods, an ideal approach for the small displacements and steady state behavior of the piezoelectric actuator considered here. For this derivation we ignore the work due to non-conservative forces, being the charge held over the terminals, as it only influences the circuit equations which are not pertinent in this derivation. The potential energy has four total contributions; two are identical due to the electric enthalpy of the PZT layers, one is due to the substrate, and the last from the epoxy layer being modeled as an elastic foundation with a spring boundary condition constraining the transducer to the fixture. Therefore, the total potential energy is expressed as

$$U=H+U_s+U_{ef}\ . \tag{3.3}$$

Due to the axisymmetric geometry of both the transducer and the boundary conditions, as well as the small strain assumption of linear piezoelectricity, the volume integrals are reduced to line integrals with the area in the $r-\theta$ plane remaining constant [51, 52]. This assumption is known as piston-like motion, and is typically valid for materials with aspect ratios greater than 20 [53-55]; in this case the PZT layer has an aspect ratio of 14, however we will show the piston-like motion to hold true and provides an accurate model. For the bimorph, the area in this plane is represented as $A=\pi\left(r_o^2-r_i^2\right)$. Following this assumption, each potential energy term can be expressed as

$$\int_{\bar{V}} H = \int_{\bar{V}} \left(U_p - E_3 D_3\right) d\bar{V} = A \int_{h_{ef}}^{h_{ef}+h_p} \left(\frac{1}{2} Y_p S_{33}^2 - Y_p d_{33} E_3 S_{33} - \frac{1}{2} \varepsilon_{33}^S E_3^2 \right) d\bar{x} + A \int_{h_{ef}+h_p+h_s}^{h_{ef}+2h_p+h_s} \left(\frac{1}{2} Y_p S_{33}^2 - Y_p d_{33} E_3 S_{33} - \frac{1}{2} \varepsilon_{33}^S E_3^2 \right) d\bar{x}$$

$$\int_{\bar{V}} U_s = \frac{1}{2} \int_{\bar{V}} Y_s S_{33}^2 d\bar{V} = \frac{1}{2} Y_s A \int_{h_{ef}+h_p}^{h_{ef}+h_p+h_s} S_{33}^2 d\bar{x} \tag{3.4}$$

$$\int_{\bar{V}} U_{ef} = \frac{1}{2} \int_{\bar{V}} k u^2 d\bar{V} = \frac{1}{2} kA \int_0^{h_{ef}} u^2 d\bar{x}$$

where the spatial derivative is defined as $u' = \partial u / \partial x = S_{33}$. We can simplify the elastic foundation potential energy by assuming a constant epoxy thickness of known value and treating the layer as a linear spring, eliminating the integral for its corresponding potential energy and simplifying its influence to that of a boundary condition only, to be applied later. The spring constant is defined as $k = Y_{ef} A / h_{ef}$. Due to the strong influence of the adhesive layer on the systems stiffness, an experiment is conducted for estimation of the thickness of the bonding structure (Appendix B). The estimated thickness is used to calculate the layers spring constant, and the resulting modal frequencies dependent on this layer are compared to experimental results to ensure accuracy.

The kinetic energy is defined as [49]

$$\int_{\bar{V}} K d\bar{V} = \frac{1}{2} \int_{h_{ef}}^{h_{ef}+h_p} m_p \dot{u}^2 d\bar{x} + \frac{1}{2} \int_{h_{ef}+h_p}^{h_{ef}+h_p+h_s} m_s \dot{u}^2 d\bar{x} + \frac{1}{2} \int_{h_{ef}+h_p+h_s}^{h_{ef}+2h_p+h_s} m_p \dot{u}^2 d\bar{x} \tag{3.5}$$

where the time derivative is represented as $\dot{u} = du / dt$.

Hamilton's principle requires the application of variational methods to the energies previously described. Applying this method to the kinetic energy results in the expression

$$\delta\int_{\bar{V}} K d\bar{V} = -\int_{h_{ef}}^{h_{ef}+h_p} m_p \ddot{u}\delta u d\bar{x} - \int_{h_{ef}+h_p}^{h_{ef}+h_p+h_s} m_s \ddot{u}\delta u d\bar{x} - \int_{h_{ef}+h_p+h_s}^{h_{ef}+2h_p+h_s} m_p \ddot{u}\delta u d\bar{x} \ . \tag{3.6}$$

The IEEE standard constitutive relations of linear piezoelectricity are derived from the application of variational methods to the electric enthalpy, given in stress-electric displacement form as [49, 52]

$$\delta H = \frac{\partial H}{\partial S_{33}}\delta S_{33} + \frac{\partial H}{\partial E_3}\delta E_3 \ , \tag{3.7}$$

$$T_{33} = \frac{\partial H}{\partial S_{33}} = Y_p\left(S_{33} - d_{33}E_3\right) \ , \tag{3.8}$$

$$D_3 = -\frac{\partial H}{\partial E_3} = Y_p d_{33} S_{33} + \varepsilon_{33}^S E_3 \ . \tag{3.9}$$

The electric field is defined as $E_3 = -V_H(x,t)/L$ where the voltage is expressed as $V_H(x,t) = V(t)\left[\bar{H}(x-L) - \bar{H}(x)\right]$ with $V(t) = Ve^{j\omega t}$. Accordingly, $\delta S_{33} = \delta u'$ and $\delta E_3 = -\delta V_H / L$ therefore the total electric enthalpy is

$$\delta\int_{\bar{V}} H d\bar{V} = A\int_{h_{ef}}^{h_{ef}+h_p}\left(T_{33}\delta S_{33} - D_3\delta E_3\right)d\bar{x} + A\int_{h_{ef}+h_p+h_s}^{h_{ef}+2h_p+h_s}\left(T_{33}\delta S_{33} - D_3\delta E_3\right)d\bar{x} \ . \tag{3.10}$$

After expanding equation (3.10) and using integration by parts to simplify the expression, we find the variation of the electric enthalpy to be [51]

$$\begin{aligned}
\delta\int_{\bar{V}} H d\bar{V} = {} & Y_p A u'\delta u\Big|_{x=h_{ef}}^{x=h_{ef}+h_p} + Y_p A d_{33}\frac{V_H}{L}\delta u\Big|_{x=h_{ef}}^{x=h_{ef}+h_p} + Y_p A u'\delta u\Big|_{x=h_{ef}+h_p+h_s}^{x=h_{ef}+2h_p+h_s} + \\
& Y_p A d_{33}\frac{V_H}{L}\delta u\Big|_{x=h_{ef}+h_p+h_s}^{x=h_{ef}+2h_p+h_s} + Y_p A\int_{h_{ef}}^{h_{ef}+h_p}\left(-u'' - d_{33}\frac{V_H'}{L}\right)\delta u d\bar{x} + A\int_{h_{ef}}^{h_{ef}+h_p}\left(Y_p d_{33}u'\frac{1}{L} - \varepsilon_{33}^S\frac{V_H}{L^2}\right)\delta V_H d\bar{x} + \\
& Y_p A\int_{h_{ef}+h_p+h_s}^{h_{ef}+2h_p+h_s}\left(-u'' - d_{33}\frac{V_H'}{L}\right)\delta u d\bar{x} + A\int_{h_{ef}+h_p+h_s}^{h_{ef}+2h_p+h_s}\left(Y_p d_{33}u'\frac{1}{L} - \varepsilon_{33}^S\frac{V_H}{L^2}\right)\delta V_H d\bar{x}
\end{aligned} \tag{3.11}$$

The same process is applied to the substrate and elastic foundation, and the result substituted along with equations (3.6) and (3.11), into equation (3.2). The resulting expression contains the equations of motion, boundary conditions, and circuit equations which govern the bimorphs dynamics.

Having taken the elastic foundation to be a constant thickness, and applying its influence as a boundary condition, we can simplify the bounds of integration by defining the thickness coordinate to begin at $x = h_{ef} \equiv 0$. Accordingly, the bimorph is divided into three segments with axial deformations u_1, u_2, and u_3 for the regions $0 \le x \le h_p$, $h_p < x \le h_p + h_s$, and $h_p + h_s < x \le 2h_p + h_s$ [56]. Therefore, each material layer will have a corresponding equation of motion and the material interfaces will have boundary and continuity conditions to ensure contact is maintained. The three equations of motions are found to be

$$-m_p \ddot{u}_1 + Y_p A u_1'' + Y_p A d_{33} \frac{V_H'}{L} = 0, \qquad 0 \le x \le h_p \tag{3.12}$$

$$-m_s \ddot{u}_2 + Y_s A u_2'' = 0, \qquad h_p < x \le h_p + h_s \tag{3.13}$$

$$-m_p \ddot{u}_3 + Y_p A u_3'' + Y_p A d_{33} \frac{V_H'}{L} = 0, \qquad h_p + h_s < x \le 2h_p + h_s \tag{3.14}$$

and are bound by the four boundary conditions and two continuity conditions; with the first condition including stress continuity with the elastic layer modeled as a spring, given as

$$\left[Y_p A u_1' + Y_p A d_{33} \frac{V_H}{L} - k u_1 \right]_{x=0} = 0 \ , \tag{3.15}$$

$$\left[Y_s A u_2' - Y_p A u_1' - Y_p A d_{33} \frac{V_H}{L} \right]_{x=h_p} = 0 \ , \tag{3.16}$$

$$\left[-Y_s A u_2' + Y_p A u_3' + Y_p A d_{33} \frac{V_H}{L} \right]_{x=h_p+h_s} = 0 \ , \tag{3.17}$$

$$\left[-Y_p A u_3' - Y_p A d_{33} \frac{V_H}{L} \right]_{x=2h_p+h_s} = 0 \ , \tag{3.18}$$

$$\left[u_1 = u_2 \right]_{x=h_p} \ , \tag{3.19}$$

$$\left[u_2 = u_3 \right]_{x=h_p+h_s} \ . \tag{3.20}$$

To model the mechanical response of the bimorph we use separation of variables and can ignore terms coupled to the electrodynamics of the structure. The displacement is expressed using separation of variables, as

$$u_i(x,t) = \sum_{n=1}^{\infty} \phi_{ni}(x) \eta_{ni}(t) \tag{3.21}$$

where the subscripted index *i* represents one of the three material layers; explicitly the piezoelectric layers are represented by $i = 1 \text{ and } 3$, and for the steel substrate $i = 2$. The index *n* denotes the infinitely many modes, and the summation of this index will be implicit in the following derivation. The temporal function is defined as $\eta_n(t) = A_n e^{j\omega t}$, and $\ddot{\eta}_n(t) = -\omega_n^2 \eta_n(t)$. Applying these expressions to the uncoupled mechanical equations of motion, we find they are of the form

$$m_i \omega_n^2 \phi_{ni}(x) + Y_i A \phi_{ni}''(x) = \alpha_{ni} \phi_{ni}(x) + \phi_{ni}''(x) = 0 \ , \tag{3.22}$$

which has the general solution

$$\phi_{ni}(x) = a_{ni} \sin(\alpha_{ni} x) + b_{ni} \cos(\alpha_{ni} x) \tag{3.23}$$

where

$$\alpha_{ni} = \omega_n \sqrt{\frac{m_i}{Y_i A}} \ . \tag{3.24}$$

The general solution given by equation (3.23) is applied to the boundary and continuity conditions given by equations (3.15-3.20), resulting in a six-by-six coefficient matrix used to find

the eigenvalues of the system. Solving for the six unknown shape function coefficients is done using Galerkin's method.

Consider two distinct modes, *n* and *q*; multiplying equation (3.22) by $\phi_{qi}(x)$ and integrating over an arbitrary length, we find

$$-\int_{x_1}^{x_2} \phi_{qi}(x) Y_i A \phi''_{ni}(x) dx = \omega_{ni}^2 \int_{x_1}^{x_2} \phi_{qi}(x) m_i \phi_{ni}(x) dx \ . \tag{3.25}$$

Integration by parts of the left-hand side results in

$$-\left[\phi_{qi}(x) Y_i A \phi'_{ni}(x)\right]_{x_1}^{x_2} + \int_{x_1}^{x_2} \phi'_{qi}(x) Y_i A \phi'_{ni}(x) dx = \omega_{ni}^2 \int_{x_1}^{x_2} \phi_{qi}(x) m_i \phi_{ni}(x) dx \ . \tag{3.26}$$

Applying this expression to each material layer and its respective boundary conditions, and then summing the three resulting equations, we find

$$\begin{aligned} &\phi_{q1}(0) k \phi_{n1}(0) + \int_0^{h_p} \phi'_{q1}(x) Y_p A \phi'_{n1}(x) dx + \int_{h_p}^{h_p+h_s} \phi'_{q2}(x) Y_s A \phi'_{n2}(x) dx + \int_{h_p+h_s}^{2h_p+h_s} \phi'_{q3}(x) Y_p A \phi'_{n3}(x) dx = \\ &\omega_{n1}^2 \int_0^{h_p} \phi_{q1}(x) m_p \phi_{n1}(x) dx + \omega_{n2}^2 \int_{h_p}^{h_p+h_s} \phi_{q2}(x) m_s \phi_{n2}(x) dx + \omega_{n3}^2 \int_{h_p+h_s}^{2h_p+h_s} \phi_{q3}(x) m_p \phi_{n3}(x) dx \end{aligned} \ . \tag{3.27}$$

The continuity conditions of the bimorph require the natural frequencies of the layers to be equal to the systems natural frequency, therefore equation (3.27), can be simplified to

$$\phi_{q1}(0) k \phi_{n1}(0) + \sum_{i=1}^{3} \int_{x_1}^{x_2} \phi'_{qi}(x) Y_i A \phi'_{ni}(x) dx = \omega_n^2 \sum_{i=1}^{3} \int_{x_1}^{x_2} \phi_{qi}(x) m_i \phi_{ni}(x) dx \ . \tag{3.28}$$

By symmetry, the same equation holds for the natural frequencies denoted by mode *q*, giving

$$\phi_{q1}(0) k \phi_{n1}(0) + \sum_{i=1}^{3} \int_{x_1}^{x_2} \phi'_{qi}(x) Y_i A \phi'_{ni}(x) dx = \omega_q^2 \sum_{i=1}^{3} \int_{x_1}^{x_2} \phi_{qi}(x) m_i \phi_{ni}(x) dx . \tag{3.29}$$

Subtracting equation (3.29) from equation (3.28), we find

$$\left(\omega_n^2 - \omega_q^2\right)\sum_{i=1}^{3}\int_{x_1}^{x_2}\phi_{qi}(x)m_i\phi_{ni}(x)dx = 0 \ . \tag{3.30}$$

Therefore,

$$\sum_{i=1}^{3}\int_{x_1}^{x_2}\phi_{qi}(x)m_i\phi_{ni}(x)dx\Big|_{n\neq q} = 0 \tag{3.31}$$

and the mass normalization is defined as

$$\sum_{i=1}^{3}\int_{x_1}^{x_2}\phi_{qi}(x)m_i\phi_{ni}(x)dx = \delta_{nq} \ . \tag{3.32}$$

Subsequently using this result and equation (3.28), we find

$$\phi_{q1}(0)k\phi_{n1}(0) + \sum_{i=1}^{3}\int_{x_1}^{x_2}\phi'_{qi}(x)Y_iA\phi'_{ni}(x)dx = \omega_n^2\delta_{nq} \ . \tag{3.33}$$

For non-trivial solutions, $n = q$, equation (3.32) can be expanded to

$$\int_0^{h_p} m_p\phi_{n1}(x)^2dx + \int_{h_p}^{h_p+h_s} m_s\phi_{n2}(x)^2dx + \int_{h_p+h_s}^{2h_p+h_s} m_p\phi_{n3}(x)^2dx = 1 \ . \tag{3.34}$$

We may also represent the shape functions as an equivalent function normalized by a modal coefficient, written as [51]

$$\phi_{ni}(x) = a_2\left(\frac{a_i}{a_2}\sin(\alpha_{ni}x) + \frac{b_i}{a_2}\cos(\alpha_{ni}x)\right) = a_2\tilde{\phi}_{ni}(x) \tag{3.35}$$

Substituting equation (3.35) into equation (3.34), and after factoring for a_2, we find

$$a_2 = \frac{1}{\sqrt{\int_0^{h_p} m_p\tilde{\phi}_{n1}(x)^2dx + \int_{h_p}^{h_p+h_s} m_s\tilde{\phi}_{n2}(x)^2dx + \int_{h_p+h_s}^{2h_p+h_s} m_p\tilde{\phi}_{n3}(x)^2dx}} \ . \tag{3.36}$$

Using the coefficient matrix found earlier along with equation (3.36), we have found the systems shape functions and eigenvalues, representing the mechanical response of the system.

The temporal modes are found using Galerkin's discretization method. The electro-mechanically coupled equations of motion given by equations (3.12-3.14) are multiplied by an orthogonal shape function, $\phi_{ki}(x)$, and the resulting expression integrated over its respective material layer's thickness. For the three bimorph layers, these equations are

$$\int_0^{h_p} \phi_{k1}\left(m_p \phi_{n1} \ddot{\eta}_{n1} - Y_p A \phi''_{n1} \eta_{n1} - Y_p A d_{33} \frac{V'_H}{L} \right) dx = 0 \ , \tag{3.37}$$

$$\int_{h_p}^{h_p+h_s} \phi_{k2}\left(m_s \phi_{n2} \ddot{\eta}_{n2} - Y_s A \phi''_{n2} \eta_{n2} \right) dx = 0 \ , \tag{3.38}$$

$$\int_{h_p+h_s}^{2h_p+h_s} \phi_{k3}\left(m_p \phi_{n3} \ddot{\eta}_{n3} - Y_p A \phi''_{n3} \eta_{n3} - Y_p A d_{33} \frac{V'_H}{L} \right) dx = 0 \ . \tag{3.39}$$

Equations (3.37-3.39) are evaluated with their respective boundary and continuity conditions, as well as the orthogonality condition is given by equation (3.33). Furthermore, we make the common approximation that the electric field is constant over the length of the bimorph, negating the influence of position. Accordingly, summing the three evaluated expressions results in the relationship

$$\ddot{\eta}_n + \eta_n \omega_n^2 + Y_p A d_{33} \frac{V(t)}{L} \left[\int_0^{h_p} \phi'_{k1} dx + \int_{h_p+h_s}^{2h_p+h_s} \phi'_{k3} dx \right] = 0 \ . \tag{3.40}$$

Evaluating the integrals, we find

$$\ddot{\eta}_n + \eta_n \omega_n^2 + Y_p A d_{33} \frac{V(t)}{L} \left(\left[\phi_{n1}(h_p) - \phi_{n1}(0) \right] + \left[\phi_{n3}(2h_p + h_s) - \phi_{n3}(h_p + h_s) \right] \right) = 0 \ . \tag{3.41}$$

Replacing the temporal function variable with its definition, we are able to simplify equation (3.41) and solve for the amplitude constant of the temporal function as

$$A_n = \frac{Y_p A d_{33} \frac{V}{L}\left[\phi_{n1}(0) + \phi_{n3}(h_p + h_s) - \phi_{n1}(h_p) - \phi_{n3}(2h_p + h_s)\right]}{\omega_n^2 - \omega^2} \quad . \tag{3.42}$$

Therefore, the temporal function is the final expression

$$\eta(t) = \frac{Y_p A d_{33} \frac{V}{L}\left[\phi_{n1}(0) + \phi_{n3}(h_p + h_s) - \phi_{n1}(h_p) - \phi_{n3}(2h_p + h_s)\right]}{\omega_n^2 - \omega^2} e^{j\omega t} \quad . \tag{3.43}$$

Substituting this expression back into the original definition for the displacement using separation of variables, as well as adding in the effects of viscous damping, we find the displacement of the bimorph to be

$$u_i(x,t) = \sum_{n=1}^{\infty} \frac{\phi_{ni}(x) Y_p A d_{33} \frac{V}{L}\left[\phi_{n1}(0) + \phi_{n3}(h_p + h_s) - \phi_{n1}(h_p) - \phi_{n3}(2h_p + h_s)\right]}{(\omega_n^2 - \omega^2) + 2j\zeta\omega_n\omega} e^{j\omega t} \quad . \tag{3.44}$$

A previous investigation, Dupuis *et al.* 2017, had modeled the vibration of the inner substrate not adhered to the annular PZT rings, resulting in an expression for the acceleration at any point on the plate as [30]

$$a(r,t) = -\omega^2 W_o e^{j\omega t}\left[1 + \sum_{n=1}^{\infty} \psi_n(r) \frac{2\pi\rho_s h_s \omega^2 \int_0^{r_i} r\psi_n(r)dr}{\Omega_n^2 - \omega^2 + 2j\zeta_n\Omega_n\omega}\right] \tag{3.45}$$

where W_o, the magnitude of base excitation, at the time was found from experimental measurements. Having modeled the bimorph portion responsible for the input base excitation to the plate, the entirety of the transducer has been modeled for axisymmetric boundary conditions, where the input base excitation is

$$u_2(\tfrac{L}{2}, t) = W_o e^{j\omega t} \quad . \tag{3.46}$$

These resulting equations allow us to use known material properties, dimensions, and electrical stimulus to predict the deformation of the entire transducer; most importantly, the resulting acceleration of the steel substrate which makes contact with wet clothing during the drying process.

3.3. Experiments and model validation

This investigation was intended to complete the electroelastic modeling of a semi-annular piezoelectric bimorph, therefore special attention was placed on verifying that the model accurately predicts the bimorphs dynamics. To ensure the separation of the model into two parts is accurate, the transducer's central plate is removed by subtractive manufacturing at a slow rate to ensure the heat generated from friction does not damage the PZT's. Therefore, the bimorph model can be compared experimentally to an equivalent geometry. An equivalent geometry is also created in COMSOL Multiphysics, where a comparison of bimorph mode shape results between the analytical and FEM model can be viewed in Appendix C.

Verification of the proposed models was done by measuring the dynamic response of the transducer at several locations which characterize the device and have been identified to be most influential for the process of ultrasonic atomization. These influential parameters are: (1) the displacement of the bimorph at the operating frequency of the transducer when atomization is occurring, (2) the displacement of the bimorph at its resonance frequency, and (3) the output acceleration at the center of the transducer, being the input energy for the ultrasonic atomization process.

The experiment is pictured in figure 3.2a, showing a single-point laser doppler vibrometer (LDV; Polytec OFV 5000/505) aimed at reflective tape placed at several points on the bimorph (figure 3.2b), and the transducer (figure 3.2c). An AC signal is generated using a Keysight 33500B

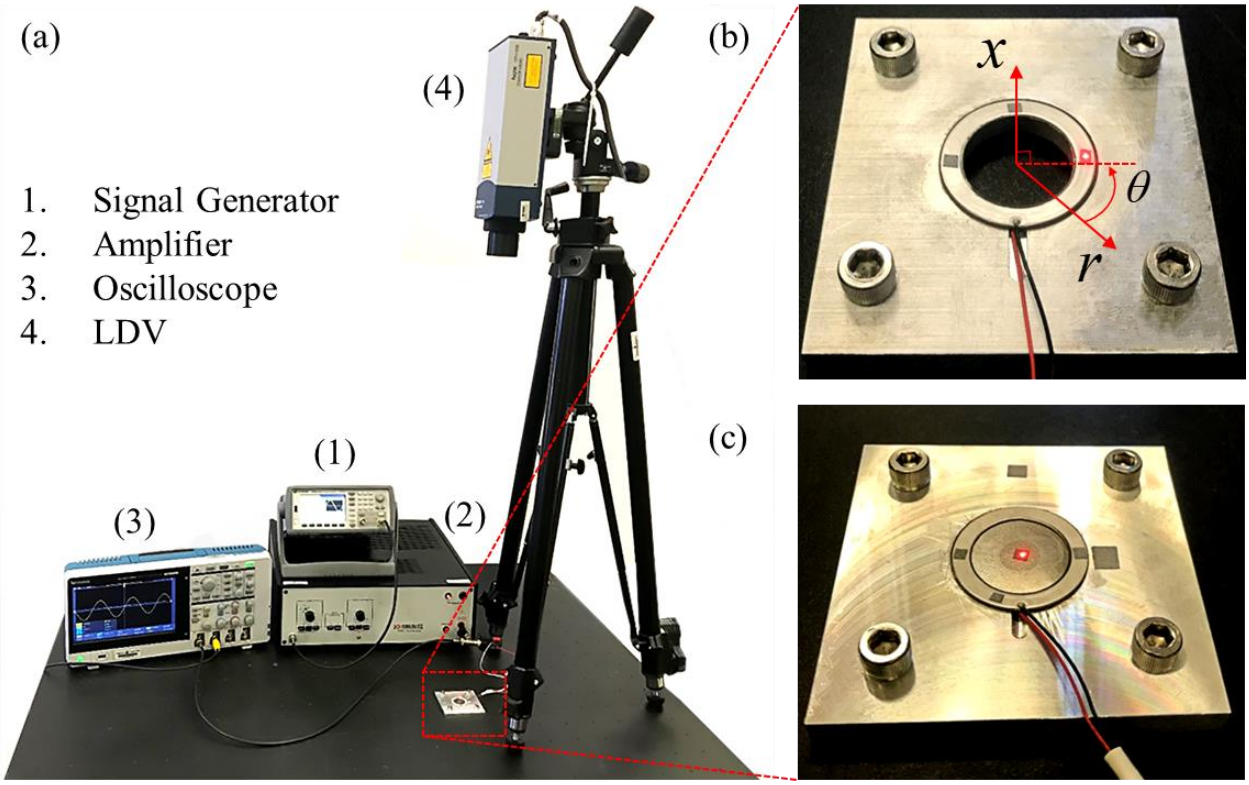

Figure 3.2. (a) Experiment set-up, **(b)** piezoelectric bimorph, and **(c)** whole piezoelectric transducer.

Waveform Generator and then amplified using a Krohn-Hite model 7500 amplifier before actuating the transducer. The amplified actuation signal, as well as the output voltage of the LDV, is measured with an oscilloscope (Tektronix TBS 2000) operated by a MATLAB® script for the recording of data.

Validation of the bimorph model was done in part by comparing the predicted first modal frequency with experimental measurements. It was found that epoxy layer thickness had a significant effect on the system's natural frequency (Section 3.4). The thickness of this layer adhering the bimorph to the fixture, needed for calculation of the boundary conditions spring constant, is approximated by matching the model's predicted first mode with that found by experiment. In the limit of the thickness approaching zero, the linear spring boundary conditions approach that of a rigid wall, resulting in a first modal frequency of 995 kHz. After approximating

the epoxy thickness as 1.5 μm, the analytical model's first mode was found to match experimental measurements at a frequency of 930 kHz (figure 3.3a).

Further validation of the analytical model was done by measuring the bimorphs displacement at the operating frequency of the transducer, ~100 kHz, where atomization occurs. This displacement is compared to that predicted by equation (3.44) for $u_3(2h_p + h_s, t)$, figure 3.3b. It can be seen both the resonance and off-resonance response of the bimorph is accurately predicted by the proposed analytical model. Furthermore, the small deviations from experiment and model have a negligible effect on the resulting plate acceleration and its influence on ultrasonic drying. While variations in epoxy thickness around the boundary, as well as manufacturing imperfections within the transducer, cause experimental data to have small deviations between each run, the results were highly repeadtable, although no stastical method was used due to the sensitivity of the trials.

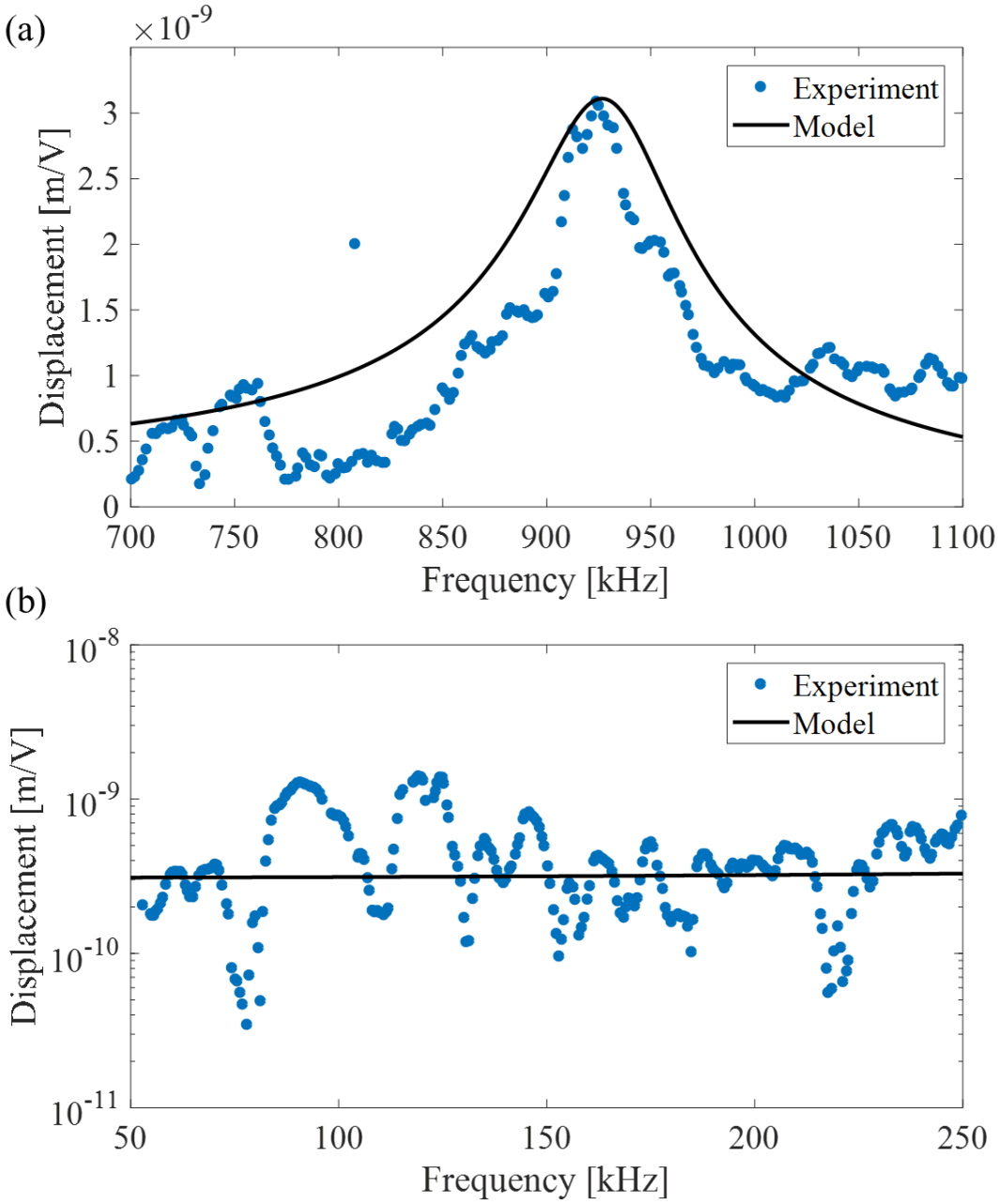

Figure 3.3. Bimorph displacement per input voltage, experiment and theory at **(a)** resonance, and **(b)** off-resonance.

The bimorph displacement is modeled as the base excitation to the unconstrained substrate with a thin plate geometry. A comparison was made between the predicted frequency response function (FRF) of the modeled central plate with that of the experiment in the range where atomization occurs. Two separate but equivalent transducers were adhered to two fixtures using a vacuum bonding process [48]. From the FRF's of the two structures, the peak amplitude of each

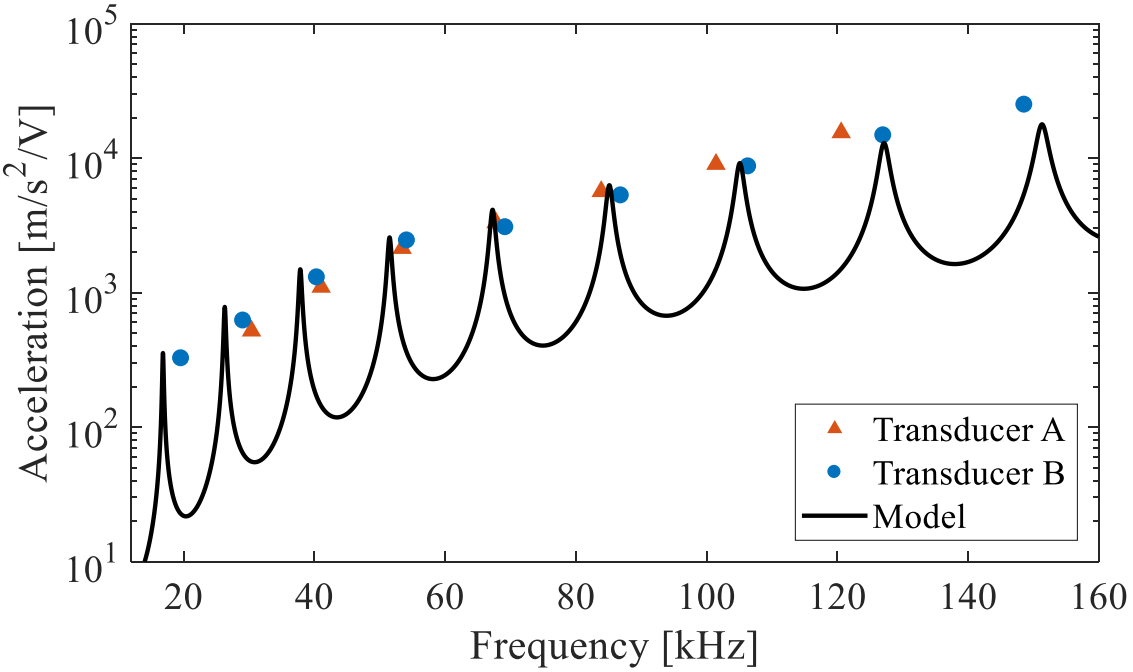

Figure 3.4. Acceleration of the plate's geometric center due to bimorph displacement; experiment and theory.

harmonic within the plotted range is compared against the resulting analytical expression (figure 3.4), where the input base displacement to equation (3.45) is taken from the predicted bimorph displacement function, equation (3.44), having been plotted in figure 3.3.

It can be seen that the analytical expression for the plate, with the input from the analytical bimorph model, accurately predicts the response of the transducers measured experimentally. Moreover, the magnitudes measured are comparable with those needed to achieve atomization, given by equation (3.1) [25]; the presence of atomization during testing further confirms the accuracy of the measured values. Variations in the frequency and amplitude of corresponding mode numbers are in the range of variations from one transducer to another, suggesting that the system is sensitive to minor differences in material properties from the manufacturing process, as well as variations in the adhering epoxy layer, both being factors where accurate modeling is difficult.

Furthermore, it is evident that a resonance mismatch occurs between the bimorphs first modal frequency (~1 MHz) and the operating frequency of the transducer (~100 kHz). This significant resonance mismatch inhibits the system from operating at peak efficiency. An investigation was performed to resolve this issue and is described in the following section.

3.4. Influence of adhering layer on direct contact ultrasonic drying

Efficient drying relies heavily on optimizing the boundary conditions of the transducers in order to achieve high accelerations and rapid atomization; therefore a similar analysis was performed for the electroelastic equations developed in this study [30]. The epoxy used to adhere the transducer to the fixture was found to have a significant impact on the modal frequencies of the bimorph, as this is the connecting layer modeled as a spring foundation supporting the transducer, having stiffness k in equation (3.4), and contributing to the system's potential energy. Variations in thickness of this layer and its effect on the bimorphs displacement (equation 3.44) over a range of actuation frequencies are plotted in figure 3.5. The increasing thickness' plotted results in a decrease in stiffness of the epoxy layer, as $k = Y_{ef} A / h_{ef}$, causing the systems natural frequency to lower proportionally with the decrease in spring constant magnitude.

It was found that mounting the transducer on an epoxy layer 760 μm thick lowers the bimorphs naturally frequency to that of the operating frequency of the transducer (~100 kHz). Lowering the natural frequency allows for resonance matching, which vastly increases the atomization capabilities of the transducer. This shift in resonance provides a tenfold increase in base excitation displacement, without any changes made to the transducer itself. The resulting increase in base excitation amplitude to the plate provides a tenfold increase in acceleration (equation 3.45), shown

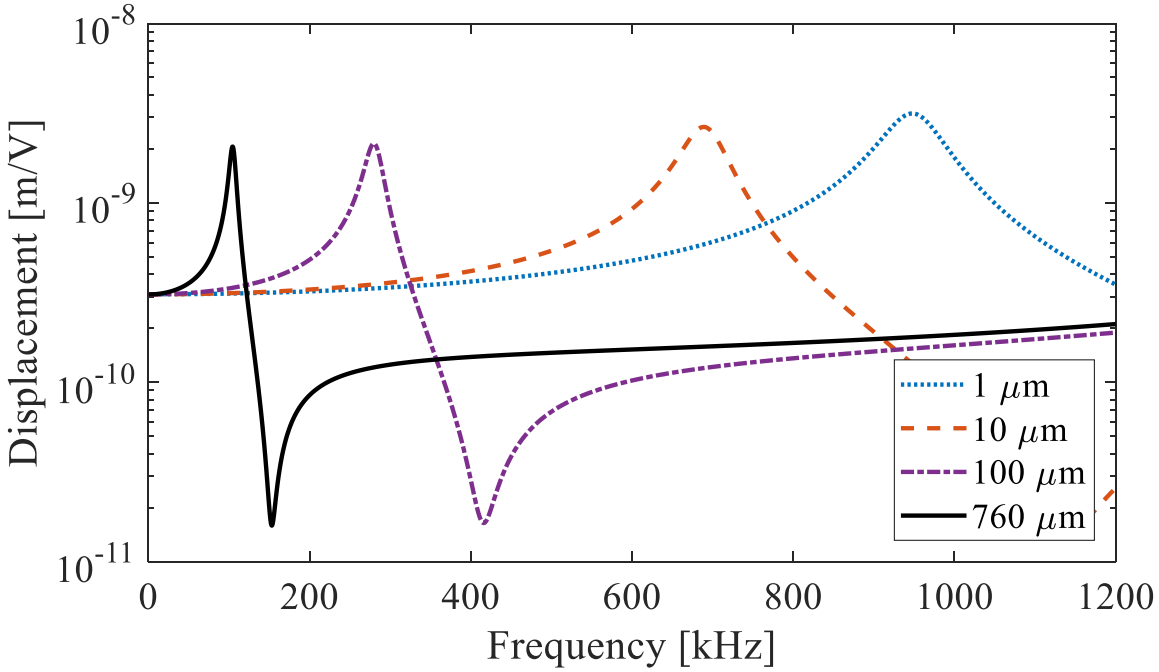

Figure 3.5. Theoretical bimorph displacement by electrical actuation for various thicknesses of epoxy.

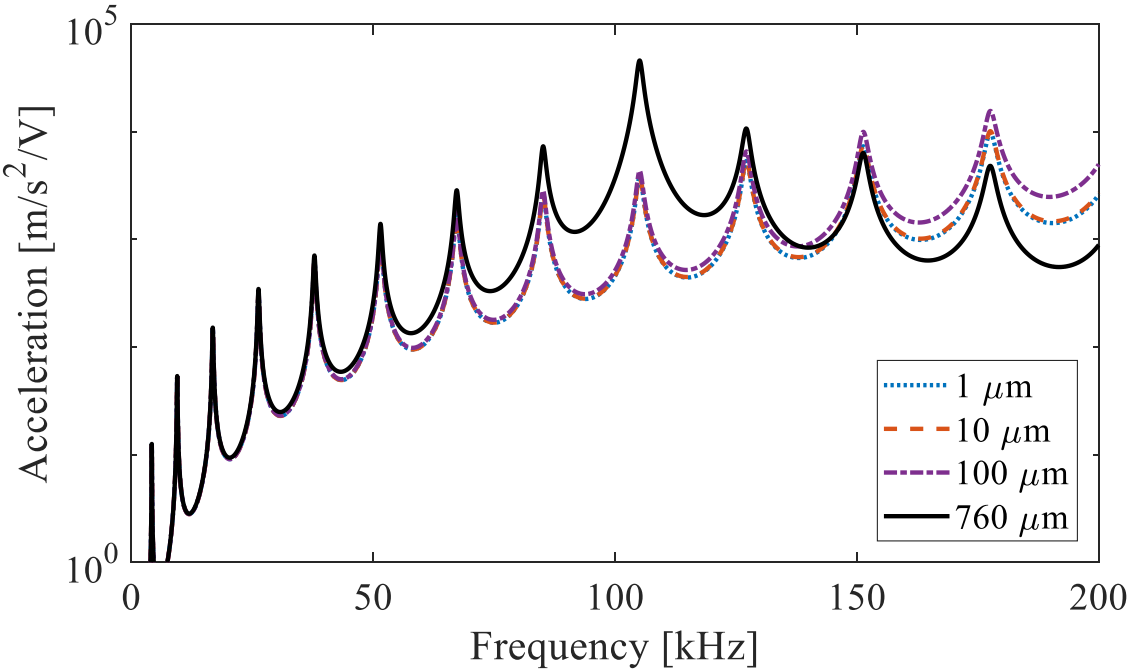

Figure 3.6. FRF for acceleration at the center of the plate due to actuation by the bimorph displacement given by figure 3.5 in the same frequency range.

by figure 3.6, where the 760 μm thick layers FRF has a significant increase in acceleration over a narrow bandwidth around the operating frequency of ~100 kHz.

Direct contact ultrasonic drying has been shown to be heavily dependent on the average acceleration over the contact area between the fabric and vibrating structure. The magnitude of applied acceleration directly governs the quantity of water in the fabric, which can be atomized in the initial nonlinear region, as well as the rate at which this water is atomized [30]. Previous investigations by the authors of Dupuis *et al.* [30], revealed a single non-dimensional expression for the nonlinear portion of direct contact ultrasonic drying as

$$\bar{M}(t) = (1 + \bar{C}_1 + C_2\bar{a}) + (\bar{M}_{sat} - \bar{C}_1 - C_2\bar{a}) \exp\left\{-\bar{\Omega}_1 \, \mathrm{e}^{(1.58\times10^{-5}\,\bar{a})}\, t \,/\left[(\mathrm{A}_f) t_1 e^{(-5\times10^{-6}\,\bar{a})} \right]\right\} \quad (3.47)$$

where $\bar{a}$ is the average acceleration over the plate, calculated with the area integral

$$\bar{a} = \frac{\int_0^{r_i} 2\pi r \left| a(r,t) \right| dr}{\pi r_i^2} \; . \quad (3.48)$$

The resulting increase in output acceleration due to the resonance matching of the bimorph and plate has a significant effect on the drying time of fabrics. For each of the epoxy layers investigated, a corresponding drying curve found using equation (3.47) was plotted due to the changing average acceleration associated with each case, shown by figure 3.7.

Optimizing the epoxy layer thickness for resonance matching has the potential to decrease drying times by over 50%. Preliminary results for the energy consumption of this technology are approximately 0.3 kJ/g, being 10 times more efficient than current electric resistance dryers. The application of our study would have the potential halve the consumption, significantly increasing the current efficiency of ultrasonic drying to 20 times that of electric resistant dryers.

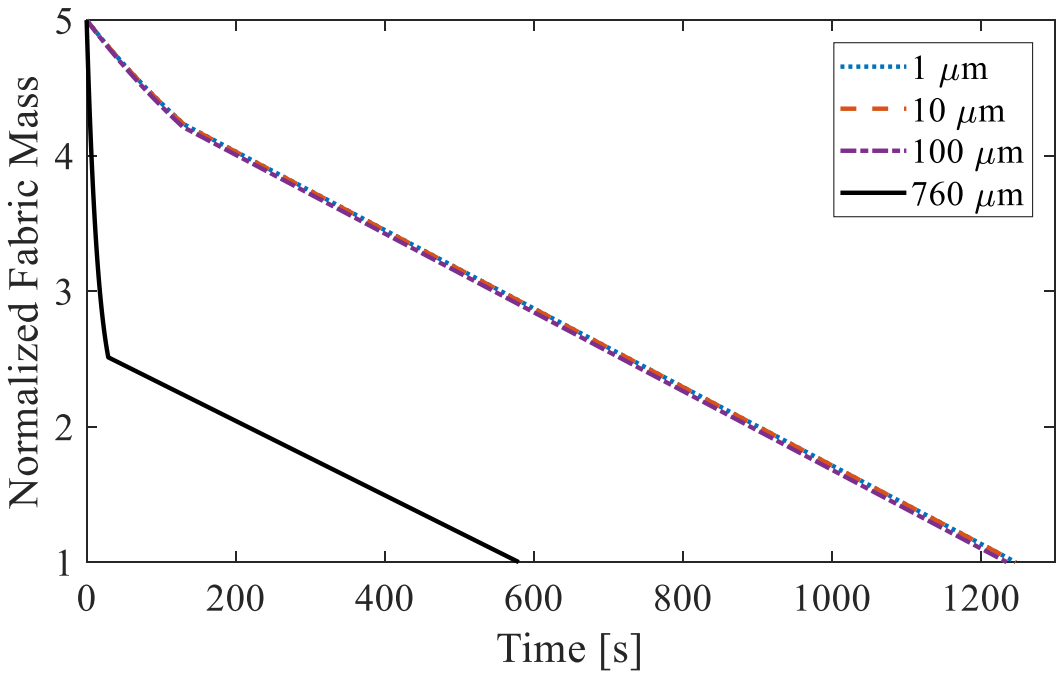

Figure 3.7. Influence of epoxy layer thickness on direct-contact ultrasonic drying times.

Conclusions

Direct contact ultrasonic clothes drying using principles of atomization shows great potential over conventional thermal drying techniques. While heat-pump dryers and even improved heating coils have recently increased thermal drying efficiency, the high latent heat of vaporization of water limits significant improvements. Furthermore, increases in thermal drying efficiency typically come at the expense of longer dry times, which is a crucial metric for market acceptability. The mechanical nature of droplet ejection due to atomization and its relation to fabric drying is an ideal replacement for conventional electric resistance clothes dryers. The high accuracies distributed parameter electroelastic models have for predicting deformations based upon an input voltage, coupled with the acceleration dependent drying rate of fabrics in direct

contact with these ultrasonic vibrations, enables the design of a unique dryer catering to the mechanics of atomization in fabrics highlighted in this and other investigations by the authors.

The analytical model in this investigation represents the bimorph transducer in its entirety, from which the material properties and geometry can be adjusted to optimize energy-efficient drying. The electroelastic expression for an annular bimorph developed in this investigation, coupled with the plate deformation model previously developed by the authors [30], fully completes the model for a disc type piezoelectric transducer where thickness mode deformations are dominant. The output acceleration is then connected to the global expression for the drying rates of fabrics in direct contact with ultrasonic vibrations. From these three coupled expressions, optimization of the vibrating structure can be completed. A mismatch in resonant frequencies found between the bimorph and the portion of the plate in contact with fabric reduces the efficiency of the system significantly. In this investigation, we propose resonance matching by modification of the bonding epoxy layer, resulting in upwards of a 200% increase in efficiency.

This chapter provides a useful vibration-based model for annular-type bimorph transducers. The relationships between the particular transducer, its boundary conditions, and the influence of these parameters on ultrasonic drying are extremely useful for the optimization of the dryer design to ensure market acceptability and significant energy savings.

Appendix A: PZT material investigation

The commercially available transducer used in this investigation as well as early prototypes of the direct contact ultrasonic dryer utilizes a specific form of lead zirconate titanate, PZT-5A, as the default material for the annular piezoelectric rings. The electromechanical coupling coefficient, density, and Young's modulus are all parameters of the material which highly influence the

performance of the bimorph. It was found for PZT-5A there is a mismatch in the first modal frequency of the bimorph and the operating frequency of the transducer, as discussed in section 3.4; therefore it is hypothesized that through careful selection of the PZT material utilized, a closer match in resonance frequencies can be obtained. For this investigation, we will look at three commonly used piezoelectric materials, PZT-5A and PZT-5H being soft ceramics, and PZT-8, a hard ceramic, indicated by the mechanical quality factors (Table A1) [37].

Material	Density [kg/m^2]	Youngs Modulus [GPa]	Piezoelectric Constant [m/V]	Quality Factor
PZT-5A	7,800	56	450	100
PZT-5H	7,800	53	600	80
PZT-8	7,600	74	250	1200

Table 3.A1. Properties of three piezoelectric materials investigated.

Specifically, their influence on the analytical model manifests itself in the natural frequencies of the system, the amplitude of displacement, as well as the electromechanical coupling factor, given by equation 3.44 as

$$\theta = Y_p A d_{33} \frac{V}{L} \tag{3.A.1}$$

It can be seen from equation 3.A.1 the amplitude of displacement is linearly dependent on the thickness coupling coefficient d_{33}. This is identified to be the dominant parameter for the displacement of the bimorph.

For both the analytical and experimental results, PZT-5H performed better than the currently used PZT-5A, and both these materials resulted in a higher acceleration output than PZT-8 (figure 3.A1). This is due to the higher coupling in the thickness direction of PZT-5H, as well as the lower Young's Modulus, leading to a lower natural frequency of the bimorph which approaches that of the plate.

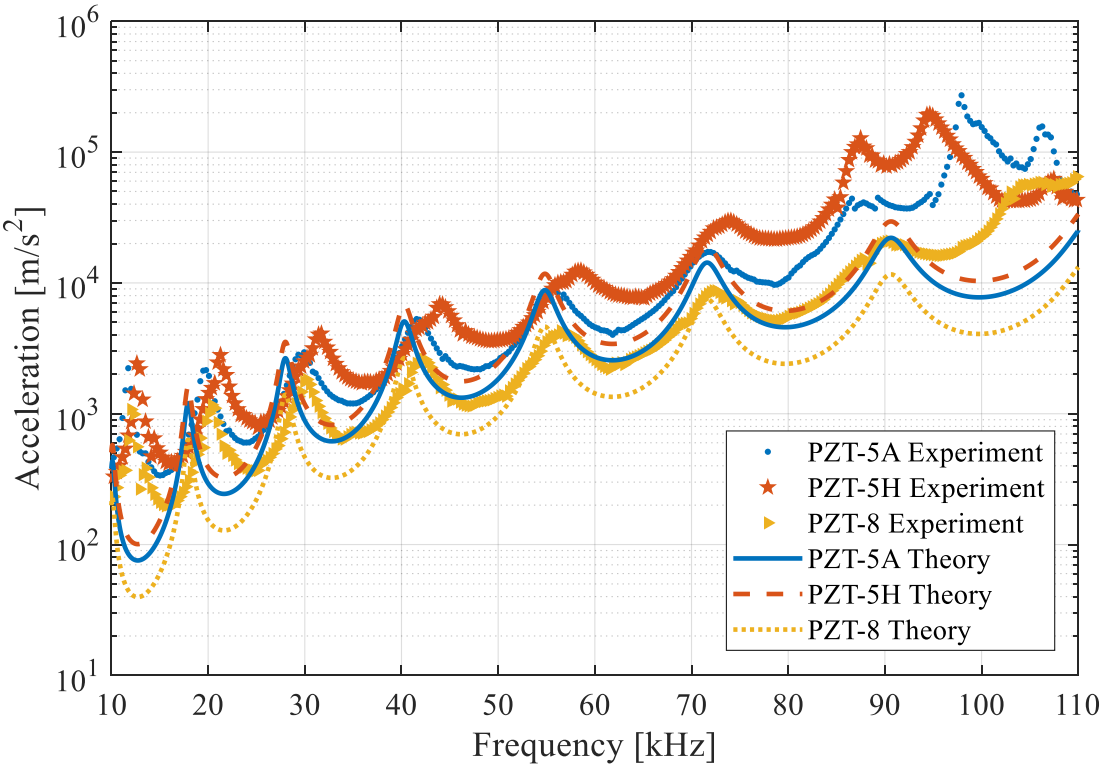

Figure 3.A1. Experimental and Theoretical FRFs for various piezoelectric materials used in the bimorph transducer.

From figure 3.A1, it can be seen that a simple change of the materials used can increase the output acceleration of the transducer by a factor of two over the currently used PZT-5A. This change results in no additional cost to manufacturing or to the geometry of the transducer. The lack of agreement due to nonlinear effects in the form of midplane stretching occurs as the operating frequency approaches ~100 kHz. This is further discussed in section 6.5.1.

Appendix B: Bonding layer thickness estimation

The adhesive layer attaching the piezoelectric transducer to a supporting plate has a strong influence on the systems natural frequency due to the high magnitudes of stiffness in the epoxy. As such, it is crucial to estimate the spring constant of this layer accurately to ensure the bimorph's natural frequency matches that of experiment. We have previously defined the spring constant of

this layer to be $k = Y_{ef} A / h_{ef}$, where the epoxy Young's modulus and contact area are constant for a given adhesive and transducer size, therefore, we must approximate the thickness of the epoxy layer to accurately account for the adhesive's influence on the system.

The experiment is conducted by testing various applied masses over aluminum disks connected to an aluminum plate by a thick layer of adhesive. The applied weight then compresses the disk and excess glue is expelled to the sides of the disk. The weights range from the lone weight of the disk, to an applied mass of 500g in six increments (figure 3.B1). The thickness is measured with digital calipers three times, and the average taken as the final measurement. The results are plotted in figure 3.B2, showing an exponential decrease in epoxy thickness when increasing the applied weight over the disk.

The transducer used in this thesis is vacuum bonded to a supporting plate to ensure uniformity of the adhering layer. This process allows for imperfections within the bonding layer to be removed, and a uniform height achieved. The vacuum applies a pressure of 25 in/Hg over the surface area of the transducer, being approximately 7 square centimeters. This relates to a force of approximately 5,500 grams, applied over the adhesive layer bonding the transducer to the aluminum plate. Through the use of figure 3.B2, we can assume the bonding layer to be only several micrometers thick. This is used as the initial approximation for the model, and will be tested by comparisons to experimental measurements of the first thickness mode of the bimorph.

Figure 3.B1. Epoxy thickness measurement experiment.

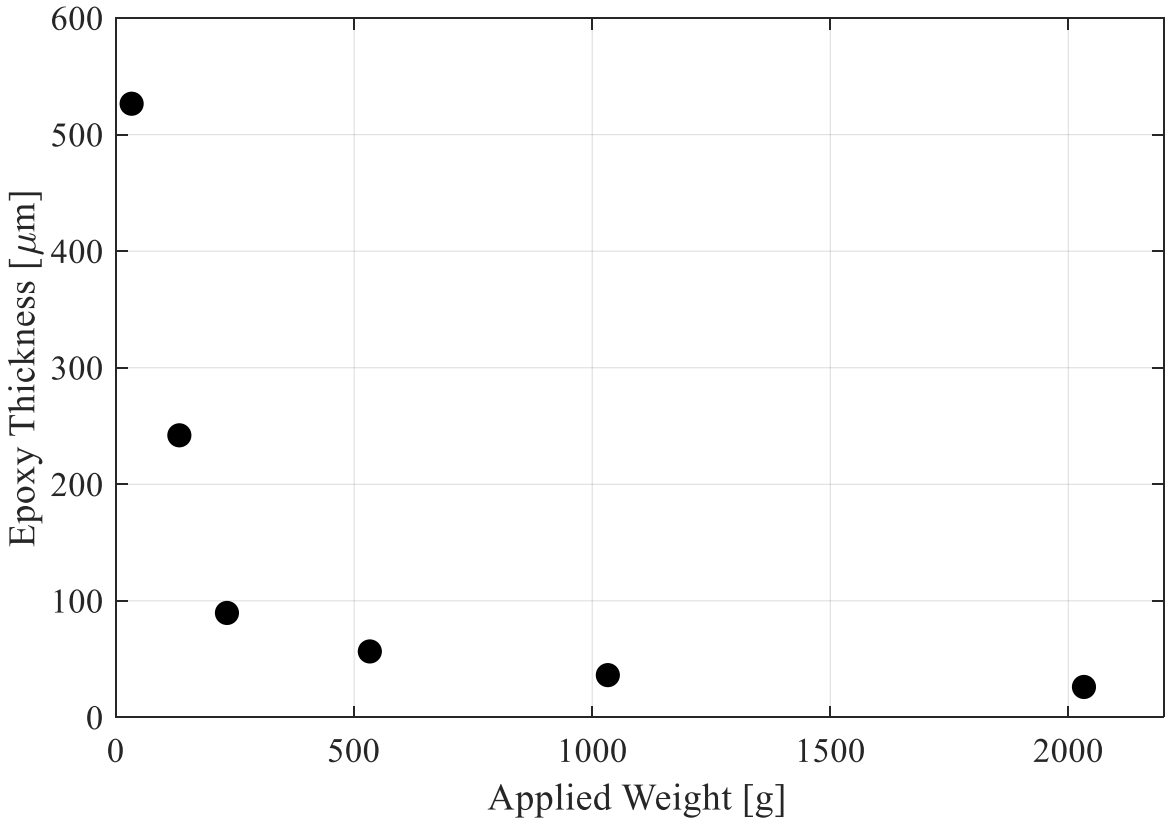

Figure 3.B2. Epoxy thickness versus the applied weight over the discs.

Appendix C: Mode shape verification

An early step in verifying the accuracy of analytical modeling is through comparisons of the mechanical response of the model to that of finite element modeling. Mode shapes, or the resonant displacement of a structure at various excitations equal to that of the systems natural frequency, is commonly used as this initial verification. For the bimorph subjected to an axisymmetric fixed boundary condition on its bottom surface, each layer will displace and compress in a specific manner for each resonant frequency. The fundamental modal frequency results in the expansion of each of the three bimorph layers. As we move upwards in mode number,

we gain additional compressive regions, increasing linearly in number for each increasing mode. A comparison of these mode shapes can be viewed in figure 3.C1.

It can easily be seen there is a one-to-one match between the analytically predicted mode shapes and that provided by COMSOL Multiphysics finite element modeling. Moreover, the inclusion of the epoxy boundary condition does not alter the agreement of the two models. This highlights the accuracy of the analytical model, where the natural frequencies and displacements are correctly predicted.

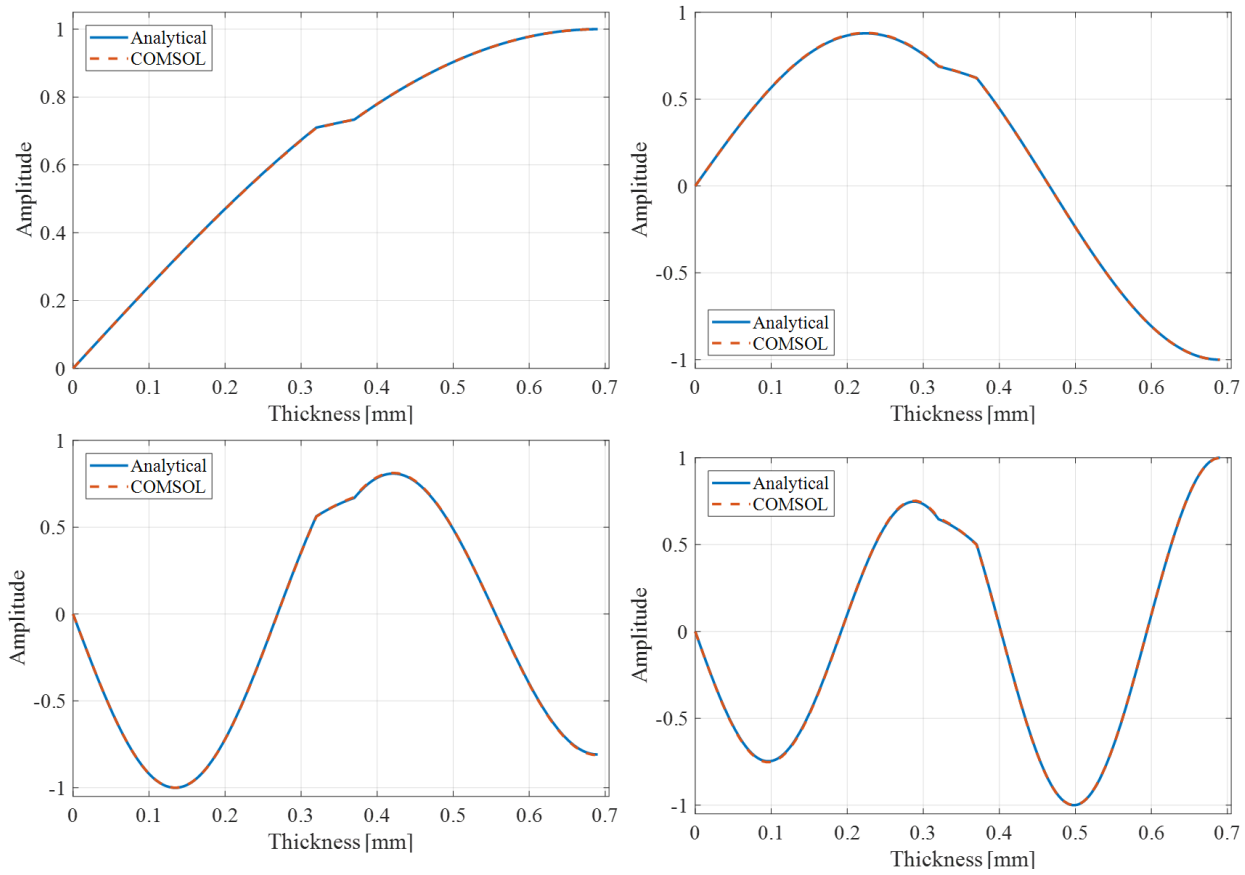

Figure 3.C1. Analytical and finite element mode shapes for the first four natural frequencies of the bimorph structure under an axisymmetric fixed boundary condition.

Bibliography

1. Beeby, S.P., M.J. Tudor, and N.M. White, *Energy harvesting vibration sources for microsystems applications.* Measurement Science and Technology, 2006. **17**(12): p. R175-R195.
2. Priya, S., *Advances in energy harvesting using low profile piezoelectric transducers.* Journal of Electroceramics, 2007. **19**(1): p. 167-184.
3. Priya, S. and D.J. Inman, *Energy Harvesting Technologies*. 2009, Springer.
4. Cook-Chennault, K.A., N. Thambi, and A.M. Sastry, *Powering MEMS portable devices—a review of non-regenerative and regenerative power supply systems with special emphasis on piezoelectric energy harvesting systems.* Smart Materials and Structures, 2008. **17**(4).
5. Wang, X., et al., *A frequency and bandwidth tunable piezoelectric vibration energy harvester using multiple nonlinear techniques.* Applied Energy, 2017. **190**: p. 368-375.
6. Administration, U.S.E.I. *Annual Energy Outlook*. 2019; Available from: https://www.eia.gov/outlooks/aeo/tables_ref.php.
7. Yadav, V. and C.G. Moon, *Fabric-drying process in domestic dryers.* Applied Energy, 2008. **85**(2-3): p. 143-158.
8. Patel, V.K., et al., *Experimental evaluation and thermodynamic system modeling of thermoelectric heat pump clothes dryer.* Applied Energy, 2018. **217**: p. 221-232.
9. Tuğrul Oğulata, R., *Utilization of waste-heat recovery in textile drying.* Applied Energy, 2004. **79**(1): p. 41-49.

10. Ng, A.B. and S. Deng, *A new termination control method for a clothes drying process in a clothes dryer.* Applied Energy, 2008. **85**(9): p. 818-829.

11. Bansal, P., K. Sharma, and S. Islam, *Thermal analysis of a new concept in a household clothes tumbler dryer.* Applied Energy, 2010. **87**(5): p. 1562-1571.

12. Stawreberg, L. and L. Nilsson, *Potential energy savings made by using a specific control strategy when tumble drying small loads.* Applied Energy, 2013. **102**: p. 484-491.

13. Denkenberger, D., et al., *Analysis of Potential Energy Savings from Heat Pump Clothes Dryers in North-America*. 2013, Ecova and Collaborative Labeling and Appliance Standards Program (CLASP).

14. James, A.J., et al., *Vibration-induced drop atomization and bursting.* Journal of Fluid Mechanics, 2003. **476**.

15. Barreras, F., H. Amaveda, and A. Lozano, *Transient high-frequency ultrasonic water atomization.* Experiments in Fluids, 2002. **33**(3): p. 405-413.

16. Goodridge, C.L., W.T. Shi, and D.P. Lathrop, *Threshold Dynamics of Singular Gravity-Capillary Waves.* Physical Review Letters, 1996. **77**(22): p. 4692-4692.

17. de la Fuente-Blanco, S., et al., *Food drying process by power ultrasound.* Ultrasonics, 2006. **44 Suppl 1**: p. e523-7.

18. Ramisetty, K.A., A.B. Pandit, and P.R. Gogate, *Investigations into ultrasound induced atomization.* Ultrason Sonochem, 2013. **20**(1): p. 254-64.

19. Yule, A.J. and Y. Al – Suleimani, *On droplet formation from capillary waves on a vibrating surface.* Proceedings of the Royal Society of London. Series A: Mathematical, Physical and Engineering Sciences, 2000. **456**(1997): p. 1069-1085.

20. Rajan, R. and A.B. Pandit, *Correlations to predict droplet size in ultrasonic atomisation.* Ultrasonics, 2001. **39**(4): p. 235-255.

21. Wood, R.W. and A.L. Loomis, *XXXVIII. The physical and biological effects of high-frequency sound-waves of great intensity.* The London, Edinburgh, and Dublin Philosophical Magazine and Journal of Science, 1927. **4**(22): p. 417-436.

22. Vukasinovic, B., M.K. Smith, and A. Glezer, *Spray characterization during vibration-induced drop atomization.* Physics of Fluids, 2004. **16**(2): p. 306-316.

23. Vukasinovic, B., M.K. Smith, and A. Glezer, *Mechanisms of free-surface breakup in vibration-induced liquid atomization.* Physics of Fluids, 2007. **19**(1).

24. Goodridge, C.L., et al., *Viscous effects in droplet-ejecting capillary waves.* Physical Review E, 1997. **56**(1): p. 472-475.

25. Lang, R.J., *Ultrasonic Atomization of Liquids.* The Journal of the Acoustical Society of America, 1962. **34**(1): p. 6-8.

26. Peng, C., et al., *Physics of direct-contact ultrasonic cloth drying process.* Energy, 2017. **125**: p. 498-508.

27. Momen, A.M., et al., *Dryer using high frequency vibration*. 2018, Ut-Battelle LLC.

28. Deepu, P., C. Peng, and S. Moghaddam, *Dynamics of ultrasonic atomization of droplets.* Experimental Thermal and Fluid Science, 2018. **92**: p. 243-247.

29. Peng, C., A.M. Momen, and S. Moghaddam, *An energy-efficient method for direct-contact ultrasonic cloth drying.* Energy, 2017. **138**: p. 133-138.

30. Dupuis, E.D., et al., *Electroelastic investigation of drying rate in the direct contact ultrasonic fabric dewatering process.* Applied Energy, 2019. **235**: p. 451-462.

31. Dupuis, E., et al., *Multiphysics modeling of mesh piezoelectric atomizers.* Proc. SPIE Smart Structures and Materials + Nondestructive Evaluation and Health Monitoring, 2018. **10595**: p. 1-9.

32. Dupuis, E.D., et al., *Ultrasonic Piezoelectric Atomizers: Electromechanical Modeling and Performance Testing*, in *Smart Materials, Adaptive Structures and Intelligent Systems*. 2018, ASME: San Antonio, TX.

33. Anton, S.R. and H.A. Sodano, *A review of power harvesting using piezoelectric materials (2003–2006).* Smart Materials and Structures, 2007. **16**(3): p. R1-R21.

34. Shahab, S. and A. Erturk, *Contactless ultrasonic energy transfer for wireless systems: acoustic-piezoelectric structure interaction modeling and performance enhancement.* Smart Materials and Structures, 2014. **23**(12): p. 1-13.

35. Shahab, S., M. Gray, and A. Erturk, *Ultrasonic power transfer from a spherical acoustic wave source to a free-free piezoelectric receiver: Modeling and experiment.* Journal of Applied Physics, 2015. **117**(104903): p. 1-8.

36. Shahab, S., D. Tan, and A. Erturk, *Hydrodynamic thrust generation and power consumption investigations for piezoelectric fins with different aspect ratios.* The European Physical Journal Special Topics, 2015. **224**(17-18): p. 3419-3434.

37. Shahab, S., S. Zhao, and A. Erturk, *Soft and Hard Piezoelectric Ceramics and Single Crystals for Random Vibration Energy Harvesting.* Energy Technology, 2018. **6**(5): p. 935-942.

38. Roundy, S. and P.K. Wright, *A piezoelectric vibration based generator for wireless electronics.* Smart Materials and Structures, 2004. **13**(5): p. 1131-1142.

39. Fan, K., et al., *Design and development of a multipurpose piezoelectric energy harvester.* Energy Conversion and Management, 2015. **96**: p. 430-439.

40. Wang, Y., et al., *A renewable low-frequency acoustic energy harvesting noise barrier for high-speed railways using a Helmholtz resonator and a PVDF film.* Applied Energy, 2018. **230**: p. 52-61.

41. Zhang, J. and L. Qin, *A tunable frequency up-conversion wideband piezoelectric vibration energy harvester for low-frequency variable environment using a novel impact- and rope-driven hybrid mechanism.* Applied Energy, 2019. **240**.

42. Ju, S. and C.-H. Ji, *Impact-based piezoelectric vibration energy harvester.* Applied Energy, 2018. **214**: p. 139-151.

43. Shin, Y.-H., et al., *Piezoelectric polymer-based roadway energy harvesting via displacement amplification module.* Applied Energy, 2018. **216**: p. 741-750.

44. Shahab, S. and A. Erturk, *Electrohydroelastic Euler–Bernoulli–Morison model for underwater resonant actuation of macro-fiber composite piezoelectric cantilevers.* Smart Materials and Structures, 2016. **25**(10).

45. Shahab, S. and A. Erturk, *Coupling of experimentally validated electroelastic dynamics and mixing rules formulation for macro-fiber composite piezoelectric structures.* Journal of Intelligent Material Systems and Structures, 2016. **28**(12): p. 1575-1588.

46. https://www.steminc.com/PZT/en/pzt-atomizer-transducer-100-khz. Available from: https://www.steminc.com/PZT/en/pzt-atomizer-transducer-100-khz.

47. Meesala, V.C., M.R. Hajj, and S. Shahab, *Modeling and identification of electro-elastic nonlinearities in ultrasonic power transfer systems.* Nonlinear Dynamics, 2019. **99**(1): p. 249-268.

48. Anton, S.R., A. Erturk, and D.J. Inman, *Multifunctional self-charging structures using piezoceramics and thin-film batteries.* Smart Materials and Structures, 2010. **19**(11): p. 1-15.

49. Tiersten, H.F., *Linear Piezoelectric Plate Vibrations*. 1969: Plenum Press.

50. Meesala, V.C. and M.R. Hajj, *Identification of nonlinear piezoelectric coefficients.* Journal of Applied Physics, 2018. **124**(065112): p. 1-11.

51. Meesala, V.C., M.R. Hajj, and S. Shahab, *Modeling electroelastic nonlinearities in ultrasound acoustic energy transfer systems*, in *Active and Passive Smart Structures and Integrated Systems XII*. 2018.

52. Meesala, V.C., M.R. Hajj, and S. Shahab, *Modeling and identification of electro-elastic nonlinearities in ultrasonic power transfer systems.* Nonlinear Dynamics, 2019.

53. Guo, N., *The vibration characteristics of piezoelectric discs*. 1989, University of London.

54. Guo, N., P. Cawley, and D. Hitchings, *The finite element analysis of the vibration characteristics of piezo-electric discs.* Journal of sound and vibration 1992. **159**(1): p. 115-138.

55. Kunkel, H., S. Locke, and B. Pikeroen, *Finite-element analysis of vibrational modes in piezoelectric ceramic disks.* IEEE Transactions on ultrasonics, ferroelectrics, and frequency control, 1990. **37**(4): p. 316-328.

56. Wagner, U.v. and P. Hagedorn, *Piez-Beam systems subjected to weak electric field: experiments and modelling of non-linearities.* Journal of Sound and Vibration, 2002.

Chapter 4

Solution of mist ejection rates at the microscopic level

Abstract

Microchannels are increasingly incorporated in MEMS systems due to their high rates of heat and mass transfer, as well as their ability to utilize molecular interactions. Recently, researchers at Oak Ridge National Lab have utilized piezoelectric transducers with arrays of microchannels for the purpose of clothes drying without the need for applied thermal energy. In this process, a piezoelectric transducer comprised of a thin steel plate with annular PZT rings adhered to its surfaces is actuated in the ultrasonic range. The resulting deformation at resonance accelerates the fabric at large magnitudes causing the contained water to separate into smaller droplets, referred to as atomization. The droplets are then forced through microchannels within the steel plate where they are quickly removed from the area around the fabric. Modeling of the flow in this system is complicated by the small aspect ratio, nonlinear geometry, time varying entrance conditions, and adhesion to the channel. Further difficulties arise from small variations in channel sizes due to manufacturing imperfections; at such small hydraulic diameters these differences can drastically alter the flow rate of the channel from what is expected. Experimental measurements are also made difficult due to the small length of the channel and its oscillating motion. In this chapter, we will discuss modeling techniques for this case of open-ended microchannel under oscillatory motion, used in direct contact ultrasonic clothes drying.

4.1 Introduction

The limits of applying macroscopic flow theory based on the continuum assumption to microchannels has been an increasing area of interest. The rise of microelectromechanical systems (MEMS) use in sensing, actuation, heat transfer, and energy harvesting has grown substantially in recent years, and the study of liquid flows at these scales is increasing in importance. The principle characteristic for applying our understanding of macroscopic flows to microchannels are several dimensionless numbers relating inertial, viscous, and surface tensions forces. These include the Bond number, the Weber number, and the Reynolds number, where critical values for flow transition occur around $\mathrm{Re} \sim 2,000$ [1]. While inertial effects are rarely included in microfluidic processes, the high operating frequencies of ultrasonic drying resulting in short time scales for the flow results in these forces being substantial. Further considerations include the wetting of various materials the microchannels are created from, affecting all areas of the flow. For hydrophilic materials, it was found the Navier-Stokes equation holds at channel sizes greater than ten molecular diameters, allowing for the application of the continuum hypothesis to the problem at hand [2]. However, a lapse in research was found for high frequency flows in short, micrometer scale channels. These follows are characterized by a strong influence from entrance effects, channel profile, and air entrainment when considering two phase flow such as in an oscillating jet. In this investigation, we will study such channels as they relate to direct contact ultrasonic clothes drying, where the actuation of these flows comes from the ultrasonic vibrations of a circular disk.

The limits of investigations on oscillating flows in the millimeter scale has not exceeded the ~100 Hz range, however there are applications where piezoelectric flow control has the potential to reach the kHz scale [3, 4]. One such application is the atomization of liquids, commonly used in nebulizers and recently in an ultrasonic clothes dryer developed by researchers

at Oak Ridge National Lab [5, 6]. These technologies utilize a piezoelectric transducer with a stainless-steel substrate, fabricated with an array of microchannels for the transport of atomized water. In this application, wall friction drives the flow creating pressure gradients rather than vice-versa, in this manner the relative motion of the substrate is used as the boundary condition for the micron-scale flow.

Moreover, the influence of channel profiles greatly influences the flows in short channels where entrance effects are substantial. The funneling effect of nozzles, as well as nonlinearly tapered channels greatly increases the mass flow rate capabilities of the piezoelectric atomizer, increasing the performance of ultrasonic drying and other applications. The inclusion of oscillating flows in these non-uniform channels is a further area lacking investigations. The authors have identified only two approaches in literature, numerical and experimental, towards modeling tapered channels, steady and oscillating, respectively. The difficulty of experimental techniques for the short channels at oscillating frequencies in the kHz range makes numerical approaches with validations from literature one of the few currently available methods. Further complexity arises when dealing with two phases, occurring in oscillating flows; air entrainment at the exit of the channel increases the likelihood of encountering turbulent flow, due to localized Reynolds numbers reaching high values of magnitude.

The oscillating plate is able to achieve droplet ejection due to the inertia of the fluid filling the microchannel. As we are working with the drying of fabrics, we will assume the fluid is always water, and is considered incompressible. Next, we will need to estimate the fluid regime we expect to encounter, laminar or turbulent, due to the operating conditions of the transducer. For this we turn to the Reynolds number, given as $\mathrm{Re} = \rho UD / \mu$ where ρ is the fluid density, U is the characteristic velocity, D is the characteristic length scale, and μ is the viscosity. The Reynolds

number allows us to estimate the relative importance of inertial and viscous forces in the flow. For water in a microchannel oscillating at several to tens of meters per second, the maximum Reynolds number achieved is approximately Re=1,260, implying the flow is safely in the laminar regime [1, 7-9]; however, this is only the case when dealing with single phase flow. When air is entrained into the microchannel, the two-phase flow characteristics will be found to introduce turbulence to the system.

For interfacial flows where droplet generation occurs, the capillary number, defined as the ratio $Ca \sim F_\mu / F_\sigma \sim \mu U / \sigma$, is more commonly used, as it provides insight into the ratio of viscous forces to the surface tension of the liquid. During this process, three major steps occur in sequence: initially, an immiscible interface separates the two phases of fluid, then a large deformation of the interface occurs until an unstable state is reached due to necking of the fluid, at this point pinch-off occurs and a droplet is released from the bulk liquid. As the length scale of the channel decrease, the viscous and interfacial forces increase, leading to a greater importance in the capillary number [10].

For most microfluidic flows, inertia is not a strong force as the volume of liquid is incredibly small; however, for flows where acceleration and velocity reach high magnitudes, such as in an oscillating jet, inertia will contribute to the ability for a droplet to reach capillary pinch-off. For this reason, we will also include the Weber number in our analysis, comparing the liquid inertia and surface tension forces. The Weber number is defined as $We \sim F_i / F_\sigma \sim \rho D U^2 / \sigma$.

These three numbers, the Reynolds number, Capillary number, and Weber number, will be used in conjunction to characterize the flow and give physical insight into how the dimensions of the microchannel effects droplet ejection. Comparisons of flow parameters such as flow rate, and

velocity gradients against these dimensionless numbers will allow for the quantification of forces allowing for improvements to be made to increase water shedding performance.

Having modeled the entirety of the piezoelectric transducer used in early prototypes of the ultrasonic dryer, we can predict the velocity of the contacting plate at as a function of its radius. We then seek to connect the velocity of the plate, also being the microchannel walls, to the flow rate of water through the channel. This is representative of Couette flow as the no-slip wall condition causes viscous dissipation to create a velocity gradient within the channel. Difficulties arise from the open-ended microchannel inlet and outlet, the short channel increasing entrance effects, rough wall conditions due to the subtractive process used to form the channels, as well as the possibility of air entrainment. The high frequency of operation is another area that has yet to be investigated to the author's best knowledge. Typical oscillatory flows in literature are limited to the hundreds of Hz scale, whereas the piezoelectric device in this investigation operate between 40 and 100 kHz.

4.2 Analytical approximation

The modeling efforts in chapter 2 allows for the prediction of the displacement of each of the microchannel holes. It is hypothesized that a close approximation to the mist ejection is a calculation of the displaced area during the ejection portion of the oscillatory cycle; therefore, we will multiply the outlet area by the displacement of the microchannel for calculation of the swept volume during one half cycle of the plate's motion; moreover, this motion is repeated many times over a short duration due to the high frequencies of motion.

To begin modeling efforts, a sample of the microchannel holes is needed for inputting their radial distance from the center into equation 2.15. Figure 4.1 shows such an array of 5,000 evenly

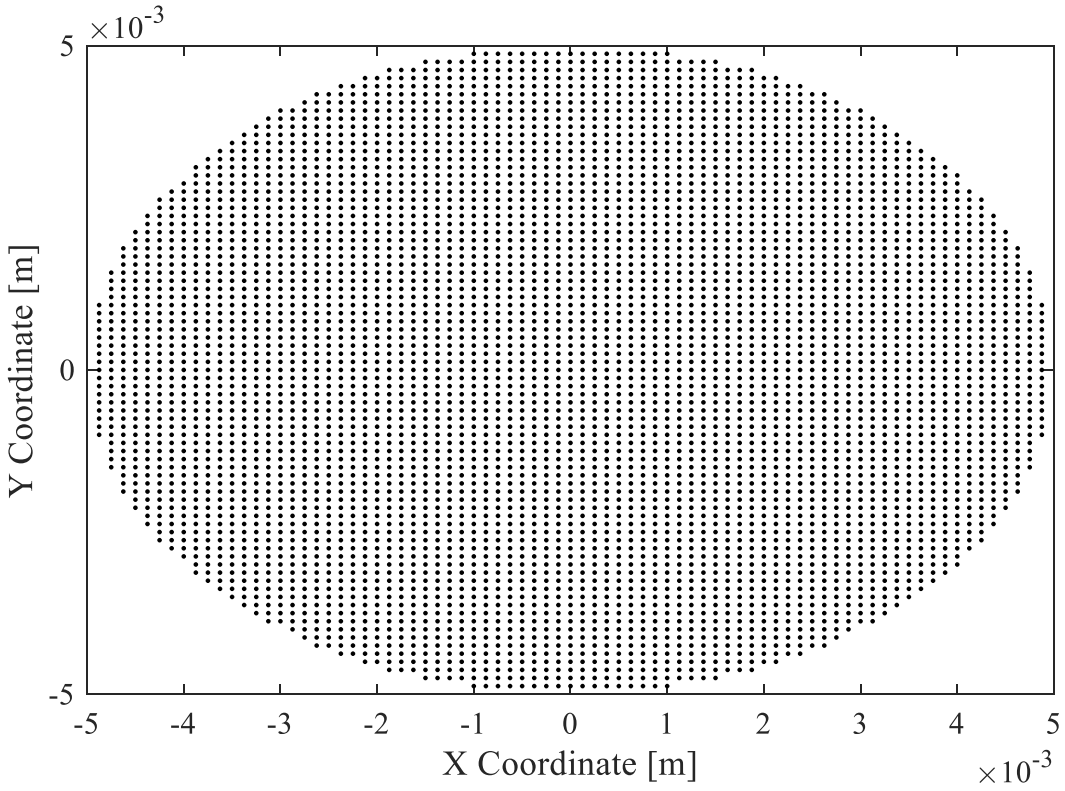

Figure 4.1. Microchannel grid sampling.

spaced outlets of the microchannels with a diameter of 10 μm. The radial distance of each point is calculated by $r = \sqrt{x^2 + y^2}$.

For each microchannel, its displacement is calculated for a given voltage input to the bimorph, and then plotted against its coordinate position. Figure 4.2 shows the results of the analytical equation 2.15 for each of the sampled points in figure 4.1.

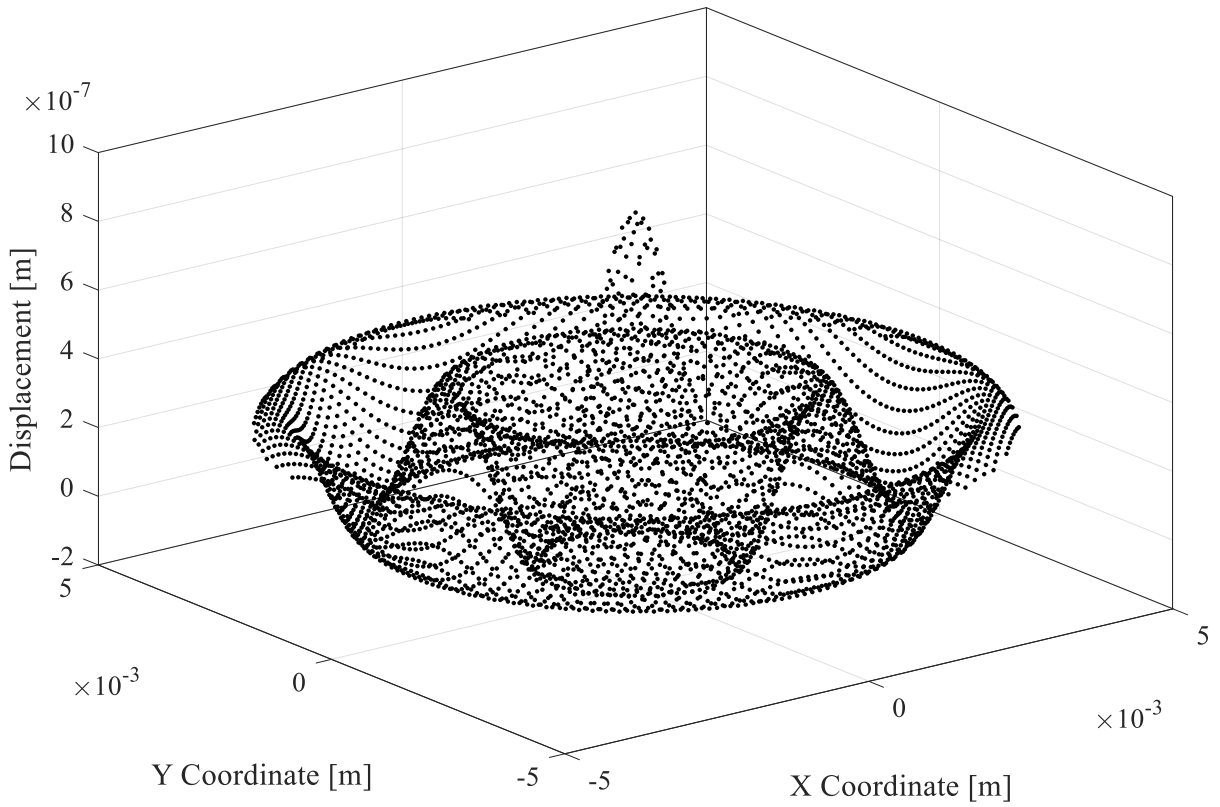

Figure 4.2. Microchannel array displacement profile at resonance and 30 V input.

Next, the total swept volume of the array of microchannels is calculated by summing the displacement for each of the channels plotted in figure 4.2 and multiplying by the inlet area of the channel. To find the total volume over a unit of time, this value is multiplied by the frequency of operation. The total volume per unit time is estimated as

$$\frac{\bar{V}}{t} = \frac{\omega}{2\pi} A_{inlet} \sum_{p=1}^{P} w_{outlet}(r_p)$$

$$\frac{\bar{V}}{t} = f\pi\left(35\times10^{-6}\right)^2 \sum_{p=1}^{P}\sum_{n=1}^{\infty} \phi_n(r_p) \frac{2\pi\rho h\omega^2 W_o \int_0^a r\phi_n(r)dr}{\omega_n^2 - \omega^2 + 2j\zeta_n\omega_n\omega} \quad . \tag{4.1}$$

To confirm this model, experiments are conducted to measure the volume flow rate through the array of microchannels. Two volumes of water are used for testing, 100 μL and 300 μL. Each volume is atomized on the transducer for a given voltage input, and the time taken for the complete volume to be turned to mist is recorded. This process is repeated three times for each voltage and initial water volume combination, and the average of the three taken as the final measurement. Figure 4.3 shows the results of these experiments compared with the analytical models flow rate predictions.

It can be seen that for low values of input voltage, the model accurately predicts the flow rate through the array of microchannels, but at increasing voltages a discrepancy emerges. This is due to the nonlinear increase in output acceleration at increasing voltages, due to the displacements of the plate exceeding the thickness of the plate. When displacements approach and exceed the

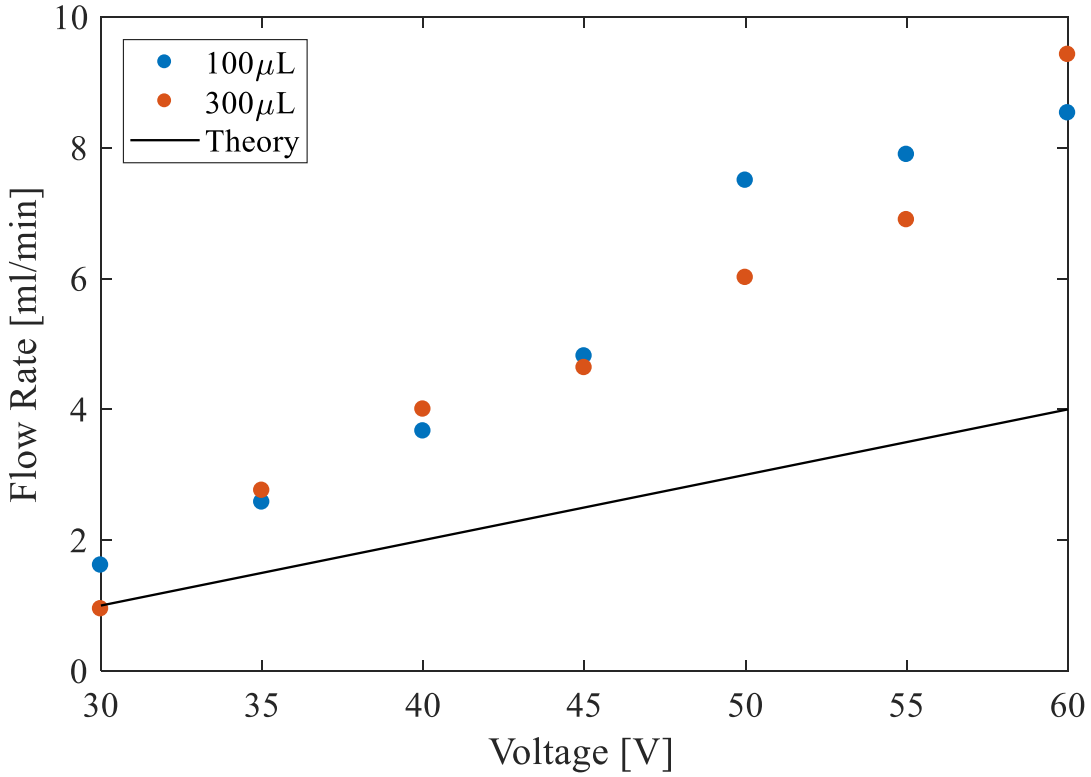

Figure 4.3. Flow rate experimental measurements compared to analytical predictions.

thickness of the plate, our assumption of classical plate theory does not hold. This is evident from figure 2.B1, where the center acceleration does not follow the same linear trends at higher voltages as is achieved with lower voltages. In fact, the linear assumption begins to breakdown at applied voltages of ~20V and operating frequencies exceeding ~100 kHz. This characteristic of the transducer complicates modeling efforts as the nonlinear displacements of the plate would need to be accounted for in order for the model to hold at high magnitudes of displacement.

4.3 Computational fluid-dynamics

In order to investigate the microscopic flows at high oscillatory frequencies, we turn to numerical simulations using COMSOL Multiphysics. In this model, we simulate the same high frequency oscillation of the plate interacting with an initially stationary fluid filled cavity with an outlet feeding into the ambient air. The goal of this investigation is to identify the importance of various forces within the channel for future modeling efforts.

We will use two modules of COMSOL to achieve the desired results: fluid structure interactions to simulate the plate moving throw the fluid, and turbulent flow within the channel that solves the Navier-Stokes equation numerically. The level set method is used to simulate a moving interface, a necessary feature due to the droplet interface being transported through the channel and into ambient air. This method calculates a contour line of the interface and numerically solves for its displacement, denoted as the level set function. This equation is given as

$$\frac{\partial \phi}{\partial t} + \mathbf{u} \cdot \nabla \phi = \gamma \nabla \cdot \left[\varepsilon \nabla \phi - \phi(1-\phi) \frac{\nabla \phi}{|\nabla \phi|} \right] \tag{4.1}$$

where ϕ is the level set function, ε determines the thickness of the interface region ranging from zero to one, γ determines the stabilization of the level set function, and $\mathbf{u}$ is the interface velocity vector. It can be seen that the left-hand side of equation 4.1 provides the motion of the interface, and the right-hand side provides corrections necessary for numerical stability [11].

The model configuration can be seen in figure 4.4. The tapered microchannel is modeled as an undeforming and impenetrable wall, oscillating through the fluids as dictated by the plate modeling efforts in chapter 2. The microchannel is initially filled with water, as well as having a thin film of water above the plate denoting the supply of water that a fabric will deposit on the plate. The outlet feeds into ambient air, where this condition can also be seen above the supply of water to simulate atmospheric conditions and to allow for atomized water to travel both upwards and downwards through the channel. The left boundary is an axisymmetric boundary, which allows for simplification of the model while still modeling for the entirety of the channel diameter. The right boundary for the air and water are also given as symmetric boundaries, to keep water contained above the plate, but the geometry of this region is not included in the simulation as we are mainly concerned with the flow through the channel. These simplifications of the geometry allow for a timelier simulation to be completed, a necessary feature when dealing with computational fluid dynamics, notorious for long simulation times.

Snapshots of the simulations can be seen in figure 4.5, showing one complete cycle of motion of the plate through the fluids. The initial upwards motion results in air entrainment within the channel, complicating the dynamics of the problem by introducing two phase flow considerations. As time progresses, we see a jet being ejected from the outlet of the channel, as well as swirling of the entrained air due to vorticity within the moving channel. From these models,

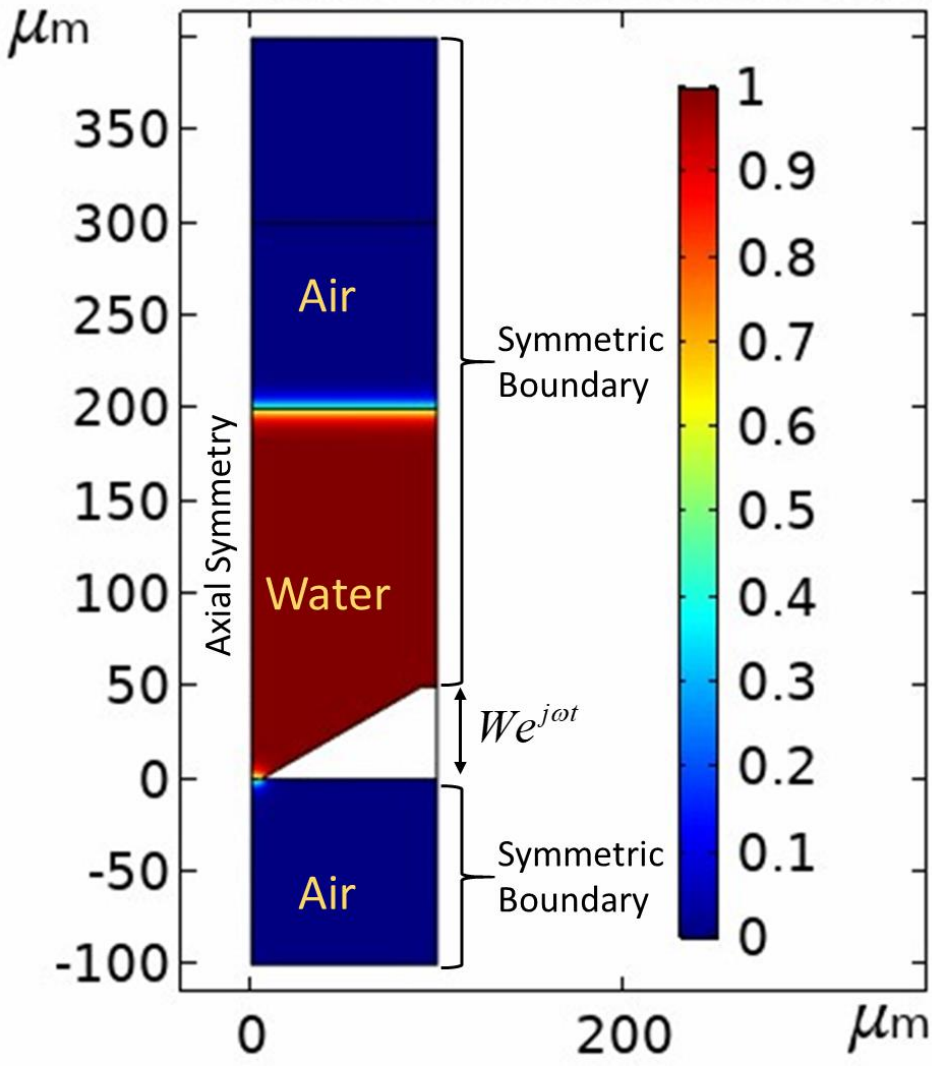

Figure 4.4. CFD model geometry and boundary conditions.

we are able to calculate the velocity of the water moving through the channel in order to quantify the magnitude of forces at hand. The maximum velocity of the fluid during these oscillatory motions reaches 124 m/s, resulting in a Capillary number of approximately 1.6, and a Weber number of 1,059. These two numbers show that viscous forces are on par with the effects of surface tension, but also tells that inertial forces are significantly higher than both viscous and surface tension effects. This is not much of a surprise as the high magnitudes of the changing directionality of the flow has not been studied previously, and gives insight into the forces that must be considered for accurate modeling to be achieved.

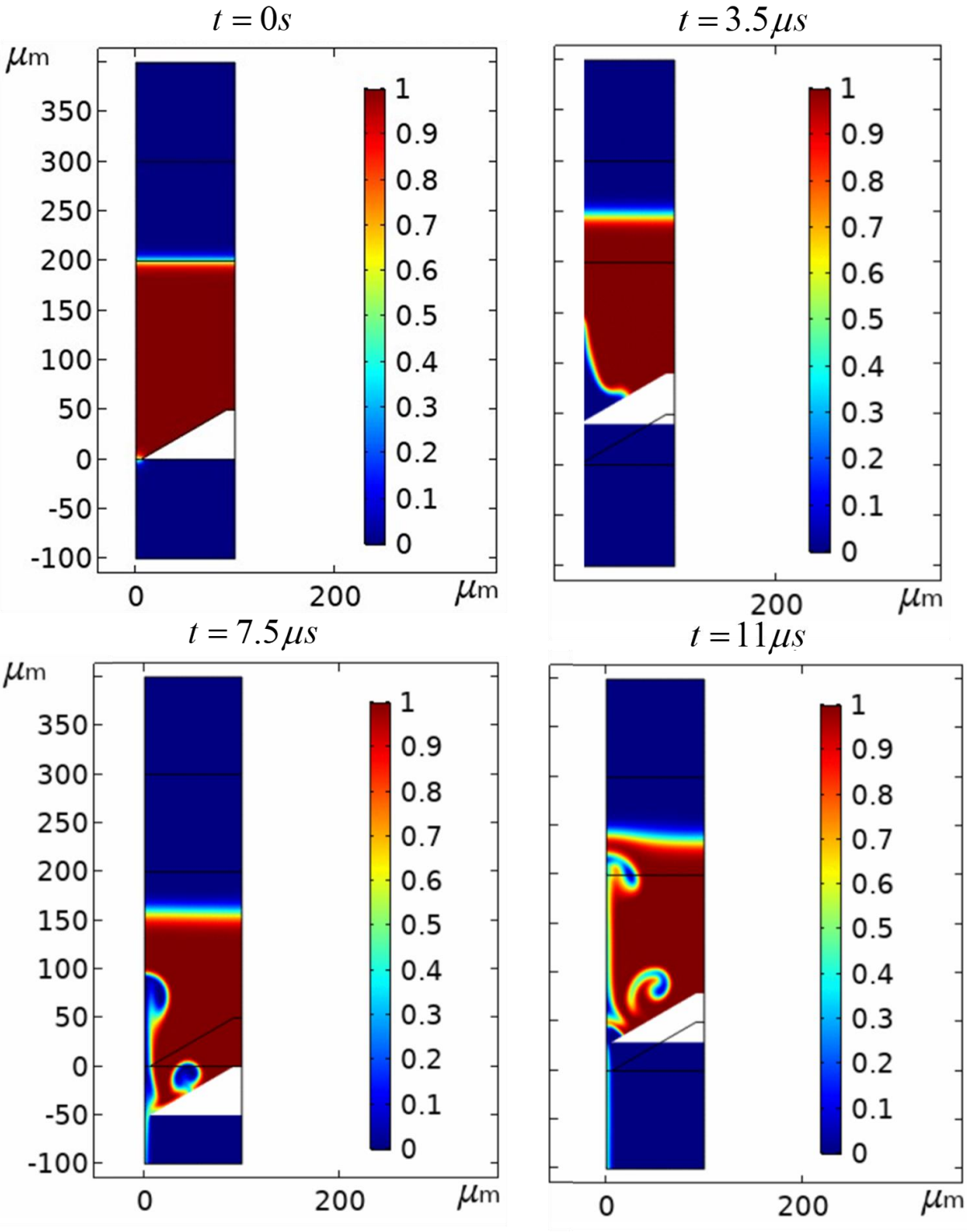

Figure 4.5. CFD simulation snapshots at various times during one cycle of motion.

Furthermore, negative pressure within the channel highlights the occurrence of cavitation within the channel. The high pressures emanating from the motion of the plate is sufficiently intense to rapidly turn certain areas of the flow into a gas, greatly complicating the physics within the channel. Previous investigations have highlighted the presence of cavitation during the atomization process, so it is not surprising that such events occur within the shedding of water through the plates microchannels [12, 13]. As there are no models which couple the motion of the plate to cavitation, this will be a very interesting area of research and one that would need much attention in future works.

Bibliography

1. Sharp, K.V. and R.J. Adrian, *Transition from laminar to turbulent flow in liquid filled microtubes.* Experiments in Fluids, 2004. **36**(5): p. 741-747.
2. Travis, K.P., B.D. Todd, and D.J. Evans, *Departure from Navier-Stokes hydrodynamics in confined liquids.* The American Physical Society, 1997. **55**(4): p. 4288-4295.
3. Osman, O.O., H. Shintaku, and S. Kawano, *Development of micro-vibrating flow pumps using MEMS technologies.* Microfluidics and Nanofluidics, 2012. **13**(5): p. 703-713.
4. Gaver, D.P. and J.B. Grotberg, *An experimental investigation of oscillating flow in a tapered channel.* Journal of Fluid Mechanics, 2006. **172**(-1).
5. Peng, C., et al., *Physics of direct-contact ultrasonic cloth drying process.* Energy, 2017. **125**: p. 498-508.

6. Pan, C.T., J. Shiea, and S.C. Shen, *Fabrication of an integrated piezo-electric micro-nebulizer for biochemical sample analysis.* Journal of Micromechanics and Microengineering, 2007. **17**(3): p. 659-669.

7. Darbyshire, A.G. and T. Mullin, *Transition to turbulence in constant-mass-flux pipe flow.* Journal of Fluid Mechanics, 2006. **289**: p. 83-114.

8. *MEMS: Background and Fundamentals*. 2 ed, ed. M. Gad-el-Hak. 2006, Boca Raton, FL: Taylor & Francis Group.

9. Koo, J. and C. Kleinstreuer, *Liquid Flow in microchannels: experimental observations and computational analyses of microfluidics effects.* JOURNAL OF MICROMECHANICS AND MICROENGINEERING, 2003. **13**: p. 568-579.

10. Zhu, P. and L. Wang, *Passive and active droplet generation with microfluidics: a review.* Lab Chip, 2016. **17**(1): p. 34-75.

11. Multiphysics, C. *CFD Module User's Guide*. Available from: https://doc.comsol.com/5.4/doc/com.comsol.help.cfd/CFDModuleUsersGuide.pdf.

12. Ramisetty, K.A., A.B. Pandit, and P.R. Gogate, *Investigations into ultrasound induced atomization.* Ultrason Sonochem, 2013. **20**(1): p. 254-64.

13. Mir, J.M., *Cavitation-induced capillary waves in ultrasonic atomization.* The Journal of the Acoustical Society of America, 1980. **67**(1): p. 201-205.

Chapter 5

Design of an alternative tumble dryer prototype

Abstract

Direct contact ultrasonic clothes drying, a novel application of ultrasonic vibrations for the purpose of drying textiles is a promising solution for ultra-efficient clothes drying technology. Developed by researches in 2016 at Oak Ridge National Laboratory, this concept utilizes the atomization of liquids exposed to high frequency vibrations, creating a mist of micrometer sized droplets from the bulk liquid retained in fabrics. Previous investigations have utilized arrays of 30mm diameter transducers, and while these have been shown to be more efficient than thermal drying, they are limited by the amount of contact area that can be made with the fabric. The packing density of these transducers leaves much dead space where the fabric must wick water to the locations of atomization. In this section, we will analyze a large area dryer concept which utilizes large plates rather than small discs to contact and dry the fabric. The advantages of this technology will be shown to be the simplicity of the design, large contact area, and several control parameters to achieve resonance matching between the vibrating plate and piezoelectric actuators. Due to the increased mass of the system, the actuators chosen are bolt clamped Langevin transducers, with increased forcing capabilities compared to the annular bimorph F100 transducers. Comparisons will be on the basis of output acceleration and power consumption, where it will be shown the plate dryer concept has the ability to achieve drying with a sixteenth of the energy consumption.

5.1 Introduction

Resonance matching between an actuation source and electromechanical systems is a necessity for many applications, including energy harvesting, vibration control and isolation, microelectromechanical systems (MEMS), and recently in direct contact ultrasonic clothes drying [1]. Of these systems, material properties, geometry, and boundary conditions are highly influential on the systems natural frequency and performance. Damping from over constraining devices due to the rigid boundaries, excessive strain, and material imperfections can be identified through comparisons of vibration models with experimental measurements.

Vibrational systems can be designed creatively to provide maximum performance with minimum input energy, through optimization of the previously defined parameters influencing the systems performance. In this view, we aim to maximize the contact area over which the fabric is actuated when atomization is realized, and to achieve resonance matching between the actuators and vibrating contact area. This section will investigate parameters such as the boundary condition and number of actuators, in their influence on the vibration characteristic of the plate.

5.2. Motivation

The currently used piezoelectric transducer has limited potential due to its small contact area, requiring a massive amount of transducers to cover any substantial area, a necessary feature for drying clothing [1-3]. Manufacturing costs will increase drastically when hundreds, if not thousands of these devices are bonded and wired to a supporting structure. Figure 5.1 shows such a prototype, comprised of sixteen modules with 28 piezoelectric transducers on each module for a total of 448 transducers. Each module has a fan to facilitate air movement through the fabric,

helping to ventilate the ejected mist. These modules move forwards and back, compressing the fabric between the transducers and meshed plate. Electronics are housed in the bottom shelf of the prototype, where waste heat is carried upwards, helping to increase the temperature of the fabric increasing drying capabilities at the same time as recovering lost energy.

With this in mind, we search for alternative dryer designs which utilizes a larger surface area for direct contact drying. For actuating a larger mass, it is also necessary to have the piezoelectric forcing increase in magnitude; however, this often comes with increased transducer mass, lowering the operating frequency of the device through the relation $\omega = \sqrt{k/m}$. While lower operating frequencies correlates to a lower critical acceleration necessary for atomization, given by equation (2.1), we must be weary of approaching the audible hearing range. These constraints make achieving atomization difficult as piezoelectric actuators have notoriously low vibration amplitudes at increasing magnitudes of frequency.

A preliminary investigation into the packing density of the currently used F100 transducer was performed to quantify the importance of achieving large area atomization. An aluminum plate was suspended from a load cell, and twenty-four transducers adhered to the plate in a honeycomb packing arrangement to increase the number of transducers that could fit inside a given area. The transducers were wired in parallel where each transducer could be connected or disconnected from the circuit to analyze the influence of the number of transducers actuated as well as the arrangement of the transducers. This experiment, pictured in figure 5.2, serves to provide insight into whether the same drying performance can be obtained from a carefully arranged array of transducers.

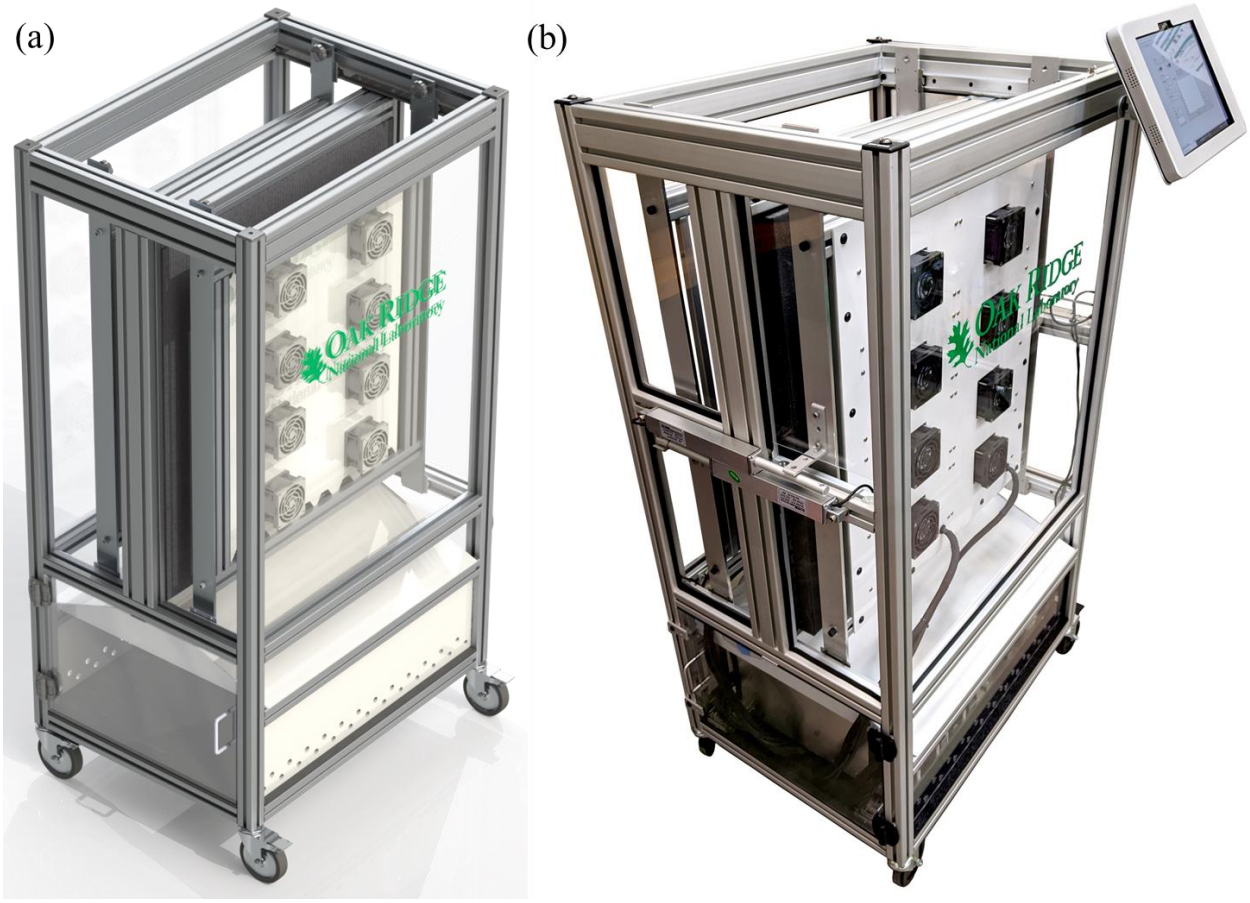

Figure 5.1. (a) CAD Rendering of the press-type dryer utilizing the F100 transducers, and **(b)** experimental prototype.

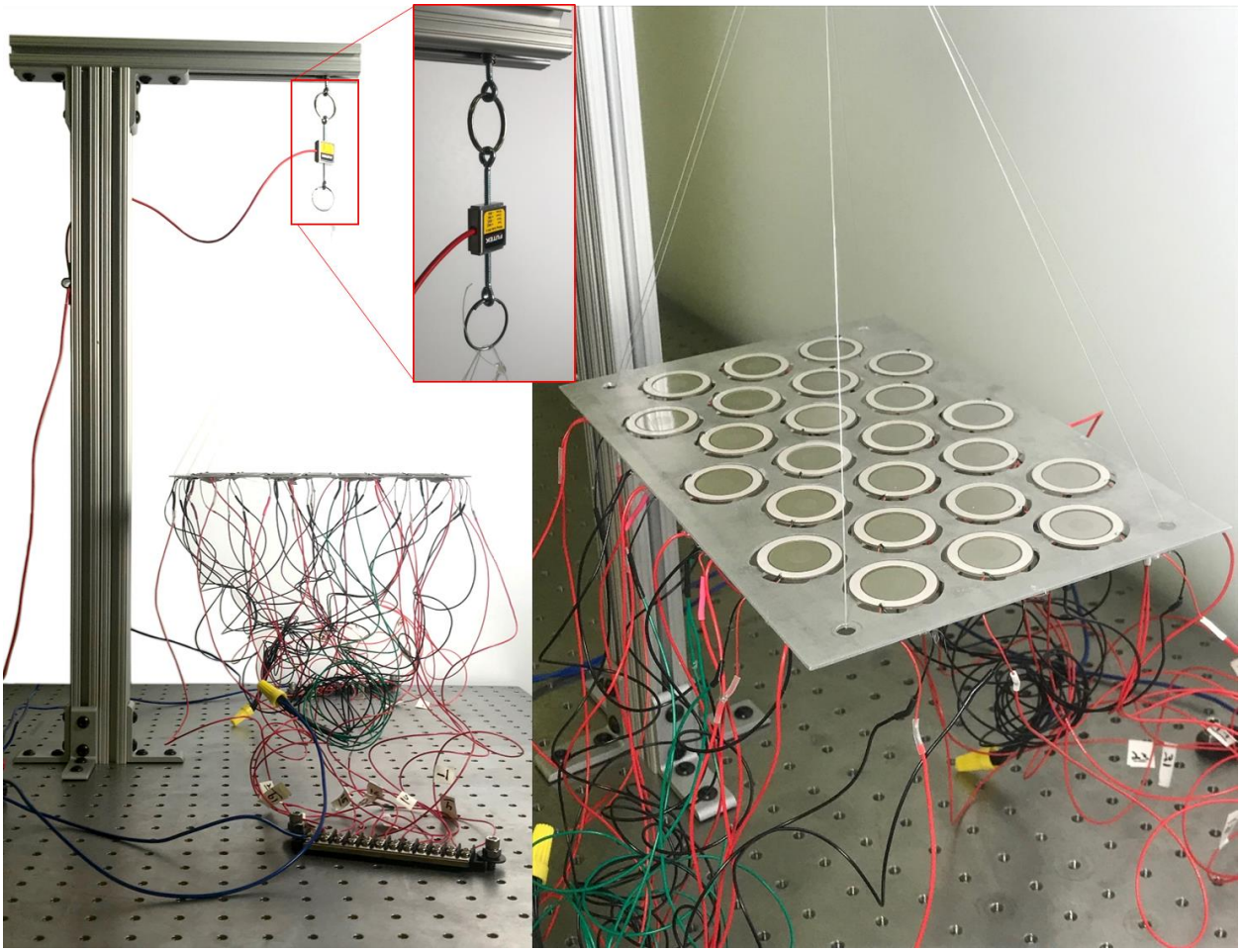

Figure 5.2. Packing density experiment with an array of transducers adhered to a plate and suspended from a load cell.

Seven different configurations are analyzed, where a saturated cloth with the same area as the plate is dried to completion. These arrangements can be viewed in figure 5.3, where a green circle denotes an active transducer, and a red circle an inactive transducer. The drying curves for each of these arrays are then plotted together at their bone-dry weight. The movement of the curves to the end point of the drying cycle is done to accurately compare the efficiency of configuration, where differences in beginning moisture content are insignificant.

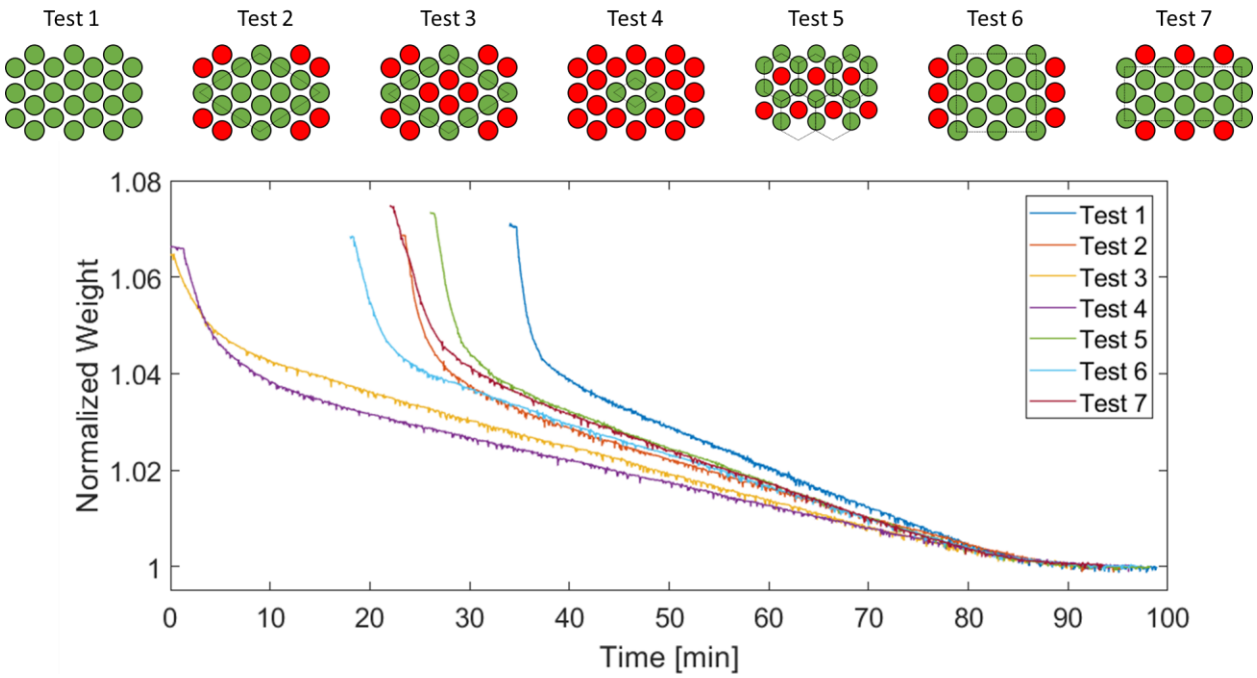

Figure 5.3. Drying curves for seven different packing density configurations aligned by the dry weight of the fabric to compare each arrangement's drying curves.

Following the collection of drying curves, a linear regression is performed between remaining moisture contents (RMC) of 52% and 5%. Damp clothes generally come out of a washing machine at 52% RMC, meaning they are not fully saturated once the drying process begins; therefore, we negate the nonlinear regime of drying for analysis of packing density, and instead focus on the linear portion. Further, DOE standard measurements for drying require clothing to be dried to 5% RMC, meaning they are not entirely bone dry. We then analyze this region by performing a linear regression, where the slope of the decay of water is the parameter of interest; a larger slope denotes an increase in drying performance.

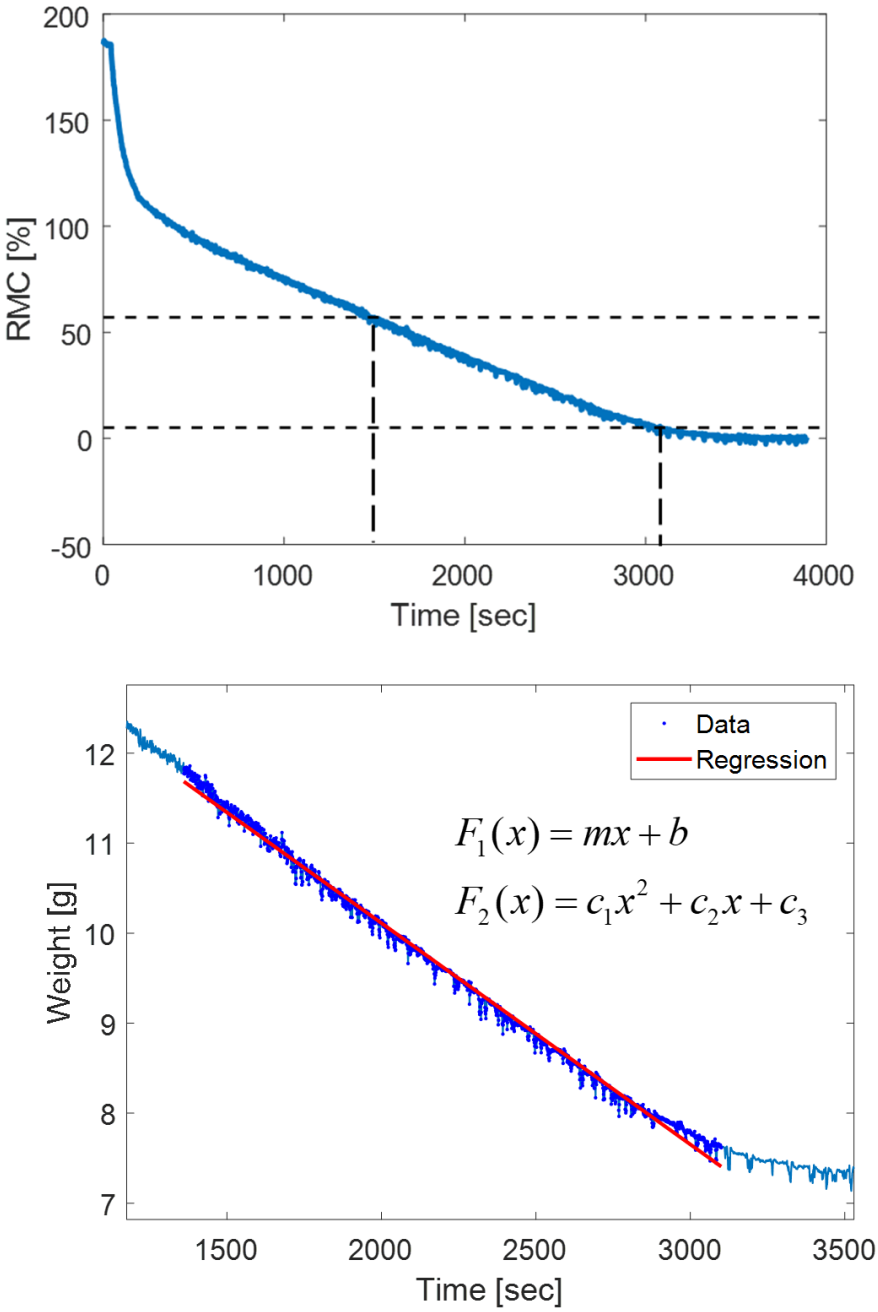

Figure 5.4. (a) Typical drying curve with the remaining moisture content (RMC) of 52% and 5% highlighted, and **(b)** the regression for the linear portion of drying between these moisture contents.

Following the fitting of a linear regression to each of the seven packing arrangements, the slopes of the drying curve are plotted against the ratio of transducer to fabric area. It can quickly be seen that there is an increase in the rate of water loss when more active transducers are present,

as more energy is being spent to the fabric. The exponential change from a high ratio, denoting significantly more fabric area than active drying area, to a lower ratio highlights the sensitivity of the system to the packing density.

It was observed that many of the transducers operate at slightly different natural frequencies, due to differences in mounting conditions as well as imperfections within the piezoelectric materials used. This drastically reduces the efficiency of the system as portions of the atomized area will experience significantly less acceleration than those where resonance is achieved; moreover, the dead-space between transducers must wick water to active areas of drying,

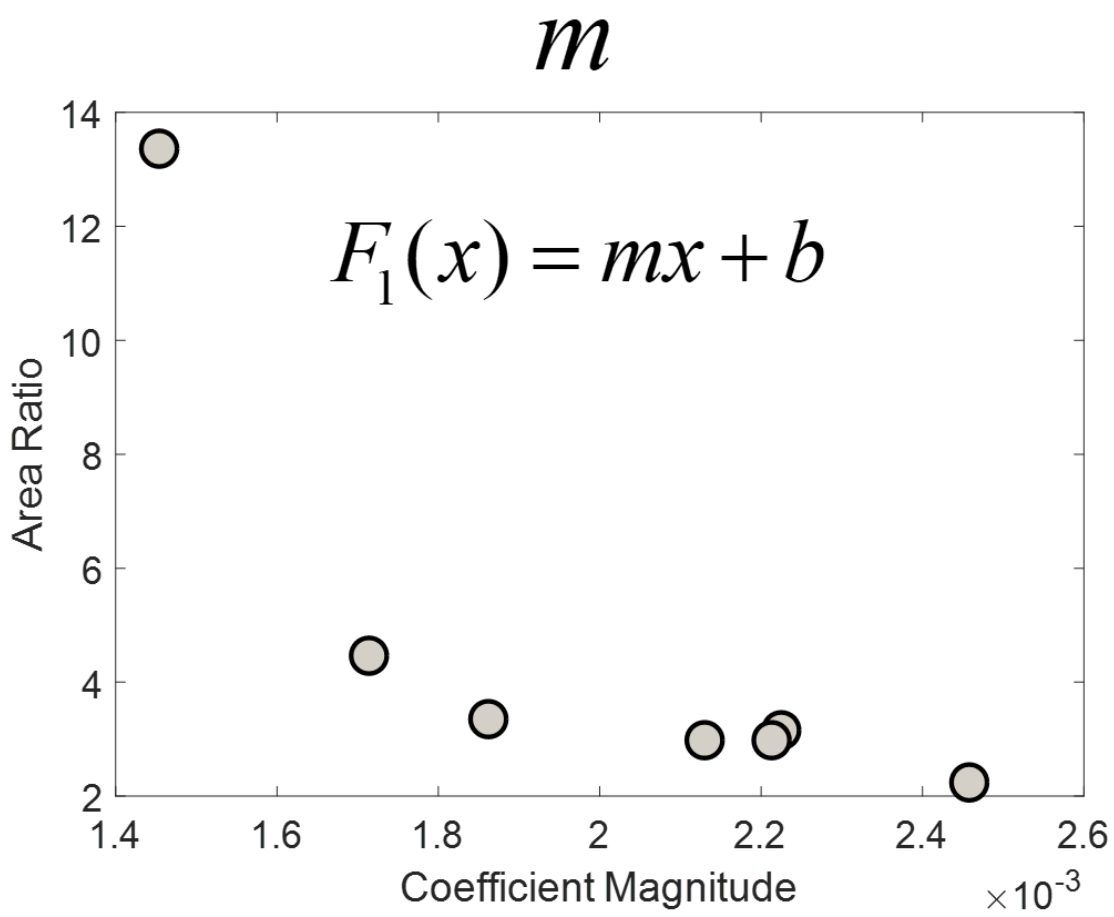

Figure 5.5. Linear drying slope compared to the area ratio of the transducer to fabric size for which the regression was fitted.

further increasing the time it takes to remove moisture. To avoid these discrepancies, we seek to vibrate the entire surface area contacting the wet fabric, to minimize dead-space and to achieve resonance throughout the entire structure.

5.3. Approach

For analysis of this concept, we will investigate a single section of plate actuated by either one or two bolt-clamped Langevin transducers connected on either end of the plate as given in figure 5.6. Proof of concept will be achieved through the realization of atomization, and improvements made from the collection of acceleration data through a single point LDV. COMSOL Multiphysics will be used in conjunction for confirmation of observations made through experiment leading to improvements in the design of the prototype. An emphasis will be placed on the boundary conditions connecting the plate to the transducers. When a single transducer is excited, the other acts as a rigid wall, restricting motion through the damping of vibrational modes. For the excitation of both transducers, a phase difference may also be used to investigate its influence of the output acceleration. Further, the applied tension used in mounting the plate will be another control parameter influencing the response of the plate to sinusoidal actuation.

We introduce a new parameter for measuring the effectiveness of large-scale devices as compared to the performance of the currently used transducer in this investigation. This parameter, power per unit area when atomization is achieved, will serve as baseline comparison for the scaling of this technology to a larger mass actuator and contact plate. We will introduce an applied tension to the plate as a control parameter for resonance matching between the actuator and plate.

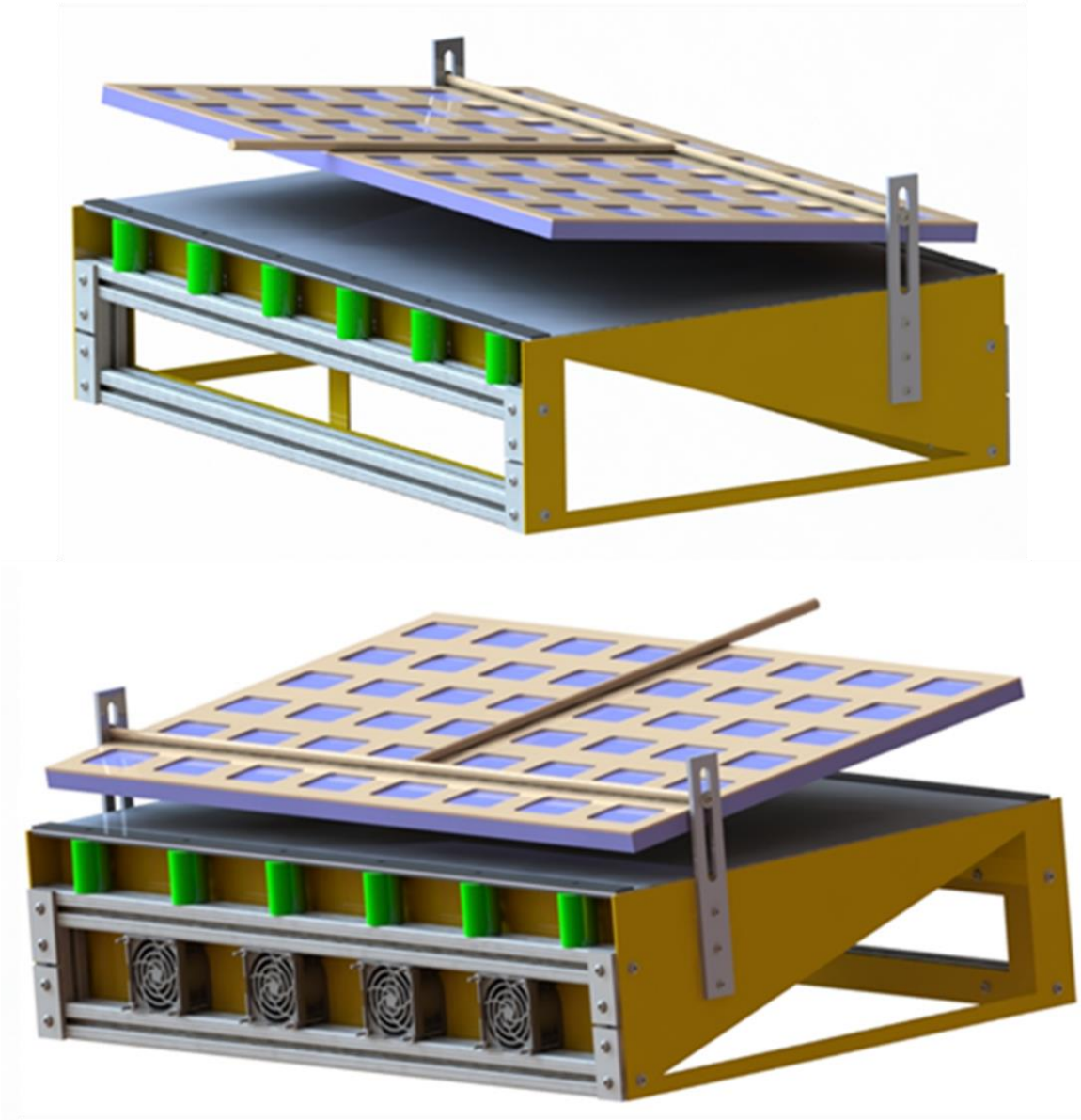

Figure 5.6. Press-type plate dryer prototype with six segmented and actuated strips.

Figure 5.6 shows a prototype of a press-type direct contact ultrasonic dryer, utilizing six plates actuated by Langevin transducers (green cylinders) rather than an array of smaller disc type transducers. The initial dimensions of the plate are chosen to be 24” x 5” x 1/64”, in order for the six arranged plates to cover the Department of Energy required fabric size for clothes drying

performance testing. A sloped bottom tray leads to an array of four fans for ventilating the mist away from the fabric, as well as drawing air through the system to facilitate drying.

5.4. Experiment

A single section of aluminum plate supported by two bolt-clamped Langevin transducers is pictured in figure 5.7. Two supporting blocks holding the Langevin transducers are mounted onto a strip of T-Slotted framing. A turnbuckle connects the two blocks, allowing for small adjustments of tension to be applied to the plate connecting the tops of the two Langevin transducers. Proof-of-concept was achieved by actuation of one or both transducers and realizing atomization at specific locations on the plate where the acceleration is sufficient to reach droplet ejection. It was quickly realized the original mass of the 5" wide plate was too large to achieve atomization, therefore the sides were cut to a width of 2.5", where the decrease in mass allowed for atomization to occur. Acceleration measurements are recorded experimentally with a LDV at the center of the plate as well as over the transducers.

Through fine tuning of the tensioner, we are able to match one of the many natural frequencies of the plate to that of the transducer. This in turn results in resonance matching, leading to high magnitudes of acceleration from the wave propagation emanating from the transducer through the plate. We are then able to observe atomization via the upward ejection of a mist from the bulk liquid on the plate. Future designs will incorporate microchannel perforations within the plate, to better facilitate the shedding of liquid.

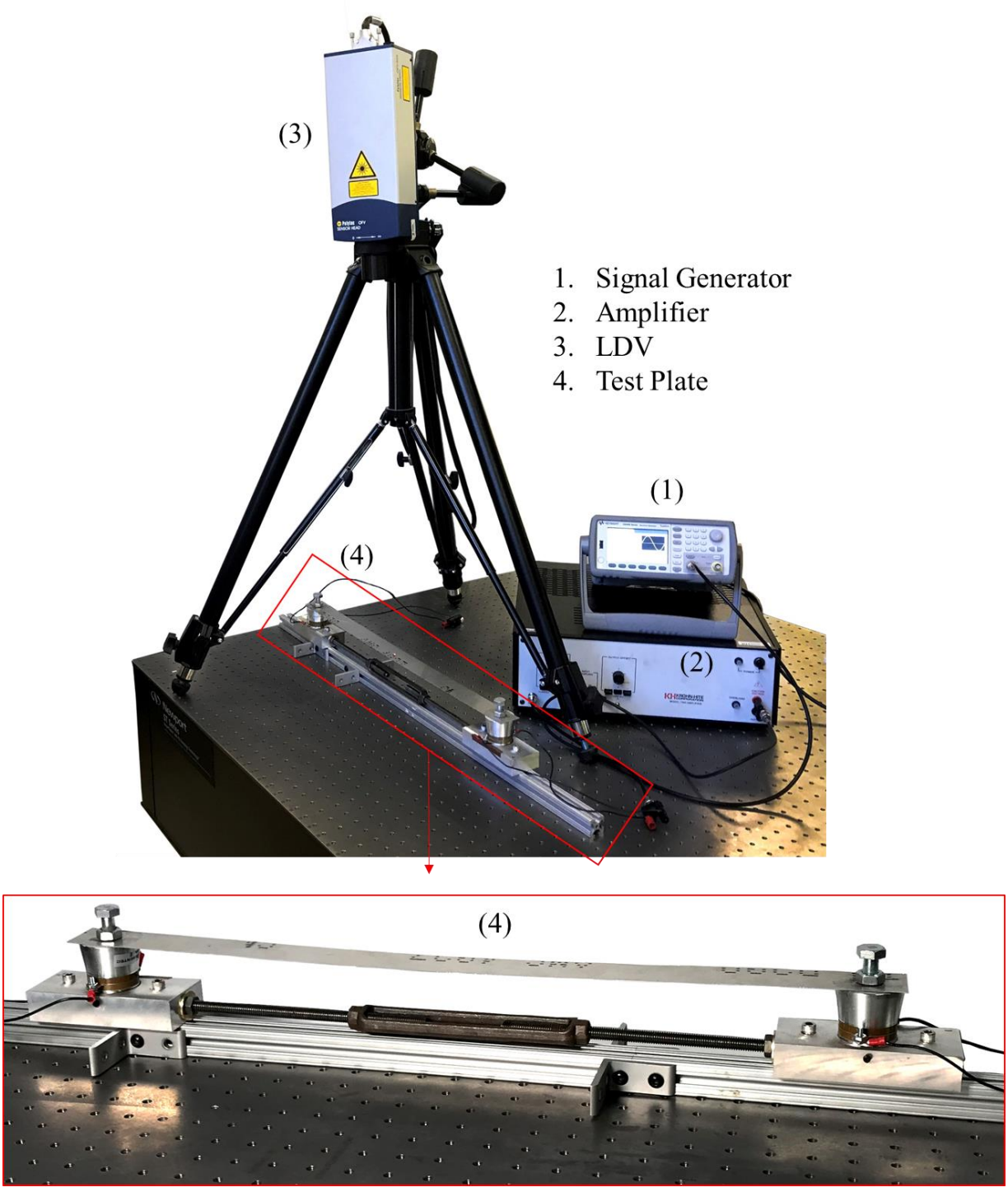

Figure 5.7. Experimental plate dryer proof-of-concept experiment.

5.5. Finite element modeling

COMSOL Multiphysics is used for finite element modeling of the plate-actuator system. To limit the cost of prototyping, it is highly desired to model systems with analytical or finite element methods, with the latter often being less time consuming while allowing for complex modeling conditions which may make analytical solutions less efficient. For these reasons, the structural mechanics module of COMSOL is used to develop a rapid model of the large-scale dryer.

We will investigate three plate boundary configurations, given by figure 5.8. The first, being a plate that is excited on one end, and fixed on the opposite. The second, being excited on one end with a roller boundary condition on the opposite. The third condition has the plate excited on one end with a boundary force on the opposite to simulate an applied tension to the plate. Finally, the fourth boundary condition will be excited on both ends with a potential phase difference.

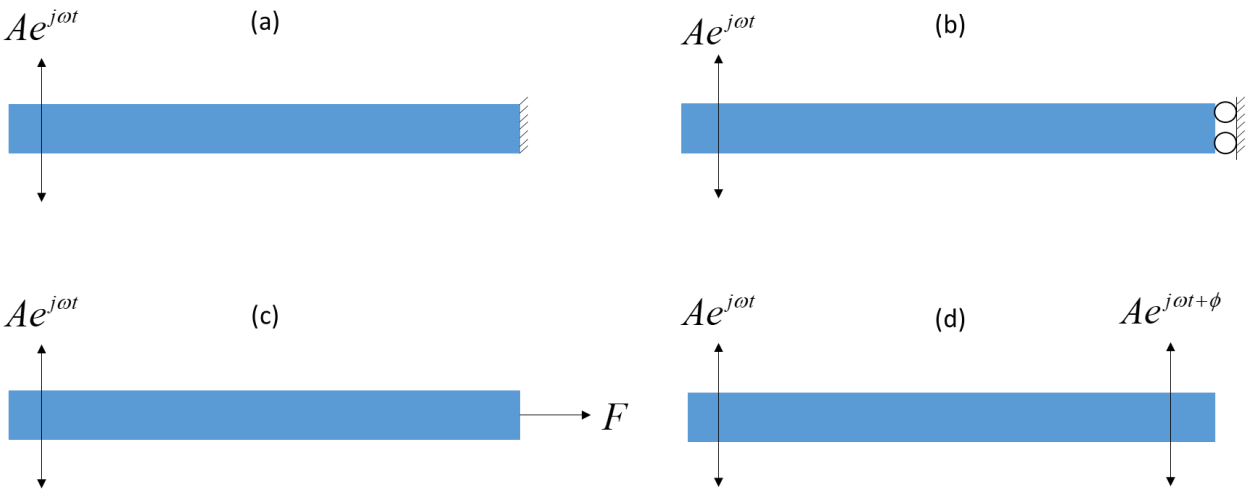

Figure 5.8. COMSOL equivalent models for **(a)** excited-fixed, **(b)** excited-roller, and **(c)** excited-tension, and **(d)** excited-excited plate configurations.

Evaluation of these configurations will be on the comparison of output acceleration versus the control parameters, being the applied tensions for figure 5.8c and the phase difference in figure 5.8d. Boundary condition changes will be compared against the average acceleration associated with each for the same forcing criteria. It is hypothesized that boundary conditions with the least constraints will lead to the highest magnitudes of output acceleration, as was evident in Appendix A of chapter 2.

5.6. Results and discussion

The varying boundary conditions applied to the opposite end of the plate from which a constant applied excitation is given has a critical influence on the output acceleration as well as the mode shapes of the plate. It can be seen in figure 5.9a-c that torsional modes as well as transverse modes are dominating the response of the plate, indicative of the bi-directional wave propagation over the plate, in both the width and length wise directions. It was quickly realized the roller boundary condition provides the highest magnitude of acceleration output, with its average value being nearly ten times that of the excited-fixed and excited-excited boundary conditions, given by table 5.1.

Boundary Condition	**Average Acceleration [ms^{-2}]**
Excited-Fixed	42,588
Excited-Roller	402,830
Excited-Excited	68,750

Table 5.1. Average output acceleration for the three boundary conditions investigated.

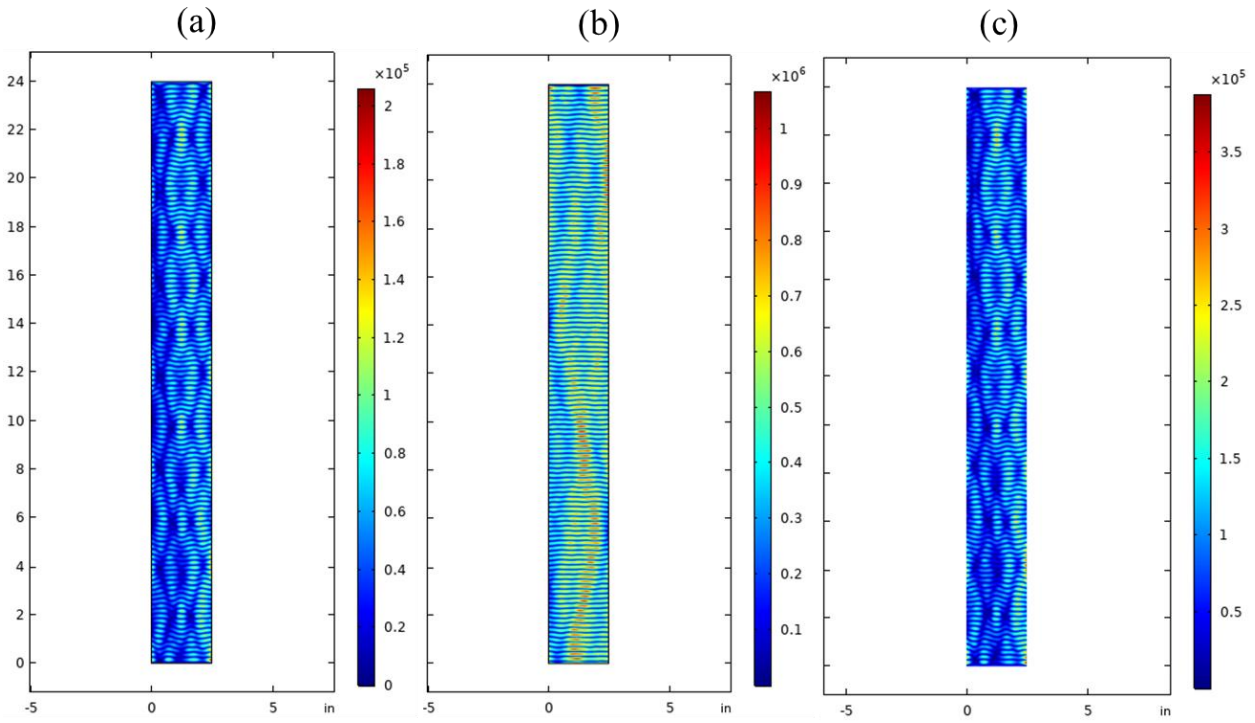

Figure 5.9. Transverse acceleration magnitude for **(a)** excited-fixed, **(b)** excited-roller, and **(c)** excited-excited boundary conditions.

The use of the roller boundary condition allows for the end of the plate to displace freely in the transverse direction as the wave propagation from the excitation source reaches the opposite end of the plate. The ability to displace reduces the strain at this end of the plate, effectively decreasing the damping of this boundary condition. The excess energy is then able to reverberate back to the excitation source where constructive interference of the wave fronts provides an increase in output acceleration.

A special case of the excited-excited boundary condition is when one actuation source operates out of phase from the other. This may be conductive of either constructive or destructive interface when the source and reflected wave fronts meet. Figure 5.10 shows simulation results for various values of the phase difference between the actuators. It can easily be realized that having

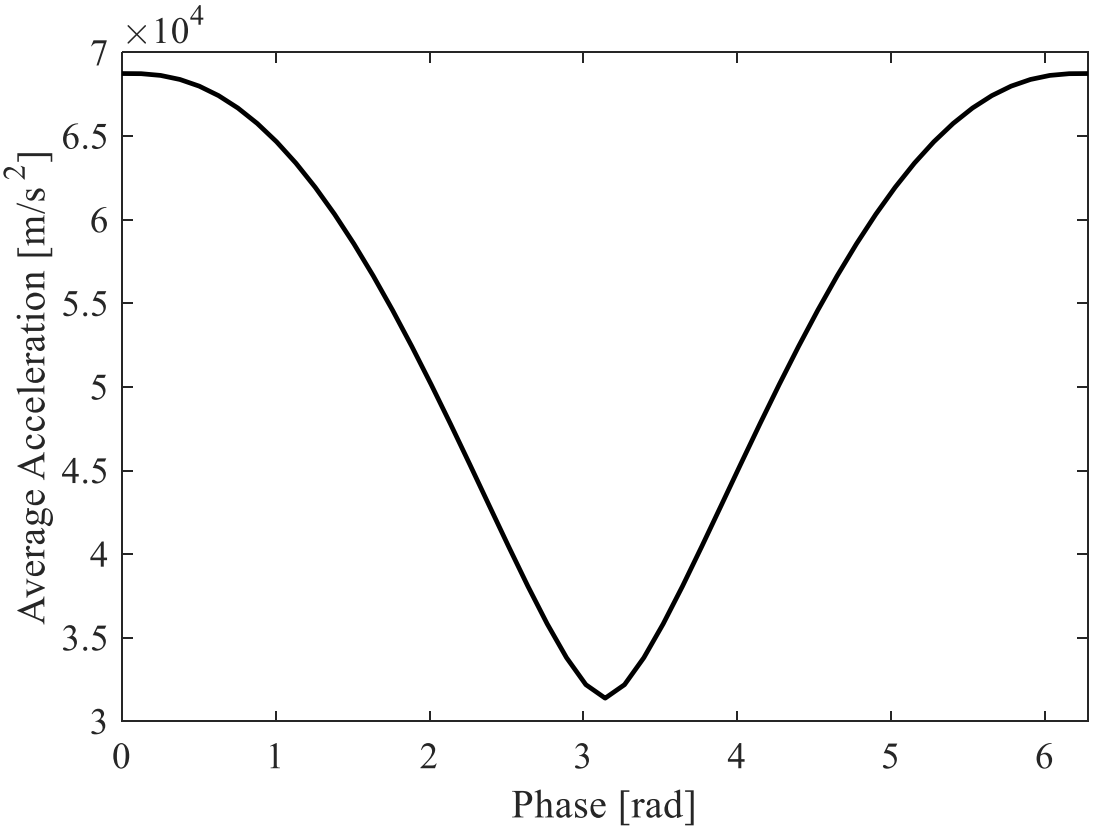

Figure 5.10. Output acceleration as a function of the phase difference applied for the excited-excited plate boundary condition.

both sources of actuation being in phase produces approximately twice the acceleration output as when they are entirely out of phase.

The experimental set-up was found to be highly dependent on the tension applied from the turnbuckle. Figure 5.11a shows various experimentally measured values of acceleration at the plate's center to arbitrarily changing values of tension. We begin with a buckled plate, indicating negative tension, and increase gradually until reaching a taught plate. The highest magnitudes of acceleration reached for both experiment and FEM are achieved when this negative tension is applied.

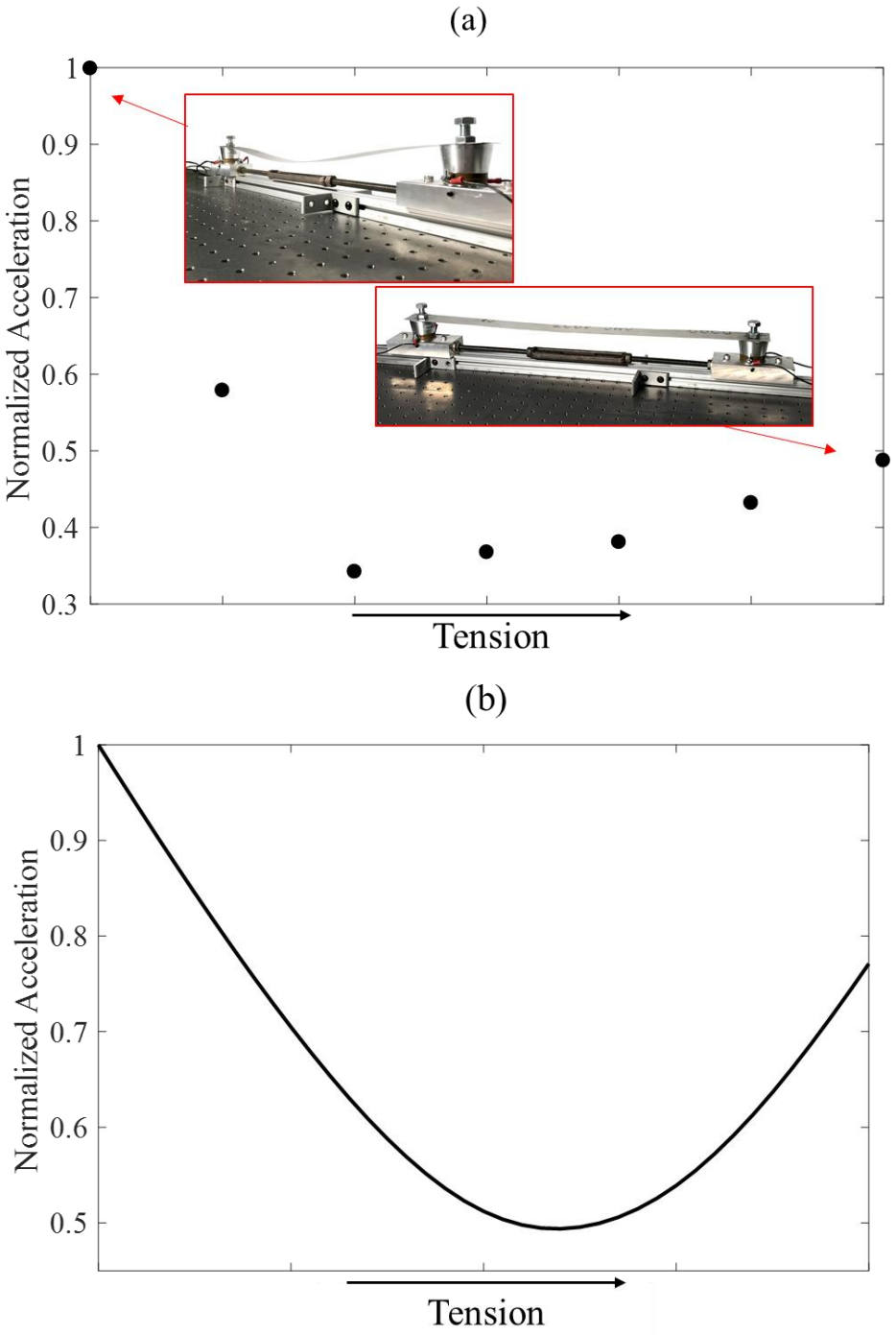

Figure 5.11. Normalized surface acceleration of the plate compared to increasing tension, **(a)** experiment, and **(b)** finite element modeling results.

To compare the effectiveness of the plate design to commercially available transducers used in prototypes of the direct contact ultrasonic dryer, we introduced a power per unit area

parameter for when atomization is achieved. Two commercial devices shown to be effective are the F100 (figure 1.2) and similar but smaller version denoted as the F135. While these transducers are effective atomizing devices, the small contact area limits their effectiveness as a large number of devices are needed for drying any substantial volume of fabric. The plate is tuned in these experiments as according to the information gained from the boundary condition investigation found using FEM and experiment. The plate is actuated by a single transducer in a buckled configuration. It is quickly seen that due to the small contact areas of the F100 and F135, that the power per unit area needed for atomization is significantly larger than that of the plate (Table 5.2).

Device	Area [m^3]	Power [W]	Power/Area
F135	5.03e-05	1.6	3,1831
F100	3.46e-04	1	2,887
Plate	0.0403	40	992

Table 5.2. Power consumption per unit area when atomization is achieved for different structures.

5.7. Conclusions

The feasibility of large-scale excitation for the purpose of atomizing water was achieved successfully. Through adjustments of the plate geometry, actuating frequency, and boundary conditions, atomization was realized over the entire surface area of a 24” x 2.5” x 1/64” plate actuated by a single bolt-clamped Langevin transducer. Both experiments and finite element modeling highlighted the importance of the applied tension to the plate, where a buckled configuration as well as a taught configuration achieved atomization, but intermediary values between these tensions was unsuccessful. Further simulations of varying the boundary condition to that of being actuated on one end, and a roller boundary on the other resulted in significant

improvements to the output acceleration of the plate. This is due to limiting the constraints on the plate, decreasing the damping of the system. From this investigation, we will be able to investigate perforated materials, plates comprised of different materials, as well as geometry changes and predict their influence on ultrasonic drying. Future considerations of the properties are identified in section 6.5.4.

Bibliography

1. Dupuis, E.D., et al., *Electroelastic investigation of drying rate in the direct contact ultrasonic fabric dewatering process.* Applied Energy, 2019. **235**: p. 451-462.
2. Dupuis, E.D., et al., *Electroelastic investigation of drying rate in the direct contact ultrasonic fabric dewatering process.* Applied Energy, 2019. **235**: p. 451-462.
3. Dupuis, E.D., et al., *Multiphysics modeling of mesh piezoelectric atomizers.* Proc. SPIE Smart Structures and Materials + Nondestructive Evaluation and Health Monitoring, 2018. **10595**: p. 1-9.

Chapter 6

Summary of contributions and prospective future research

6.1. Intellectual merits

The proposed dissertation includes the electro-elastic analytical models, which couple multi-physic topics, as well as finite element and experimental verification of the developed models. The models developed identify the influence of key parameters on ultrasonic drying and will aid in improving atomizer design for efficient, timely fabric drying. This study is the first proposed model for the ultrasonic atomization of fabrics saturated with water, applicable to any type of transducer. The results present a non-dimensional equation for the ultrasonic dewatering of fabrics, dependent only on transducer acceleration and the surface area of the cloth. The development of this technology using the proposed physical models will allow for global reductions in electrical demand related to clothes drying.

6.2. Broader impacts

The vast majority of households and many industries use clothes dryers of one form or another. The common method of drying, evaporating water by imparting thermal energy, has a limited energy efficiency as the latent heat of evaporation of water is relatively high. Additionally, the process of generating heat by passing electricity through metals and heating a much larger volume of air than the clothes occupy is wasteful. The proposed method of drying has the capability of being highly efficient, as the source energy for drying comes from piezoelectric materials, which convert the vast majority of electrical energy to mechanical energy, and have near

limitless lifecycles; furthermore, the ability to substantially improve drying times and efficiency by design characteristics alone is a huge advantage over conventional dryers. The research findings will be disseminated through conference presentations and scholarly publications.

6.3. Awards and recognition

- Awards and recognition:
  - Manuel Stein Fellowship, December 2018
- Presentations/proceedings have been contributed to the scientific community:
  - SPIE Smart Structures + Nondestructive Evaluation in the 2018 International Society for Optics and Photonics [1]
  - ASME 2018 Conference on Smart Materials, Adaptive Structures and Intelligent Systems [2]
- Journal Papers
  - Dupuis, E.D., et al., *Electroelastic investigation of drying rate in the direct contact ultrasonic fabric dewatering process.* Applied Energy, 2019. **235**: p. 451-462.
  - Dupuis, E.D., et al., *Coupling of electroelastic dynamics and direct contact ultrasonic drying formulation for annular piezoelectric bimorph transducers,* 2020 Smart Mater. Struct. 29 045027

6.4. Summary

This dissertation presents the research and development of the next generation of drying technology, utilizing a novel mechanic called atomization. Highly efficient piezoelectric elements

actuate and force the bulk liquid retained in wet fabrics to dissociate into smaller micrometer sized droplets in the form of a mist. This mist is then vented away from the fabric to facilitate the rate of drying. While the method of supplying the vibrations is an open-ended question, we have developed a framework for identifying key principles affecting the rate of ultrasonic drying and connected the output deformation of a vibrating device to the rate of water loss inside of the fabric. We have proposed several design considerations, including the mounting conditions, size of the actuated device, and boundary conditions of the system, which have been shown to increase the effectiveness of ultrasonic drying.

Chapter 2 considers the vibrations of the central plate for the F100 transducer, actuated by the annular piezoelectric rings adhered to it. An analytical model was developed which predicts the output acceleration for a given base excitation, taken from experimental data. The resulting mode shapes and displacement of the device is then directly connected to the rate of water loss through empirical data. It was found that the peak acceleration is a poor indicator of performance at high voltages due to nonlinearities present in the system from mid-plane stretching. Considering this, we analyze the drying rates as they compare to the average applied acceleration over the contacting area of the fabric. Both finite element modeling as well as a SLDV are used to confirm the predicted acceleration and mode shapes of the vibrating transducer. The result of this chapter is a unified expression for the nonlinear rate of water loss in fabrics as a function of the applied acceleration to the fabric.

Chapter 3 completes the modeling efforts begun in chapter 2. The previous chapter relied upon experimental data for the base excitation of the central plate, a key component which is electromechanically coupled through the piezoelectric rings. Chapter 3 then proposes, based on Hamilton's principle, a derivation for an annular bimorph transducer operating in the thickness

mode of vibration. The result of this model is a coupled equation where the input voltage to the system predicts an output displacement. This displacement then becomes the base excitation term missing from chapter 2. Experimental data collected using a LDV was shown to closely match with the expected modal frequency, both on and off resonance, of the transducer. The end result allows for optimization of the bimorph, through boundary conditions and piezoelectric materials used. It was found that an epoxy layer bonding the transducer to a fixture can be chosen carefully to lower the stiffness of the system, allowing for resonance matching between the bimorph and plate. We then show that this layer, when a certain thickness is selected, can decrease the drying times by 50%, correlating to a 50% reduction in energy consumption, drastically increasing the efficiency of ultrasonic drying.

Chapter 4 connects the passage of water through microchannel perforations within the plate to its vibration characteristics. The previous modeling efforts allowed for the prediction of displacement for each microchannel in the plate, being the input parameter for the Couette driven flow in the microchannel. Channel geometry was found to be highly influential on the drying characteristics and mist ejection of the F100 transducer. Perforation sizes were found to influence the adhesion of the mist leaving the channels, where too large of an exit diameter results in millimeter scale droplets forming on the underside of the device rather than micrometer mist ejection in the form of a jet.

Chapter 5 considers alternative dryer designs compared to a prototype utilizing the F100 annular piezoelectric transducers. Large area atomization was found to be capable of increasing the efficiency of the design, as well as simplifying the components needed for such a system. Moving from the small 30mm diameter F100s to bolt clamped Langevin transducers was found to decrease the number of transducers needed for similar sized drying capabilities.

The vast majority of households and many industries use clothes dryers of one form or another. The common method of drying, evaporating water by imparting thermal energy, has a limited energy efficiency as the latent heat of evaporation of water is relatively high. Additionally, the process of generating heat by passing electricity through metals and heating a much larger volume of air than the clothes occupy is wasteful. The proposed method of drying has the capability of being highly efficient, as the source energy for drying comes from piezoelectric materials, which convert the vast majority of electrical energy to mechanical energy, and have near limitless lifecycles. Furthermore, the ability to substantially improve drying times and efficiency by design characteristics alone is a huge advantage over conventional dryers.

The results of this work may revolutionize the textile drying industry. While vibration based drying is gaining attention in the food drying industry, research is progressing at a relatively slow pace when compared to the potentially drastic increase in energy efficiency. The direct connection between the deformation of the actuating device and the atomization of water and the fundamental relationships highlighted will entice further researchers to develop creative designs that will aid in the public acceptance of this novel technology. The energy savings that will follow this research will lead to a reduction in the consumption of electricity, and will help both the energy security of the United States as well as reducing climate changing emissions. The research findings will be disseminated through conference presentations and scholarly publications.

6.5. Future work

This investigation has provided the framework for future development of direct contact ultrasonic drying technology. Analytical modeling of the vibrating system was found to be

extremely beneficial to increasing the effectiveness of this technology. Through the analysis of boundary conditions and material properties, we were able to show a substantial increase in drying performance, as given in Chapter 3; however, this technology is still in its early years, and more investigation is needed into the following areas of research:

1. Nonlinear effects due to mid-plane stretching of the F100 transducer.
2. Textile material properties and their influence on atomization.
3. High frequency flows in an open-ended microchannel.
4. Creative designs for large area atomization.
5. Optimization of the devices used.

6.5.1. Nonlinear investigation

At increasing magnitudes of applied voltage to a piezoelectric transducer, its displacement will continue to increase until either saturation or failure occurs. It was shown experimentally that the displacement of the F100 transducers plate will exceed its thickness at relatively low voltages (~30V) as it approaches the operating frequency of ~100 kHz. This indicated in the chaotic nature of the FRF given in Chapter 2, Appendix B. Midplane stretching manifests itself in a complicated displacement vector, given by figure 6.1. The neutral axis deforms in a way such that a line perpendicular to the axis does not remain so after deformation, a necessary feature of linear plate theory used in the modeling for Chapter 2.

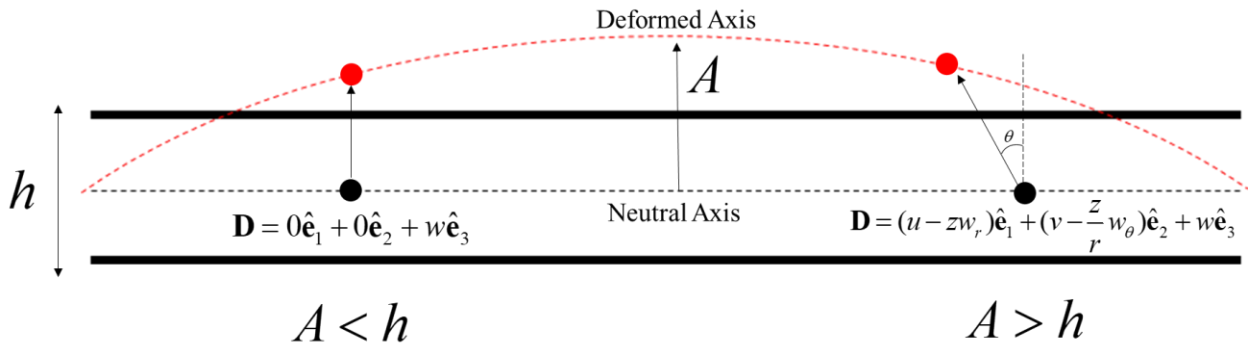

Figure 6.1. Midplane stretching and its influence on the displacement vector.

Through the inclusion of midplane stretching, the equation of motion will have components in all three coordinate directions, rather than the transverse direction as is assumed with a Kirchoff plate model. These types of problems are commonly solved using perturbation techniques, method of multiple scales, and other nonlinear analysis techniques. It is hypothesized that inclusion of these nonlinear effects will allow for exploiting midplane stretching in order to maximize the acceleration output, increasing the predicted values from that of the linear model and capturing the true behavior of the transducer.

Furthermore, the inclusion of bending in the equation of motion will result in an increased prediction for the acceleration output of the transducer. While it has been shown that thickness deformations dominate the response of the piezoelectric bimorph, radial modes are still present due to the orthogonal coupling between poling in the radial direction and strain in the transverse direction. In these ways, inclusion of midplane stretching will serve to increase the accuracy of the model and may provide interesting physical insights into increase the performance of this technology.

6.5.2. Textile properties influence on drying

Textiles are arranged in a large variety of ways, from differences in weaves, to the fibers which comprise the fabric (figure 6.2 [3, 4]). As such, the void space between threads highly effects the atomization capabilities of the moisture contained within. Previously, we introduced the ratio of forcing from the oscillating source to the surface tension of liquid droplet necessary to achieve atomization. The tighter a woven fabric fibers are held, the smaller the droplets they retain will be. It is then easy to see that a higher magnitude of forcing will be necessary for those fabrics with the smallest of retained liquid inside of the void space. It is crucial to understand the ways in which different fabrics experience atomization as it relates to the direct contact ultrasonic drying process.

To understand the influence of various fabrics, an in depth empirical investigation must be made for the drying rates of textiles exposed to various magnitudes of acceleration. It is hypothesized that correction factors will be all that is needed for altering equation 2.22, connecting the drying rates of fabrics to the applied average acceleration. This is due to the nature of these nonlinear curves. The limited amount of water capable of being atomized due to the forcing ratio can be further increased to dissociate smaller droplets when exposed to increasing magnitudes of acceleration. The time it takes to atomize these droplets will decrease with increasing applied

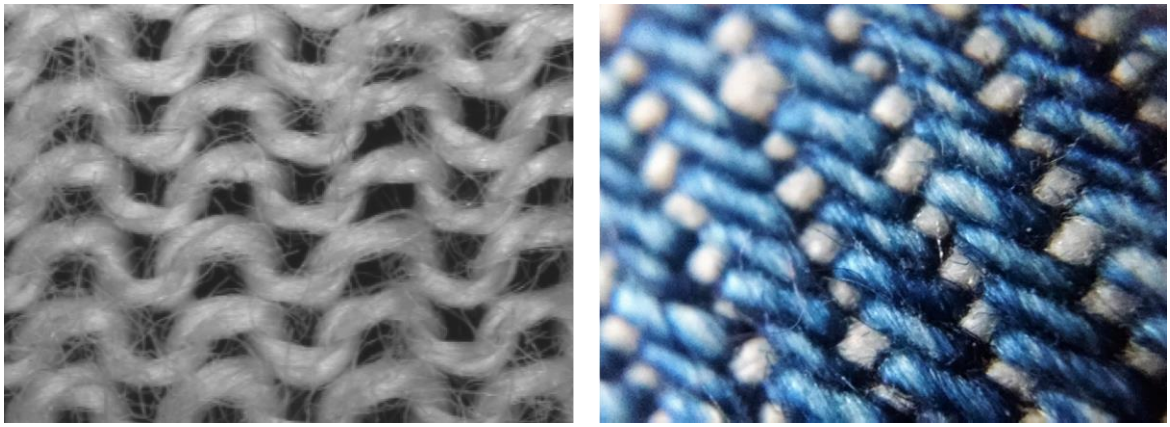

Figure 6.2. Microscope images of two different fabrics.

acceleration; however, this theory of adding correction factors has yet to be proven, and a methodical study including many types of textiles must be analyzed and related to the acceleration imparted to it. Furthermore, this investigation will identify operating conditions of the transducer which best dry specific fabrics. For commercial applications where many items of the same fabric are being dried, such as in hotels and hospitals, a custom dry cycle can be created in order to increase the efficiency of the drying cycle for a given fabric.

6.5.3. High frequency microchannel flows

Oscillatory flows in microchannels have only been considered for upwards of ~100 Hz. However, the atomization process is currently carried out at a frequency of ~100 kHz, and it is necessary to work above the audible hearing range, limiting the lower end of operating frequencies to ~20 kHz. Furthermore, open-ended microchannels, where both the inlet and outlet are effected by atmospheric conditions, is rarely studied. Open-ended outlets are commonly seen in emulsification, and droplet production applications, however the inlets for these types of flows are typically pressure driven, allowing for known inlet conditions. The inertial effects of high frequency flows is an area needing much more consideration, as few modeling efforts have been attempted in literature. The influence of cavitation within microchannel flows is another area needing more insight, as the passage of two phases through microchannels greatly complicates the flow conditions.

6.5.4. Alternative dryer design

Chapter 5 dealt with the difficult task of scaling up the transducer design to a structure with large area atomization. For this investigation, a rectangular plate is investigated, however future

designs may consider cantilevered structures or multiple tuned masses which vibrate in resonance with the actuators. The ultimate goal is to achieve resonance, resulting in atomization of water, with as little input energy as possible over the largest surface area possible. Preliminary evidence has shown that for these larger structures, a large magnitude of forcing is necessary, as well as relatively large displacements as piezoelectric elements are concerned. While stack actuators are able to displace by the required amounts (tens of micrometers), their large masses results in very lowly natural frequencies where these stroke lengths are achieved.

One such concept of utilizing cantilevers is pictured in figure 6.3. The advantages of this design is the decreased mass from the gaps between individual cantilever beams, and the ability to control the resonance frequency with a higher resolution than that of an entire plate. Due to the large displacements cantilevers can achieve, it was found that atomization for a single beam is easily achieved.

With regards to actuation, it is hypothesized that using negative Poisson ratio devices actuated by piezoelectric transducers with large forcing capabilities is the ideal solution to this problem. This would enable devices which operate the high frequencies necessary to achieve large enough displacements for atomization to be realized. Such devices consist of armatures, which utilizes a simple lever type configuration to increase the output displacement of a piezoelectric transducer.

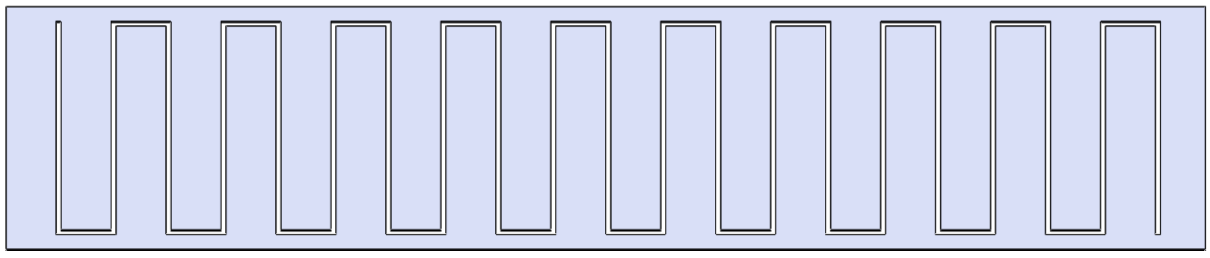

Figure 6.3. Plate with individual cantilevers within its volume.

6.5.5. Optimization

The geometry and material properties of the transducer used in ultrasonic drying has a substantial influence on the output acceleration, and thus, the rate of drying. It is crucial to optimize these parameters in order to increase the efficiency of this process. Due to the manifestation of material properties and geometry in the mode shapes, as well as the linear coupling of piezoelectric properties with the output deformation, it is recommended to use a genetic algorithm. This form of optimization evaluates the transducers performance for a variety of randomly selected values constrained to a range of realistic dimensions.

Bibliography

1. Dupuis, E.D., et al., *Electroelastic investigation of drying rate in the direct contact ultrasonic fabric dewatering process.* Applied Energy, 2019. **235**: p. 451-462.
2. Dupuis, E.D., et al., *Multiphysics modeling of mesh piezoelectric atomizers.* Proc. SPIE Smart Structures and Materials + Nondestructive Evaluation and Health Monitoring, 2018. **10595**: p. 1-9.
3. Ikiwaner, *Gestrick links-rechts linke Seite*. 2004: Wikimedia.
4. Dinesh Dhankhar, *Fabric of a jeans 2*. 2016: Wikimedia.